BRNO UNIVERSITY OF TECHNOLOGY

Faculty of Electrical Engineering
and Communication

DOCTORAL THESIS

Brno, 2018 Ing. Štěpán Foral

BRNO UNIVERSITY OF TECHNOLOGY

VYSOKÉ UČENÍ TECHNICKÉ V BRNĚ

FACULTY OF ELECTRICAL ENGINEERING AND COMMUNICATION

FAKULTA ELEKTROTECHNIKY
A KOMUNIKAČNÍCH TECHNOLOGIÍ

DEPARTMENT OF ELECTRICAL POWER ENGINEERING

ÚSTAV ELEKTROENERGETIKY

PERFORMANCE OF COMPOSITE NUCLEAR FUELS DURING NORMAL OPERATION AND NUCLEAR REACTOR ACCIDENTS

CHOVÁNÍ KOMPOZITNÍCH JADERNÝCH PALIV V PRŮBĚHU NORMÁLNÍHO PROVOZU JADERNÉHO REAKTORU A HAVARIJNÍCH SITUACÍ

DOCTORAL THESIS
DIZERTAČNÍ PRÁCE

AUTHOR
AUTOR PRÁCE

Ing. Štěpán Foral

SUPERVISOR
ŠKOLITEL

Ing. Karel Katovský, Ph.D.

Doc. Ing. David Salamon, Ph.D.

BRNO 2018

ABSTRAKT

Tato práce se zabývá oblastí kompozitních jaderných paliv založených na UO_2. V práci je vyjmenováno několik materiálů vhodných jako aditivum ty jsou srovnány z několika různých hledisek. Byla vybrána kombinace UO_2 + SiC pro detailní analýzu. Bylo zjištěno, že tato kombinace vykazuje dobré parametry v průběhu normálního provozu. Uvolňování plynných produktů štěpení je nižší společně s tepelně-mechanickým namáháním. Nicméně, je potřeba vyvinout nové modely chování kompozitních paliva. Analýza havárie blézké typu LOCA ukazuje, že palivo UO_2 + SiC vykazuje poněkud lepší parametry ve srovnání s UO_2. Centrální teplota je nižší a mechanické namáhání je rovněž nižší. Na druhou stranu, analýza RIA havárie ukázala možné potíže. Například, zvýšená tepelná vodivost byla pravděpodobným důvodem zvýšené maximální teploty pokrytí a umocněné krize varu. Toto zjištění se pravděpodobně týká všech paliv založených UO_2, které mají zvýšenou tepelnou vodivost pomocí dopantů.

Tato práce byla podpořena projektem CANUT, reg. č. 2012TE01020455.

KLÍČOVÁ SLOVA

Lehkovodní reaktor, PWR, VVER, oxid uraničitý, kompozitní palivo, LOCA, RIA .

ABSTRACT

This work deals with the domain of composite fuels based on standard UO_2. Several candidate materials for dopants are listed in the work and they are compared from different points of view. The UO_2 + SiC fuel option is selected for detail analysis. It was found that this fuel option shows good behavior during steady state operation. The Fission Gas Release is lower together with mechanical load. Nevertheless, new models of the composite behavior need to be developed. The analysis of LOCA-type accident reveals that the UO_2 + SiC fuel option shows slightly better behavior compared with UO_2. The fuel centerline temperatures is lower and the mechanical loading is lower as well. On the other hand, the analysis of RIA accident revealed possible issues. For example, the increased thermal conductivity was likely the root of higher peak cladding temperature and consequent increased departure from nucleate boiling. This finding is very likely to be find by all UO_2 based fuels with thermal conductivity increased by dopant.

The work was supported by the CANUT project, reg. No. 2012TE01020455.

KEYWORDS

Light water reactor, PWR, WWER, uranium dioxide, composite fuel, LOCA, RIA

FORAL, Š. *Chování kompozitních jaderných paliv v průběhu normálního provozu jaderného reaktoru a havarijních situací*. Brno: Vysoké učení technické v Brně, Fakulta elektrotechniky a komunikačních technologií, 2019. 162 s. Vedoucí dizertační práce Ing. Karel Katovský, Ph.D.

PROHLÁŠENÍ

Prohlašuji, že svou dizertační práci na téma *Chování kompozitních jaderných paliv v průběhu normálního provozu jaderného reaktoru a havarijních situací* jsem vypracoval samostatně pod vedením vedoucího dizertační práce a s použitím odborné literatury a dalších informačních zdrojů, které jsou všechny citovány v práci a uvedeny v seznamu literatury na konci práce.

Jako autor uvedené dizertační práce dále prohlašuji, že v souvislosti s vytvořením této doktorské práce jsem neporušil autorská práva třetích osob, zejména jsem nezasáhl nedovoleným způsobem do cizích autorských práv osobnostních a/nebo majetkových a jsem si plně vědom následků porušení ustanovení §11 a následujícího autorského zákona č. 121/2000Sb., o právu autorském, o právech souvisejících s právem autorským a o změně některých zákonů (autorský zákon), ve znění pozdějších předpisů, včetně možných trestněprávních důsledků vyplývajících z ustanovení části druhé, hlavy VI. díl 4 Trestního zákoníku č.40/2009 Sb.

V Brně dne 20. 12. 2018 **Štěpán Foral**

PODĚKOVÁNÍ

Je velké množství lidí, kterým bych chtěl v tuto chvíli poděkovat. V první řadě ale děkuji Bohu za to, že nyní, na Vánoce 2018, po vice jak sedmi letech doktorského studia a téměř třiceti letech v českém výchovném systému, mohu odevzdat tuto dizertační práci. Dále děkuji všem mým blízkým přátelům a dalším lidem, kteří I jinak pozitivně vstoupili do mého života: MP, EK, JHB, PH, VN a dalším.

V neposlední řadě děkuji mé rodině za podporu a mým vedoucím za možnost věnovat se tomu, co mě baví a o co mám zájem.

V Brně dne 20. 12. 2018 **Štěpán Foral**

- PER ADSTERA AD ASTRA -

Publius Vergilius Maro

Contents

List of Figures

List of Tables

1 Introduction

1.1 Aims of the thesis

The necessity of safe operation of nuclear reactor forces the nuclear power industry to utilize all the means which are usable for higher safety of reactor operation. This work focuses on the most basic part of the nuclear reactor - the nuclear fuel itself. By influencing its basic mechanical properties, one can reach significant improvements in reactor operation and mitigate accident consequences. This is why this work deals with the concept of the composite nuclear fuel which is based on the standard UO_2 fuel by addition of small fraction of second phase.

In this thesis, this concept was selected for a simple reason. Most of the properties of such kind of fuel can be estimated from the known properties of UO_2 which are corrected for the influence of the secondary fraction. This work assesses selected composite fuel from different points of view and estimates the influence on operational and accidental parameters. The following lines also provides details on how the assessment was done throughout this work.

This first chapter provides the general information. First, the operational states of nuclear reactor are presented. This is followed by the summary of how the nuclear fuel pellet behaves during normal burnup conditions. After that the concept of such called Accident Tolerant Fuels (ATF) is introduced and the main representatives of this section are mentioned. This type of fuel should pose improved behavior during the operational and accidental conditions.

Second chapter provides mainly the theoretical background for the third computational analysis chapter. At first, the thermal conductivity mathematical models of composite systems are deeply introduced since their knowledge is crucial for thermal behavior analysis. After that, the individual candidate material are introduced which are considered as potential additives into the UO_2 matrix. Such a UO_2 fuel containing larger fractions of additives is referred as *composite fuel* within this work. The next part of the second chapter is dedicated to models usable for modelling the thermal conductivity degradation of individual candidate materials under neutron irradiation. Material property models are listed in the last subchapter.

The third chapter is dedicated to computational analysis of composite fuel options. At first, the individual candidate composite fuels are compared using the UWB neutronic code and other simple methods. After that, one representative fuel option is selected for more detail analysis using the RELAP5 and FEMAXI6 codes.

The fourth chapter gives a short introduction of codes (RELAP5, FEMAXI6, UWB, and TRANSURANUS) used for the composite fuel behavior analysis.

The fifth chapter focuses on the behavior of the selected option of the composite nuclear fuel during normal operation. The FEMAXI6 code was verified by comparison of its modeling results with results of other codes at first. After that, the code was modified by implementing material models of second phase. A sensitivity study was performed using this modified code in order to see its influence on selected operational parameters.

The sixth chapter investigates the influence of the second phase on the mitigation of LOCA-type accident. The PSB-VVER model and RELAP5 code were utilized for this study in the first step. The influence on macroscopic parameters of changed thermal conductivity and specific heat was investigated. Next, the simulation results in the form of cladding surface temperature were used as the boundary condition for microscopic fuel analysis performed by the modified FEMAXI6 code.

The analytical part is finished by the RIA analysis of the selected composite in the chapter number seven. This work has been done in cooperation with NRC Řež. Here, the TRANSURANUS code has been utilized for the analysis of the standard and composite nuclear fuel at different burnups. This chapter predicts very interesting behaviour of the standard fuel compared that composite one.

The last chapter summarises the results and conclusions drawn in individual chapters. General conclusions and recommendations are presented here as the main contribution of this work. There is now appendix in this work.

There are two versions of this PhD. thesis. The first one is confidental and contains all the data and modelling details. The second non-confidental version does not contain the detail information about the SiC thermal conductivity degradation model and about the RIA analysis results.

1.2 Burnup effects in nuclear fuels

The information given in this subchapter is mainly based on the lecture dedicated to nuclear fuel behavior during burnup which was given by Mr. Druenne within the BNEN course *Safety of Nuclear Power Plants* provided by the SCK-CEN [1]. Another great source of information was the famous book of Olander *Fundamental aspects of nuclear fuel elements* [2].

During the burnup, the nuclear fuel undergoes a strong change in the sense of structural integrity, chemical composition, and physical properties. The main fuel behavior phenomena are briefly listed here because they are then investigated in the second practical part of this work. The emphasis is put on the thermal conductivity behavior since it is of the main interest of this work. On the other

hand, the interaction with cladding is omitted in this subchapter since this work is limited on the fuel (pellet) behavior only.

First, the nuclear fuel is typically loaded with very high linear heat generation rate (LHGR). For instance in the case of VVER-1000 TVSA-T, the peak LHGR can reach up to 448 W/cm. The heat generated by fission is distributed along the pellet radii depending on the state of nuclear fuel (influence of plutonium content, self-shielding etc.) but for simplicity, a uniform volumetric heat generation is assumed. Starting from the general equation of heat conduction:

$$\frac{\partial(\rho c T)}{\partial t} = \nabla \cdot (\lambda \nabla T) + Q, \tag{1.1}$$

where ρ is the density, c is the heat capacity, T is the temperature and λ is the thermal conductivity, the famous general equation of temperature profile can be derived:

$$\int_{T_0}^{T} \lambda(T) dT = \frac{q_l}{4\pi} \left(1 - \frac{r^2}{r_u^2}\right). \tag{1.2}$$

Here, $\lambda(T)$ is the temperature dependent thermal conductivity which is integrated from reference temperature T_0 to the temperature T at the radial coordinate r. The q_l is the linear heat generation rate (LHGR) and r_u is the fuel pellet radius. The temperature T is usually found numerically for specific radial ratio on the right side of the equation.

If the equation of temperature profile is presented in the form of eq. 1.2, the axial heat conduction is neglected, the fuel is in steady state, and the heat is generated uniformly within the whole pellet volume. Next, this equation neglects the self-shielding effect as well, but, for low enriched fuel, its temperature prediction differs very slightly when the self-shielding effect is not neglected [3].

It is apparent, that the central temperature within the fuel pellet is dependent on the LHGR and thermal conductivity only. It can be seen from Figure 1.1 how the LHGR influences the centerline temperature. The temperature profile has the parabolic shape causing high centerline temperatures. So, in the case of UO_2 fuel, a risk of fuel melting can be significant.

The second factor having the influence on the centerline temperature is the thermal conductivity. The model of the UO_2 thermal conductivity consists of phonon and electronic terms, as depicted in Figure 1.2. The phonon term represents the phonons - virtual quasi-particles carrying the heat within the solid which behave like an ideal gas. Another interpretation of the phonon theory is that phonons are simply *lattice vibrations travelling through the lattice as waves* [4].

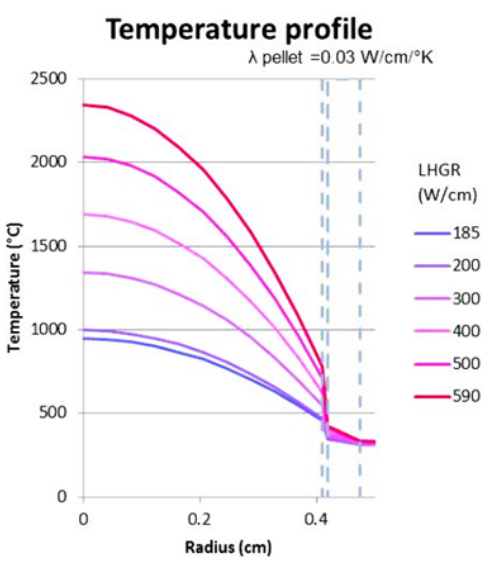

Fig. 1.1: Temperature profile in a fuel pellet calculated for different LHGR [1]

The phonon thermal conductivity in solids (λ_p) can be expressed by:

$$\lambda_p = \frac{1}{3}\rho C_v u \lambda, \tag{1.3}$$

where the C_v is the heat capacity at the constant volume, u is the phonon velocity, and λ is the phonon mean free path between collisions, defined as:

$$\lambda = \frac{1}{A + B \cdot T}. \tag{1.4}$$

The A term represents the phonon scattering cross section added by impurities and B is the term representing the influence of temperature T and phonon-phonon

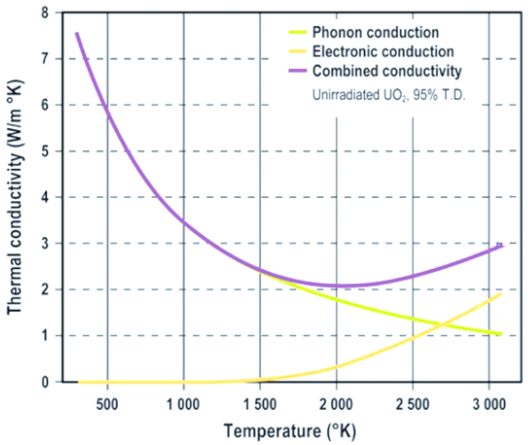

Fig. 1.2: Components of UO_2 thermal conductivity (from [1], modified)

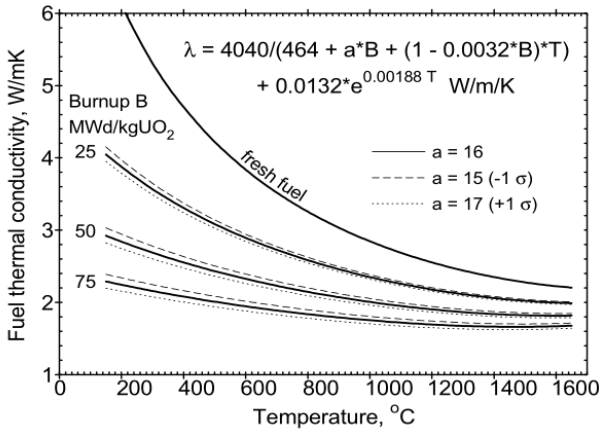

Fig. 1.3: Degradation of UO_2 thermal conductivity as measured at Halden [4]

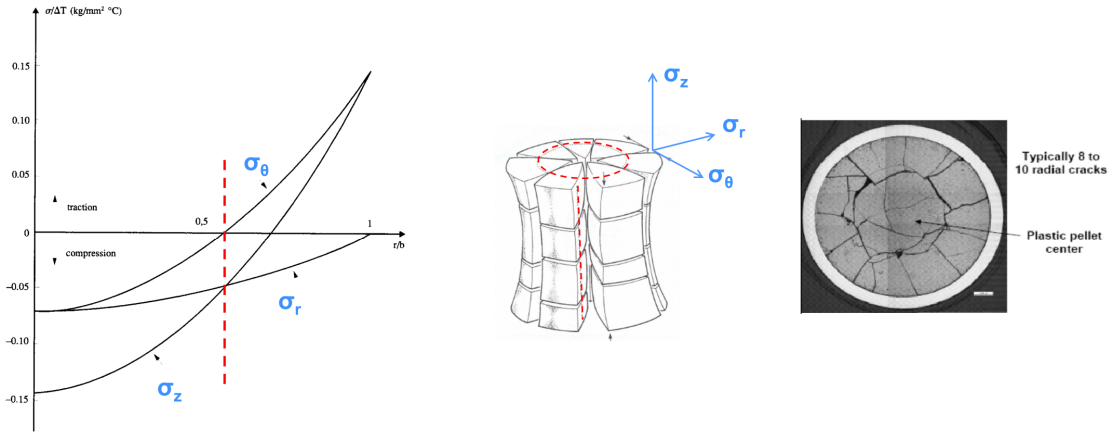

Fig. 1.4: Pellet internal stresses and the resulting pellet cracking

scattering. The thermal conductivity of UO_2 is very low due to the large phonon-phonon scattering which is due to the anharmonic components of crystal vibrations. As there is a large mass difference between U and O atoms, the lattice anharmonicity is consequently very large [2] and $(Pu/U)O_2$ pose the lowest thermal conductivity among other oxides. Next, the A is additionally increased by non-stoichiometry, presence of fission products, irradiation induced defects, porosity, and burnable absorbers within the lattice. The thermal conductivity degradation caused by burnup is depicted in Figure 1.3.

The second electrical term in Figure 1.2 is linked to electrical conductivity where the heat carriers are especially the electrons and then the holes, but this process is effective at higher temperatures only (>1500 °C).

Due to the steep temperature gradient within the pellet, the pellet is subjected to very high internal stress. Figure 1.4 shows the radial σ_r, axial σ_a, and circumferential σ_θ stresses acting during the hot full-power state of the reactor.

One can see, that whereas the interior of the fuel pellet is loaded by pressure, the surface is exhibited to tension. As a result of this tension state, the pellet cracks in a specific way. The zero-stress line is indicated by red curves and it is clearly visible in the figure on the far right that circular cracks are formed. Another influence resulting from the stress conditions is the pellet takes the shape of hourglass, as indicated in Figure 1.4.

Swelling and densification are the two processes related to the fuel pellet dimensions. The fresh pellet contains typically 5 % porosity which is intentionally left to accommodate the fission gasses and thus limit the pellet swelling. Pores which are smaller than approx. 1 μm disappear due to the radiation effect. As a consequence, the pellet shrinks about 0.5 % at the beginning of the fuel cycle (this is so called densification process). The pellet swelling works towards the densification process.

As the uranium atom splits in two fission products, the matrix has to accommodate the higher number of atoms. The solid fission products remain within the crystalline structure but the gaseous fission products (especially Xe and Kr) are not soluble. They either coalesce and form intragranular bubbles inside the grains or *diffuse to grain boundaries and form intergranular bubbles between the grains* [1].

The fission gas release (FGR) is another consequence of the intergranular bubble formation. In the case of athermal FGR, gaseous fission products escape directly through the free surface to the free volume. Another option is that the gas migrates from the intergranular bubbles along the grain boundary to free surface of the pellet and after that escapes from the pellet to the free volume. If so, the phenomenom is called thermal FGR and this type of FGR depends also on temperature and burnup. Both these phenomena increase the internal pin pressure. Too large internal pin pressure can cause the pellet-cladding gap reopening or clad collapse. This is why the FGR is of big importance for the safety operation of nuclear reactor.

1.3 The concept of accident resistant fuels: objectives and options

Since 2011, when the Fukushima accident happened, the R&D of ATF has gone through substantial progress. More money and scientific effort has been invested in order to enhance the reactor safety during normal operation and accidents. This means that new fuel concepts are under investigation in terms of new types of fuel matrix, claddings and their methods of production. Several main streams of ATF research can be identified nowadays: 1) modification of the current standard UO_2 fuel matrix, 2) development of new types of nuclear fuel matrix, 3) modification of the current Zr based cladding, 4) development of new types of cladding.

During the normal operation and accidental conditions, the new types of nuclear fuel matrix should pose at least comparable or even better operational and safety parameters (for example: lower fuel operating temperature, minimized fuel relocation, higher fuel melt temperature etc.). The main objective in cladding research is to improve the resistance to steam oxidation and to increase fission products retention especially above 1200 °C [5, 6, 7]. The US DOE plans to put these into commerce operation during the year 2022.

Within this subchapter, these concepts will be shortly introduced in order to provide a brief overview in this field.

1.3.1 Modification of the standard uranium dioxide matrix

Even before the Fukushima accident, the concept of UO_2 matrix modification was investigated in several ways. The main interest was to enhance the thermal conductivity of the fuel. This improvement is expected to mitigate the consequences of the Beyond Design Basis Accident (BDBA) since the enhanced thermal conductivity decreases the temperature profile within the fuel pellet and thus reduces the accumulated heat.

One of the possible ways is the modification of the UO_2 grain size when the fuel with larger grains leads to higher thermal conductivity. Another more progressive way seemed to be adding second phase particles within the UO_2 matrix. The second phase particles should have favorable neutronic properties, like e.g. low neutron absorption, and high thermal conductivity. Several candidate materials were found which are discussed in subchapter 2.2 in detail. The impact of such kind of fuel on double end guillotine LOCA (Loss of Coolant Accident) is investigated e.g. in [8].

In the early phase of LOCA accident, the thermal energy is released into the core causing a prompt increase in the core coolant temperature. Reference [8] investigates solely the influence of the fuel thermal conductivity on this phenomenon. This simulation has been done for the case of Westinghouse 4-loop reactor design with 80% LBLOCA (double-ended guillotine break in cold leg). Figure 1.5 depicts the situation after the break occurrence. There are distinct differences in fuel centerline temperature and peak cladding temperature for three types of fuel with different thermal conductivity. Beside the positive effect of decreasing centerline temperatures, the break transient shortens also with increasing fuel thermal conductivity. The latter effect can be also accounted to the fact that lower amount of accumulated thermal energy needs shorter time to be evacuated from the core.

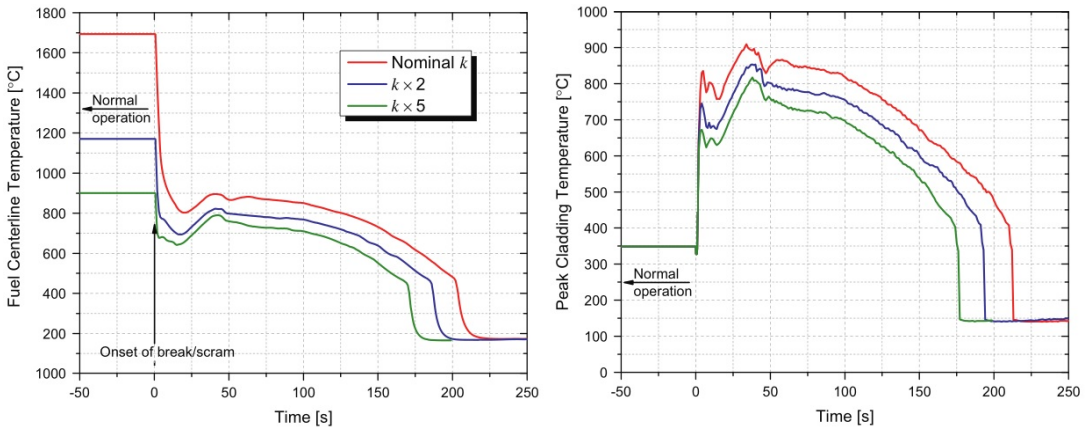

Fig. 1.5: Fuel and cladding temperatures of PWR during double end guillotine break LOCA with nominal and increased thermal conductivity (depicted as k) [8]

1.3.2 New concepts of nuclear fuels

Here, the U_3Si_2 is introduced as one of the new fuel options under consideration by Westinghouse company. Basically, this concept is not totally new, Uranium Silicide fuel option was found to be investigated in the late fifties and early sixties as the part of the advanced fuel development program for the sodium graphite reactors [9]. This concept was taken into consideration since it provides higher uranium density and thermal conductivity than that of standard UO_2 fuel. On the other hand, the melting temperature is lower compared to UO_2. Another option is to mix the U_3Si_2 with another fuel type - UN. The resulting UN-U_3Si_2 fuel provides higher thermal conductivity, fuel density and water resistance which is insufficient in the case of UN fuel [10, 11].

Another interesting option being investigated by ORNL is the Fully Ceramic Micro-encapsulated (FCM) fuel concept [6]. Here, the experience with TRISO particles is transferred to LWR technology and the UN fuel seems to be promising in this concept as well. But apart from TRISO particles which have a spherical shape, in the ATF concept, the highly enriched UN particles are confined within SiC matrix which has the shape of standard UO_2 pellet and works as another barrier retaining fission products. This type of fuel also shows good oxidation resistance versus zirconium alloy cladding. But here, the neutronic properties seem to be a big issue. *The high enrichment and reduced self-shielding within the fuel impacts the excess reactivity in fresh fuel which requires very high burnable absorbers loading* [11].

1.3.3 Modification of the current Zr cladding

The modification of the current Zr cladding consists of application of thin layer on the outer surface of fuel pin. The main aim is to improve the corrosion and oxidation resistance especially above 1200 °C when the chemical reaction producing hydrogen occurs. At the same time, the influence on thin coating layer on Zr cladding properties and reactor physics is minimal.

The chromium-based coating (Cr, CrAl, CrN) is investigated most widely. The advantage of this approach is that it not only reduces the oxidation rate, but irradiation stability (CrN), reduction in cladding ballooning during LOCA and resistance to cladding post-quench ductility loss were reported [12]. Reference [12] evaluates the Cr based coating as the most promising among others and this concept is supported by AREVA (Framatome nowadays) as well [13].

On the other hand, the diamond coating proposed by the Czech Technical University in Prague is not mentioned in this reference. The diamond has an excellent thermal conductivity and chemical stability. Currently, the this type of cladding

coating is loaded into the Halden reactor for irradiation stability test and the data are expected to be analyzed afterwards [14].

1.3.4 New concepts of fuel cladding

Several options like stainless steel, FeCrAl, Mo based cladding are being investigated. But the SiC cladding seems to be the most promising option according to [5]. SiC provides good neutron transparency and the chemical compatibility between UO_2 and SiC is well below 1500 K. The SiC/SiC composite cladding (SiC fibers embedded within SiC body) is considered as superior to SiC cladding since it offers better mechanical properties [15]. From the commercial point of view, this is the second concept being supported by AREVA. The challenges here are the SiC dissolution in high temperature, high pressure water and the potential for radionuclide release due to microcracking [12]. AREVA currently conducts irradiation of the Zr coated cladding and SiC/SiC composite in Goesgen reactor in Switzerland [13].

According to [12], the FeCrAl assures high steam oxidation resistance up to 1500 °C and the corrosion under water conditions should be minimal as well. The mechanical properties under neutron irradiation are good at least up to fluence of 15 dpa and the mechanical properties can be enhanced by adoption of its ODS variant. On the other hand, owing to its chemical composition, the neutron absorption is higher compared to Zr based cladding. Additionaly, there is a potential for increased diffusion of hydrogen from fuel across the cladding to coolant. Normally, the hydrogen is absorbed by Zr, but the BCC structure of the FeCrAl allows this process and this process must be further understand.

2 Overview of the models and background information

2.1 Thermal conductivity models of composites and their application in nuclear fuel modelling

2.1.1 Basic models of thermal conductivity of composites

In general, the analytical models for calculation the thermal conductivity of composites (TCC) are based on the former work focused on the calculation of electromagnetic field in composite materials. The first pioneer research was conducted by J. C. Maxwell. In his famous work *A Treatise on Electricity and Magnetism*, the first model of electrical conductivity for material containing heterogeneous particles was proposed. Because there is a strong analogy between electromagnetic and heat quantities, the results of his research could have been reused in the theory of heat conduction.

Today, there is a plenty of models which can be used for prediction of TCC. Many of them are listed in [16]. Starting from reference [17], there are five fundamental models on which all other models are based:

Parallel Model (Voigt Model) - λ_1 is first phase, λ_2 is second phase, f_1 is volumetric share of first phase and $f_2 = 1 - f_1$ is the volumetric of the second phase:

$$\lambda = f_1\lambda_1 + f_2\lambda_2, \tag{2.1}$$

Maxwell-Eucken Model (ME1) - λ_1 is continuous phase, λ_2 is dispersed phase:

$$\lambda = \frac{f_1\lambda_1 + f_2\lambda_2\frac{3\lambda_1}{2\lambda_1+\lambda_2}}{\lambda_1 + \lambda_2\frac{3\lambda_1}{2\lambda_1+\lambda_2}}, \tag{2.2}$$

Effective Medium Theory (EMT):

$$f_1\frac{\lambda_1 - \lambda}{\lambda_1 + 2\lambda} + f_2\frac{\lambda_2 - \lambda}{\lambda_2 + 2\lambda} = 0, \tag{2.3}$$

Maxwell-Eucken Model (ME2) - λ_1 is dispersed phase, λ_2 is continuous phase:

$$\lambda = \frac{f_2\lambda_2 + f_1\lambda_1\frac{3\lambda_2}{2\lambda_2+\lambda_1}}{\lambda_2 + \lambda_1\frac{3\lambda_2}{2\lambda_2+\lambda_1}}, \tag{2.4}$$

Series Model:

$$\lambda = \frac{1}{\frac{f_1}{\lambda_1} + \frac{f_2}{\lambda_2}}. \tag{2.5}$$

Each model presented by equations 2.1-2.5 is related to different microstructure. The corresponding microstructures are depicted in Figure 2.1. The heat flux flowing through the microstructures in this figure is assumed in the vertical direction.

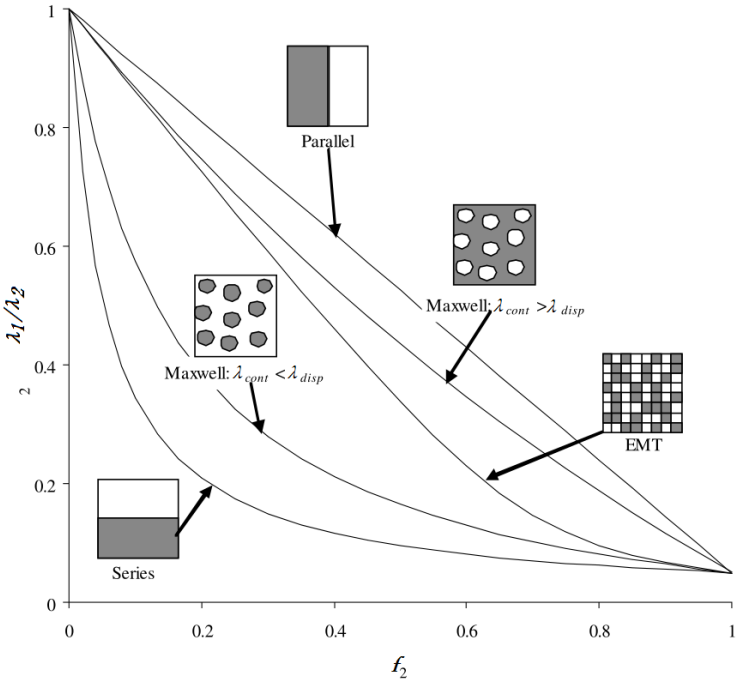

Fig. 2.1: Schematic overview of the structure of the five basic models (from [18], modified)

The Parallel model and the Series model are based on the rheological models of viscous materials. In the case that the matrix is a poor conductor and the additive is an excellent conductor, the Parallel model gives the highest values of composite's thermal conductivity and, in turn, the Series model gives the lowest values of composite's thermal conductivity. These models can be also derived using the resistance analogy from the field of electrical circuits.

The Maxwell-Eucken model (eqs. 2.2 and 2.4) is assumed that the second phase is randomly dispersed and fully embedded within the matrix. Moreover, this model can be found in more forms in the literature. For example, in the case of equation 2.2, following forms are possible [19]:

$$\frac{\lambda - \lambda_1}{\lambda + 2\lambda_1} = f_2 \frac{\lambda_2 - \lambda_1}{\lambda_2 + 2\lambda_1}, \tag{2.6}$$

$$\frac{\frac{\lambda}{\lambda_1} - 1}{\frac{\lambda}{\lambda_1} + 2} = f_2 \frac{\frac{\lambda_2}{\lambda_1} - 1}{\frac{\lambda_2}{\lambda_1} + 2}, \tag{2.7}$$

$$\lambda = \lambda_1 \frac{2\lambda_1 + \lambda_2 - 2f_2(\lambda_1 - \lambda_2)}{2\lambda_1 + \lambda_2 + f_2(\lambda_1 - \lambda_2)}, \tag{2.8}$$

$$\lambda = \lambda_1 \frac{1 + 2f_2 \frac{1-\frac{\lambda_1}{\lambda_2}}{\frac{2\lambda_1}{\lambda_2}+1}}{1 - f_2 \frac{1-\frac{\lambda_1}{\lambda_2}}{2\frac{2\lambda_1}{\lambda_2}+1}}. \tag{2.9}$$

Further, equation 2.2 can be simplified and used in practical applications. Some simplifications are presented here.

In the case of porous material with non-conductive pores, the equation 2.2 can be simplified to the form:

$$\lambda \ = \lambda_1 \frac{1 - f_2}{1 + \frac{f_2}{2}}. \tag{2.10}$$

In the case of powder composite (for example the green body prepared for sintering), the matrix is non-conductive. The equation 2.2 takes the following form:

$$\lambda \ = \lambda_1 \frac{1 + 2f_2}{1 - f_2}. \tag{2.11}$$

If there is more than one secondary phase within the matrix, the equation 2.2 can be expanded to the form:

$$\lambda = \lambda_1 \frac{1 - \sum_i f_i \frac{\lambda_1 - \lambda_i}{2\lambda_1 + \lambda_i}}{1 + \sum_i f_i \frac{\lambda_1 - \lambda_i}{2\lambda_1 + \lambda_i}}. \tag{2.12}$$

The EMT model was derived in 1935 by Bruggeman and sometimes is referred as the Böttcher model. It is the last fundamental model of possible composite microstructure. Its description, however, may be somewhat confusing. The EMT model represents a structure in which both phases (matrix and additive) can be in both forms - continuous and dispersed. At lower concentrations, the additive forms isolated particles and is fully surrounded by the continuous matrix. At intermediate concentrations, the particles of additive interconnect and create a continuous phase while in the meantime the matrix is still continuous. At high concentration of the additive, the additive begins to surround the initially continuous matrix phase and the matrix phase takes form of the isolated particles (the additive becomes matrix).

In contrast with the EMT model, the Maxwell-Eugen model assumes that the matrix still surrounds the additive grain even at high concentrations within the matrix. For this reason, the EMT model is sometimes denoted as the "mixture model" whereas the Maxwell-Eugen model is denoted as the "dispersion model". Groups of models derived on basis of these models (ME model and EMT model) have the same corresponding denotation.

The ME and EMT models are derived with the assumption that the perturbation of the flux caused by one particle does not reach the perturbation of the flux caused

by second particle. This condition is met at concentrations of the second phase below 10-15 % [20]. This limit is called "the dilute limit". To overcome the dilute limit in the case of dispersions, Bruggeman has derived a dispersion model which should be valid within the 0-100% range of additive concentrations. It has the following form:

$$1 - f_2 = \frac{\lambda_1 - \lambda}{\lambda_1 - \lambda_2} \sqrt[3]{\frac{\lambda_2}{\lambda}}. \tag{2.13}$$

In the reality, this model could only be applied to a particle concentration of no more than 70.04 volume percent, because this is the maximum packing density for spheres stacked in rhombohedral array [20].

This model can be also used for modelling the influence of porosity. If the thermal conductivity of the pore is zero, this model is simplified to [21]:

$$\lambda = \lambda_1 (1 - f_2)^{\frac{3}{2}}. \tag{2.14}$$

The Bruggeman model can be used for the pores of the shape of sphere. However, it can be further extended in order to consider other shapes of pores. This done by introducing the shape factor X:

$$\lambda = \lambda_1 (1 - f_2)^X, \tag{2.15}$$

where the factor X is expressed by:

$$X = \frac{1 - cos^2\alpha}{1 - F} + \frac{cos^2\alpha}{2F}, \tag{2.16}$$

where the F is the shape factor and α is the angle between the revolution axis of the spheroid and the non-perturbed heat flux [21]. Unfortunately, reference [21] does not give the exact formulae for calculation of F, it gives only numerical values and graphical representation of spheroidal particles - see Figure 2.2. This shape factor is a function of the axial ratio a/c of the main axis of spheroids. Specifically, for sphere ($a = c$) F is 1/3 while for oblate ($c > a$) and prolate ($a > c$) particles the F values are in the range of 0-1/3 and 1/3-1/2, respectively.

Obviously, that one should be careful with these models in the context porosity calculations. The point is that sometimes the reality may be different than initially expected. Work of Carson [18] reports this problem for the case of porous sandstone. At the first glance on the sandstone structure, the sandstone is the matrix and the pores containing air seem to be the second phase. In the reality, the microscopic picture reveals that the situation is opposite - the sandstone structure corresponds to the second phase and the interconnected air pores form the matrix.

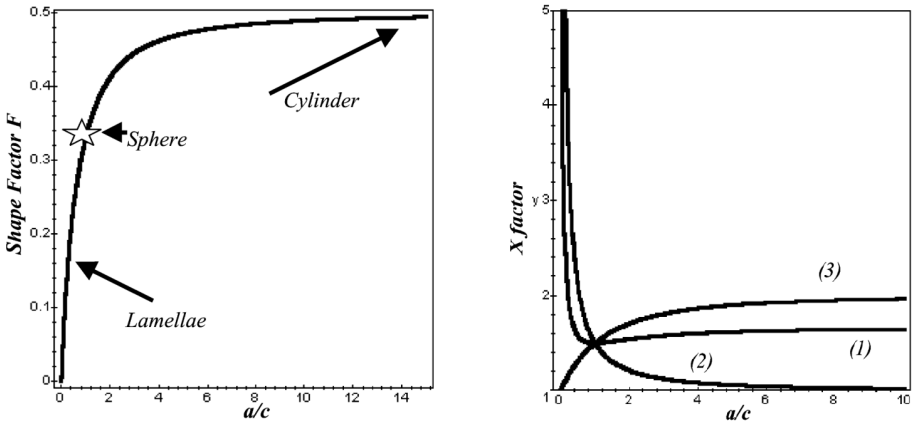

Fig. 2.2: The shape factor F and X factor [21]. Curve (1) - randomly oriented spheroids, curve (2) - spheroids oriented with the revolution axis a parallel to the heat flux, and curve (3) - spheroids oriented with the revolution axis a normally to the heat flux

To be completed, authors of [17] derived a sixth fundamental "Co-continuous model" in which both phases are continuous [22]. It can be even used for composites with more phases (let's say N) and it has a very simple form:

$$\lambda = \frac{\lambda_s}{2}\sqrt{1 + 8\frac{\lambda_p}{\lambda_s} - 1}, \tag{2.17}$$

where:

$$\lambda_s = \frac{1}{\sum_{i=1}^{N} \frac{f_i}{\lambda_i}} \tag{2.18}$$

$$\lambda_p = \sum_{i=1}^{N} f_i \lambda_i. \tag{2.19}$$

Regarding the application of these models in the composite nuclear fuel simulations, the reference [20] seems to be close to this topic. In this reference, the tungsten - uranium dioxide mixtures are investigated. For the spherical particles, reference [20] mentions the ME formula in the form of equation (2.8) but, due to its larger versatility, favors the Bruggeman formula (2.13) in a rearranged form:

$$\lambda = \lambda_p + (1 - f_2)(\lambda_1 - \lambda_2)\sqrt[3]{\frac{\lambda}{\lambda_1}}. \tag{2.20}$$

As mentioned above, this equation is applicable only up to 74.05 volumetric percent. Beyond this concentration of for lesser concentrations in which the particles are not uniformly distributed, reference [20] recommends the EMT model (equation 2.3).

2.1.2 TC Models for non-spherical particles

With some exceptions, the previously mentioned models describe the composites with spherical additives (regardless if in the form of a solid second phase or a pore filled with a vacuum). However, some materials of interest, for example carbon nanotubes or whiskers, are also being investigated as the additive to uranium dioxide. It makes it reasonable to introduce some models suitable for modelling of composites containing non-spherical particles. Reference [19] discusses these models in detail and is further used as main source of the models presented herein.

At first, the models derived purely for cylinders or platelets will be described. Introduction into more general models will follow.

Contrary to models with spherical additives, in the case of composite with non-spherical additives, the orientation of the particles to the heat flux plays an important role. If the cylinders are oriented parallel with the heat flux and parallel to each other, the Voigt model (eq. 2.1) can be used. If the cylinders are oriented perpendicular to the heat flux and parallel to each other, the Rayleigh model for dilute dispersions is recommended to be used:

$$\frac{\lambda - \lambda_1}{\lambda + \lambda_1} = f_2 \frac{\lambda_2 - \lambda_1}{\lambda_2 + \lambda_1}. \tag{2.21}$$

For mixtures with concentrations above dilute limit, following equation based on the Bruggeman's model is recommended to use:

$$f_1 \frac{\lambda_1 - \lambda}{\lambda_1 + \lambda} + f_2 \frac{\lambda_2 - \lambda}{\lambda_2 + \lambda} = 0. \tag{2.22}$$

For the randomly oriented cylinders several models are given too. For the case of thin and long cylinders presented as mixture within the matrix, Niesel derived the following model:

$$f_1 \left(\frac{\lambda_1 - \lambda}{\lambda} + \frac{4(\lambda_1 - \lambda)}{\lambda_1 + \lambda} \right) = f_2 \left(\frac{\lambda_2 - \lambda}{\lambda} + \frac{4\lambda_2 - \lambda}{\lambda_2 + \lambda} \right). \tag{2.23}$$

If the cylinders are presented as dispersion, following model (also derived by Niesel) is recommended (but both models should yield similar results):

$$1 - f_2 = \frac{\lambda_2 - \lambda}{\lambda_2 - \lambda_1} \left(\frac{\lambda_2 - 5\lambda_1}{\lambda_2 + 5\lambda} \right)^{\frac{2}{5}}. \tag{2.24}$$

The case of platelets will be discussed also because some theoretical studies assume, that graphene can be added into uranium dioxide for thermal conductivity enhancement.

In the case of composite with platelets, in which the platelets are oriented in a way that one diametric axis is parallel to the heat flux while the second diametric axis

is randomly oriented to the heat flux, the thermal conductivity of composite can be computed by:

$$\lambda = \sqrt{\lambda_p \lambda_s}, \tag{2.25}$$

where λ_p is given by equation (2.1) and λ_s is given by equation (2.5). The same parameters are also used in the mixture model for composite with randomly oriented platelets:

$$f_1 \left(\frac{2(\lambda_1 - \lambda)}{\lambda} + \frac{\lambda_1 - \lambda}{\lambda_1} \right) + f_2 \left(\frac{2(\lambda_2 - \lambda)}{\lambda} + \frac{\lambda_2 - \lambda}{\lambda_2} \right) = 0, \tag{2.26}$$

where

$$\lambda = \frac{1}{2}(-\lambda_s + \sqrt{\lambda_s^2 + 8\lambda_s \lambda_p}). \tag{2.27}$$

Finally, for the case of dispersion system with randomly oriented platelets, the following two models can be used:

$$1 - f_2 = \frac{2\lambda_2 + \lambda}{\lambda_2 - \lambda_1} \frac{\lambda_2 - \lambda}{2\lambda_2 + \lambda}) \tag{2.28}$$

$$\lambda = \lambda_2 \frac{3\lambda_2 + 2f_2(\lambda_2 - \lambda_1)}{3\lambda_2 - f_2(\lambda_2 - \lambda_1)} \tag{2.29}$$

2.1.3 Thermal conductivity models of composites with thermal barrier resistance

The model for thermal conductivity of composite with spherical inclusions and interfacial thermal barrier resistance was developed by Hasselman [23] at first and also by Nan [24] later on. The model has the form of:

$$\lambda_{eff} = \lambda_m \frac{2(\frac{\lambda_p}{\lambda_m} - \frac{\lambda_p}{ah_c} - 1)f + \frac{\lambda_p}{\lambda_m} + 2\frac{\lambda_p}{ah_c} + 2}{(1 - \frac{\lambda_p}{\lambda_m} + \frac{\lambda_p}{ah_c})f + \frac{\lambda_p}{\lambda_m} + 2\frac{\lambda_p}{ah_c} + 2,} \tag{2.30}$$

where λ stands for thermal conductivity, a is the radius of second phase particle and h_c is the interfacial thermal conductance, f is the volumetric share of the particles, and subscripts m and p refer to the matrix side and particle side. The subscript eff is related to the word effective and should not be confused with the effective multiplication coefficient related to the neutronic calculations.

Experiments with UO_2+SiC pellets [25] showed that predictions of this equation are in a good agreement with measured values for SiC content up to 20 vol.% and temperature range up to 900 °C

The interfacial thermal barrier resistance was estimated using the acoustic mismatch theory presented in [26]. The thermal barrier resistance is equal to the inverse of the interfacial conductance, which is approximately given by [27]:

$$h_c \approx \frac{1}{2}\rho_m c_m \frac{\nu_m^3}{\nu_p^2} \frac{\rho_m \rho_p \nu_m \nu_p}{\rho_m \nu_m + \rho_p \nu_p}. \tag{2.31}$$

In this equation, the ρ is the density, c_m is the specific heat of matrix, ν is the sound velocity. In the case that the particles are not of spherical shape, Hasselman and Nan model (eq. 2.30) is not suitable. For this reason, Nan has developed another model which considers not only the parameters given by eq. 2.30, but accounts also for the shape of the particles. Moreover, this model is also suitable for calculation of composites with coated particles. For this reason, the second Nan's model is widely used for calculation of thermal conductivity of composites containing carbon nanotubes and investigation of interfacial thermal barrier resistance in composites containing carbon nanotubes and similar dopants [28, 29, 30].

On the other hand, the Nan's model has three main drawbacks [31] for which it actually should not be applied in the calculations with such structures: 1) it cannot be applied for composites with nanosized particles, because the model is based on Fourier's law, which is not applicable when the particle size is of the order or smaller than the mean free path of the energy carriers, 2) it is not suitable for composites with metallic particles where the heat transport is not only due to the phonon gas but also due to the electron gas and their interactions... 3) It is just valid in the dilute limit, such that the interactions among the particles are not considered.

Ordonez-Miranda (further referred as Miranda only) has tried to overcome the three shortcomings mentioned above and developed another model which solves the problems. Although the derivation of the two models is different, Miranda has, basically, introduced so called electron-phonon coupling factor χ into the Nan's model. The coupling factor takes into the account the scattering between phonons and electrons and its influence on the composite thermal conductivity - see eq. 2.32. When the factor is neglected, Miranda's model can be reduced to the Nan's model. This is valid at least for the spheroidal particles [31].

$$\lambda_c = \frac{\lambda_e + \lambda_p}{\chi}. \tag{2.32}$$

Considering the utilization of Miranda model by UO_2, the main heat transport mechanism in UO_2 is phonon transport at lower temperatures. At higher temperatures, the electron heat transport is prevailing (see Figure 1.2 and description of equation 1.3). Thus, the coupling factor can be neglected for lower temperatures for sure. For higher temperatures, the determination of the coupling factor is out of scope this work and it will be neglected.

Still, there is still one drawback of the Nan's model which needs to be solved. Nan's model is suitable for materials with isotropic thermal conductivity, which is not the case of carbon nanotubes. The reported transverse thermal conductivity of carbon nanotubes is approximately 150-times smaller than the longitudinal thermal conductivity. This ratio was found in [32, 33, 34] but other references show different ratios. Solution of this problem is given in [35] where Miranda has simplified his model to calculate thermal conductivity of composite with coated nanofibers in dielectric matrix.

For simplicity, this work will present the model of composite with randomly oriented cylindrical particles coated with third phase. This model is schematically shown in Figure 2.3. For details on the model and its full derivation, please consult the reference [31]. The effective thermal conductivity is given by:

$$k_{eff} = k_m \frac{3 + f(2\beta_1 + \beta_3)}{3 - f\beta_1}, \tag{2.33}$$

with

$$\beta_3 = \frac{k_3}{k_m} - 1, \tag{2.34}$$

$$\beta_1 = 2\frac{1 - \frac{a_k}{a+\delta} - \frac{k_m}{k_1}}{1 + \frac{a_k}{a+\delta} + \frac{k_m}{k_1}}, \tag{2.35}$$

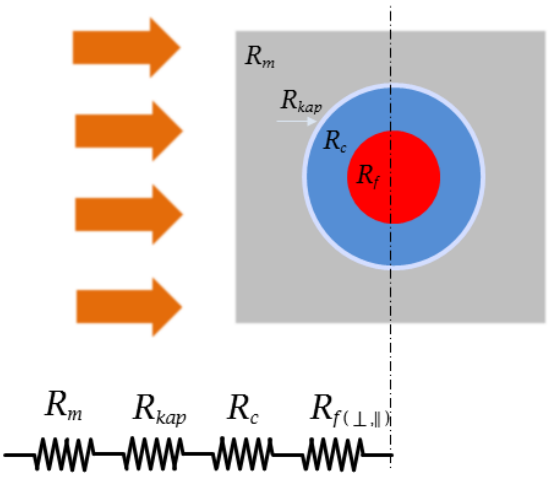

Fig. 2.3: The structure of the coated fiber within a matrix described by the Miranda model and its alternative description by current-resistance analogy. The heat flux is in horizontal direction.

where $R = 1/h_c$ is the interfacial thermal resistance, a is the radius of the cylindrical second phase, δ is the thickness of the coating, $a_k = R \cdot k_m$ is the Kapitza radius at the coating-matrix interface, and f is the volumetric share of the second phases. The Kapitza radius can be interpreted as the equivalent thickness of a layer of the matrix around the particle [31]. The thermal conductivity factors k_i are the merged thermal conductivity parameters of particle and coating. They are defined as:

$$k_1 = k_c \frac{2 + \alpha_1 \nu}{2 - \alpha_1 \nu}, \tag{2.36}$$

$$k_3 = k_c(1 + \alpha_3 \nu), \tag{2.37}$$

where k_c is the thermal conductivity of coating and ν is the relative fraction of second phase to coating given by:

$$\nu = \frac{a^2}{(a + \delta)^2}, \tag{2.38}$$

The dimensionless factors α_i account for the influence of transverse $k_\perp$ and longitudinal $k_\parallel$ thermal conductivities of the second phase. They are given by:

$$\alpha_1 = 2\frac{k_\perp - k_c}{k_\perp + k_c}, \tag{2.39}$$

$$\alpha_3 = \frac{k_\parallel}{k_c} - 1, \tag{2.40}$$

It should be noted, that equations for determinating TCC were used assuming that the interface between matrix and particle remains perfect. However, experiments determining the interphase stability UO_2-SiC fuel at high temperatures revealed that a substantial debonding starts to occur after approx. one month only. Therefore, strictly speaking, the interfacial thermal conductance should not be calculated using simply the equation 2.31.

The influence of particle - matrix debonding on the thermal conductivity can be incorporated into the computation using the model given in [23]. For simplicity, omitting of the debonging was done here with the following explanation: The particle-matrix debonding model requires the knowledge of pressure and composition of the gas surrounding the particle in the matrix (typically He with Kr and Xe). However, these parameters are a strongly influenced by the local temperature, fission gas release, burnup, and power history. In turn, local temperature is strongly determined by the thermal conductivity of the fuel which is calculated with the selected model. In order to determine all these parameters, multidimensional iteration process would have been required, while it was not certain if any significant contribution will be gained.

Besides, the cracking of the matrix was also neglected for simplicity. But in case of need, a suitable correlation describing the influence of pellet cracking on UO_2 thermal conductivity is presented in [36].

With this in mind, all calculations done with models for composite's thermal conductivity should be considered the best performance estimation. In other words, these calculations represent the upper boundary of real composite's thermal conductivity. The lower boundary is represented by the pure UO_2 thermal conductivity. Naturally, the real values of composite's thermal conductivity should be expected between these two limits. But some references mention that the composite thermal conductivity can reach even lower compared to the matrix thermal conductivity(!) due to the large thermal resistance at the phase boundary or due to the unpreferential orientation of the second phase particles.

So, another point worth discussing is the topic of the random orientation of particles, namely fibers, in the matrix. Generally, it is assumed that the fibers are dispersed randomly throughout the volume. The orientation of the cylinders is also random in the XYZ direction. However, pressing of the pellet can cause preferential orientation of the fibers in the radial direction (the degree or the axial orientation is decreased, and fibers are stacked in radial layers). This effect is also neglected in this work because the preferential heat flux is in the radial direction in which the random orientation of cylinders is maintained during pellet pressing. But in general, this effect should be positive for the heat transfer since the fibers are oriented in the center to periphery direction and thus help to transfer the heat out.

2.2 Candidate materials for thermal conductivity enhancement

In this subchapter, the different types of additives are introduced and their properties are discussed from different points of view. The emphasis is placed on the mechanical and thermal stability during production and operation and, next, on the availability of the material data usable for numerical modelling.

Figure 2.7 depicts the thermal conductivities of the candidate materials. Given the lack of data in some cases, the data on thermal conductivity is not complete especially at higher temperatures. In such cases, extrapolation had to be used assuming that the data trend is the same at higher temperatures as well. In this Figure , (1) the red stars represent measured data points, (2) the red line represents a valid temperature range of a model of single wall carbon nanotube (SWCNT) thermal conductivity, and (3) the black lines represent extrapolation of the data and the model. The origin of the data and model will be described next in detail because this thermal conductivity data is next used for comparison of the candidate materials.

The theory of degradation of the thermal conductivity under neutron irradiation is next worked out in Chapter 2.4.

2.2.1 Beryllium oxide

Starting from the oldest option, the UO_2+BeO fuel was patented in the seventies [37]. But in that time, the highly enriched UO_2 was assumed as the minor part of composite with BeO. In the nineties, the classical design of UO_2 pellet containing BeO has been investigated in [38] and it was found that the highest thermal conductivity is reached when the BeO is in the form of continuous phase. The next progress was made at Purdue University where a new fabrication process has been developed [39, 40] for production of dense UO_2+BeO (the former low density of such composite fuels was the main obstacle for a long period of time and thus no perspectives for this type of fuel were predicted). The production method of the UO_2-BeO lab-scale sample pellet is depicted in Figure 2.4. This fabrication method leads to the structure where the BeO is in the form of continuous phase – see Figure 2.5. It is told in [41] that this structure supports the integrity of the fuel during burnup and leads to lower FGR.

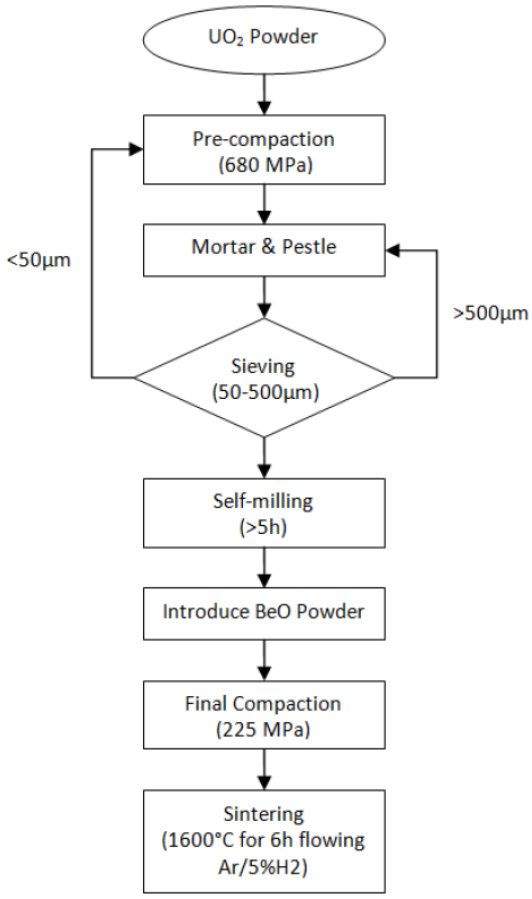

Fig. 2.4: Fabrication process flowchart of the UO_2+BeO pellet [41] (modified).

Fig. 2.5: The continuous BeO structure after removing the uranium [41].

The BeO is a perspective material from the point of view of high thermal conductivity. The neutron properties are also excellent. BeO was used as the moderator by some reactors in the past. The thermal stability with UO_2 is very good up to 2060 °C (see the phase diagram in Fig. 2.6). On the other hand, the main disadvantage is that BeO is a toxic and carcinogenic material. Author of this thesis finds this fact that it may be expected to be problematic from the point of view of public acceptance. There was also an economical study conducted in [42] which showed that, due to the high price of BeO, the UO_2-BeO fuel is economically beneficial when the discharge burnup is about 60 MWd/kg or more (under the market conditions in 2010). Another question arises from the preferred continuous phase of BeO while UO_2 is being encapsulated within this kind of matrix. The thermal expansion coefficient of BeO is significantly lower than that of UO_2 as presented in [43]. Considering this fact and the fact that there is a large increase in fuel temperature during LOCA accident (for example), a careful thermal stress analysis should be done for this type of fuel in order to investigate the structural integrity during accidents.

The investigation of the UO_2+BeO fuel is in advanced stage since this fuel has already been loaded into the Halden reactor with promising results in remarkable FGR decrease and lower centerline temperature [44].

The beryllium oxide data on unirradiated thermal conductivity was recommended in [45]. The data was fitted by the following function:

$$\lambda_{BeO} = \frac{444.3 \cdot T^2 - 1.583 \cdot 10^6 \cdot T + 1.909 \cdot 10^9}{T^2 + 1.452 \cdot 10^4 \cdot T + 9.838 \cdot 10^5}. \tag{2.41}$$

The validity range of this model and other models as well is clear from Figure 2.7.

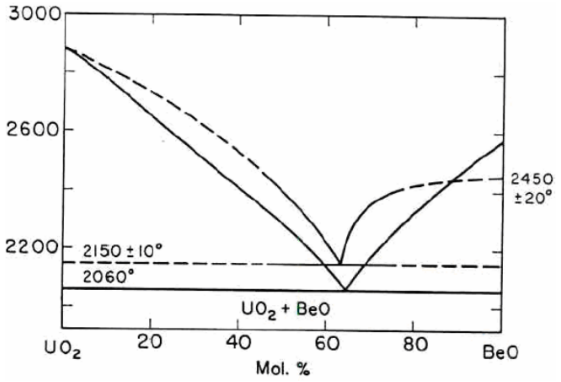

Fig. 2.6: Phase diagram of the UO_2 and BeO mixture, the temperature is in °C [40].

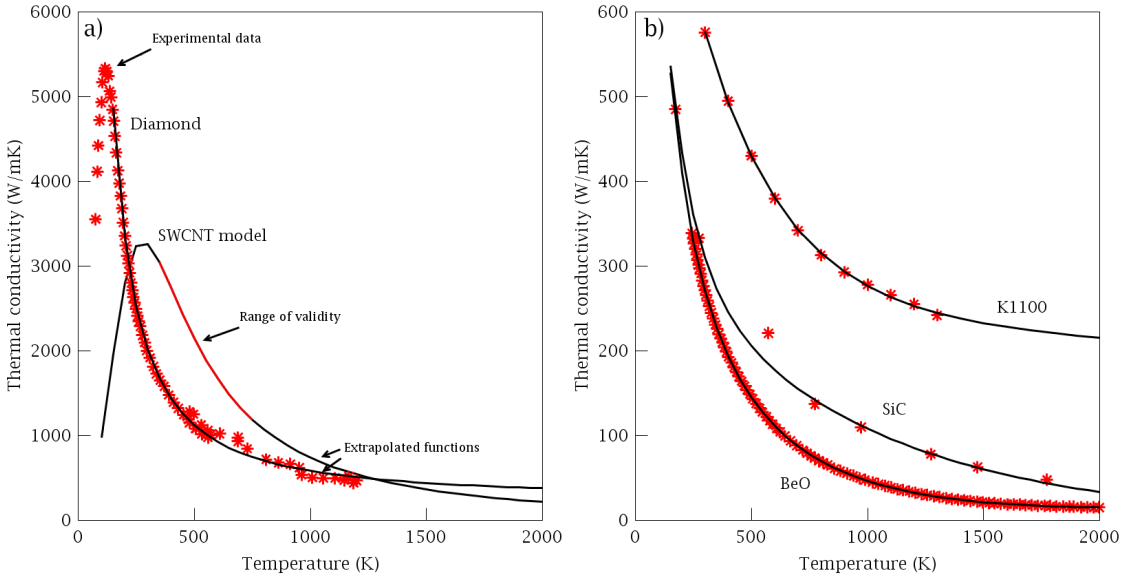

Fig. 2.7: Comparison of thermal conductivity of the candidate materials. The solid black lines are the extrapolated functions.

2.2.2 Silicon carbide

The first investigation of UO_2+SiC fuel option was done in [40] where the Polymer impregnation and pyrolysis method has been used. The problem was that this method provides low density pellets which are not suitable for reactor operation und thus this combination was rejected.

Later, series of articles [25, 46, 47] has been published which investigated this fuel option prepared by a new Spark Plasma Sintering (SPS) method. This fabrication method overcame the problem with lower density of UO_2+SiC which was faced in [40]. The SiC of two different forms was used as the additive - spheres and whiskers. The difference in morphology using traditional and SPS method is shown in Figure 2.8. Note the imperfect contact between matrix additive, especially by the classical sintering method.

It was expected that pellets containing SiC whiskers will pose higher thermal conductivity because the long SiC whisker should conduct the heat out of the pellet center to the surface. Apart from this expectation, the samples showed no significant difference in thermal conductivity. An example of the lab-scale production method is described in detail in ref. [25]:

The UO_2 and SiC powders were mixed in a ceramic vial with stainless steel balls and a blending aid, 2,3-dihydroperfluoropentane, and blended in a SPEX 8000 shaker for 1 h. The blended mixture was then dried up in a hood for at least 6 h to decompose the blending aid. ... SiC particles dispersed in UO_2 powders were then sintered using

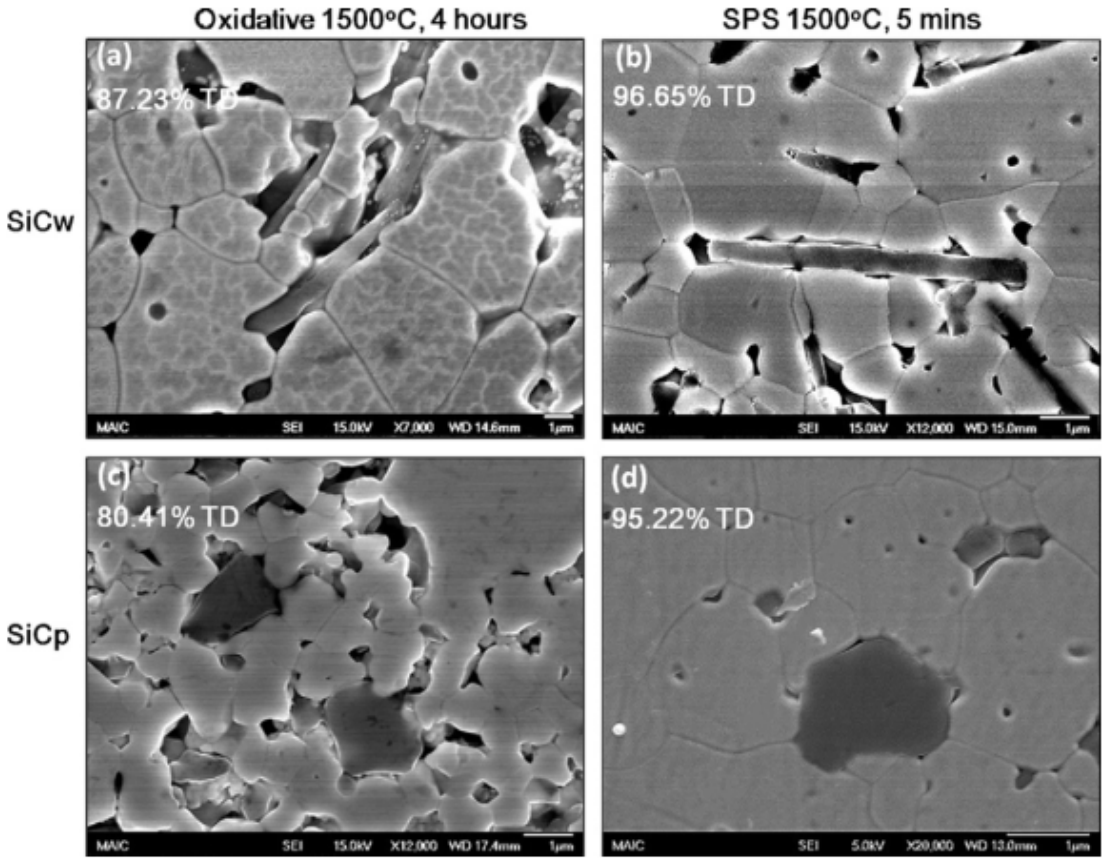

Fig. 2.8: The morphologies of UO_2 + 10 vol.% SiC (whiskers and particles) sintered by classical (oxidative) and SPS method [46].

a Dr. Sinter® SPS-1030 system at 1350 °C and 1450 °C for 5 min in a vacuum (30 m Torr). The ramp up/down rate and mechanical pressure at the maximum sintering temperature were held constant at 100 °C/min and 36 MPa, respectively.

The heat treatment procedure described in ASTM C 1430-07 was conducted on the sintered composite pellet to reduce UO_{2+x} to stoichiometric $UO_{2.0}$, which is known to have the optimum thermal properties. This process is also required to produce similar O/U ratio in all fabricated UO_2–SiC composites. The ramp up/down rate and maximum temperature were set at 2.6 °C/min and 800 °C, respectively. The heat treatment was performed in a Lindberg® alumina tube furnace using 4%H_2–N_2 gas with a dew point maintained at 35 °C.

SiC is a non-toxic material. It poses worse neutronic properties but higher thermal conductivity compared to BeO. See Figure 2.7 in which the thermal conductivity is presented. But, the chemical reaction between UO_2 and SiC begins at 1370 °C and the system is completely molten above 1700 °C, as experimentally confirmed in [39]. In contrast to that, reference [48] reports that there is no chemical reaction during sintering at 1300 °C and U_4Si_7 is formed during sintering at 1650 °C.

This finding is confirmed in [49] where *some reaction between SiC samples and UO_2 was observed at 1100 and 1300 °C, higher reactivity was seen in CVC SiC compared to that of CVD SiC*. In fact, even in the case of CVC SiC, the chemical reactivity was found to be minor for the two lower temperatures being investigated in this paper. Unfortunately, only the predicted (not measured) phase diagram was for the UO_2+SiC mixture. The near stoichiometric UO_2+SiC phase is depicted in Fig. 2.9 and the data presented confirm that eutectic is above 1908 °C. So, the UO_2+SiC composite fuel is considered chemically stable up to 1370 °C in this work and no melting is assumed up to 1650 °C.

The data on the thermal conductivity of SiC (the CVD SiC grade) were found in the flyer of the Rohm & Hass Company [50]. This material was selected as reference because it represents the commercially available material with thermal conductivity values reaching up to the values of SiC single crystal [51]. The experimental data on thermal conductivity was fitted with the following function:

$$\lambda_{SiC} = 920e^{(-0.008846 \cdot T)} + 349.1e^{(-0.001171 \cdot T)}. \tag{2.42}$$

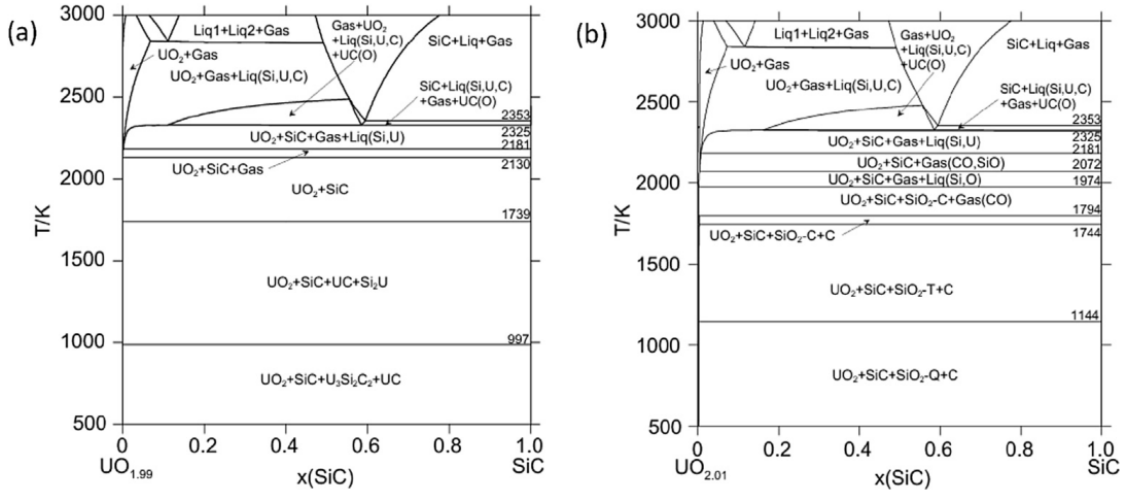

Fig. 2.9: The theoretical near stoichiometric UO_2+SiC phase diagrams as calculated in [15].

2.2.3 Carbon nanotubes

After the successful production of UO_2+SiC, the research at University of Florida changed its focus on the Carbon nanotubes [52]. The carbon nanotubes are a material which has recently been investigated in many applications, due to its superior mechanical and thermal properties. One of them is the extremely high thermal conductivity and thus it was reasonable to investigate the properties of UO_2+SWCNT (single wall carbon nanotubes).

The SPS method was utilized for the production of UO_2+SWCNT as well. The process is very similar to that used by UO_2+SiC fuel but the mixing process needed to be changed to avoid formation of graphite. The process consisted of two steps - sonication and homogenization. In the first step, the SWCNTs were dispersed in mixing liquid (preferably in ortho-dichlorobenzene). For the homogenization, SWCNTs were added to 200 ml of solvent and the suspension was then homogenized using an IKA2500 homogenizer. A sonication process followed this. A Qsonica3000 probe sonicator was used for 10 min at 40% amplitude. This two-step process yields a stable dispersion and the UO_2 power was then added into it while sonicated for an additional 5 min. To prepare the mixture for sintering, the liquid was then evaporated over 24 h at 60 °C.

In contrast to expectations, the effect of SWCN addition into UO_2 was unambiguous. The 5 vol. % concentration of SWCNT dispersed in matrix yields the best thermal conductivity enhancement (also probably due to the reported increase in theoretical density) but next increase in SWCNT concentration leads to significant decrease in thermal conductivity. The authors of [52] suspect the interactions between single carbon nanotubes to be the cause of this phenomena. Regarding this research, the author highlights that the thermal conductivity resistance at the matrix-dopant interface can be one of the roots of this problem. The increased number of SWCNT in the matrix introduces higher number of phase interfaces in the heat flux direction and thus, in turn, the presence of SWCN reduces the benefit of its high thermal conductivity.

There have been numerous works published on the thermal conductivity of carbon nanotubes but the problem with significant inconsistency in published data is faced here as well. Moreover, two types of thermal conductivity are defined in the case of nanotubes and fibers - axial and transverse. Both are needed for the next calculations.

The problem of lack of experimental data on thermal conductivity was solved by adopting the thermal conductivity model published in [53]. The advantage of this model is that it accounts for the temperature dependency up to 800 K and for the length L of the nanotubes. The length of nanotubes is given in micrometers in this

model. The ratio of axial to transverse thermal conductivity was estimated to be 150 because similar value was found in other references [54, 55, 56] despite to the fact that magnitudes of thermal conductivities measured there were significantly different. The model has the following form:

$$\lambda_{SWCNT} = (3.7 \cdot 10^{-7} \cdot T + 9.7 \cdot 10^{-10} \cdot T^2 + 9.3 \cdot (1 + 0.5/L) \cdot T^{-2})^{-1}. \quad (2.43)$$

2.2.4 Graphite fibers

The concept of the UO_2 pellet containing graphite fibers has been already suggested in [39] as well. This option was eliminated because the fibers start to react with UO_2 at 1400 °C forming UC and it was not possible to obtain high density pellets with traditional methods of sintering. This concept has been reintroduced in [57] where the SiC fiber coating was used in order to prevent the chemical reaction. From the current materials available on the market, the K1100 graphite fibers have the thermal conductivity even higher that of SiC [58]. References [59, 60] report that the K1100+SiC composites exhibit higher thermal conductivity than that of SiC even after neutron irradiation.

On the contrary, there is a question concerning the mechanical stability of such system comprising from UO_2-SiC-K1100. According to research conducted in [61], where composites comprised from carbon fibers and SiC matrix were irradiated by neutrons at 730 °C up to fluence of 9.3 dpa, the carbon fibers undergo dimensional changes leading to cracks in SiC matrix. Further material research in this area is necessary.

The data on K1100 graphite fibers was published in [58] but it is not clear from this reference, whether it is the bulk thermal conductivity or axial thermal conductivity. It is assumed in this work that this data concerns the axial thermal conductivity. The axial to transverse thermal conductivity ratio was set similar to that of SWCN for simplicity. The best fitting equation was found to be:

$$\lambda_{K1100} = 9779.820 \cdot e^{(-0.002858 \cdot T)} + 252.9 \cdot e^{(-8.686 \cdot 10^{-5} \cdot T)}. \quad (2.44)$$

2.2.5 Diamonds

The third type of the modified fuel developed at the University of Florida was that containing diamonds [62]. The diamond seems to be an excellent candidate as a dopant for thermal conductivity enhancement. It has the highest thermal conductivity reported at normal conditions and there is no risk of health damage while handling. Carbon has very low absorption of neutrons as well. Based on the results in [63], the UO_2 diamond doped fuel seems to have a good stability even at higher temperatures when after high temperature (1400 °C, 10 hours) test no debonding process of diamonds from UO_2 matrix has been observed. The thermal conductivity decrease after this test was found to be very low.

Basically, same SPS like in the case of UO_2 + SiC composite fuel was used for production. The UO_2 and diamond powders were pre-prepared by blending the UO_2 and diamond for one hour with a blending aid 2,3-dihydroperfluoropentane using the A SPEX-8000 shaker. In SPS, the green body was heat up by a temperature ramp rate of 100 °C/min to the maximum sintering temperature 1300 – 1600 °C, with a hold time of 5 min. The the maximum temperature was reached an axial pressure of 36 MPa was applied until the cooling process started. No heat treatment was applied to reduce the stoichiometry because the O/U stoichiometry was reduced by the reducing environment. The resulting structure is shown in Figure 2.10.

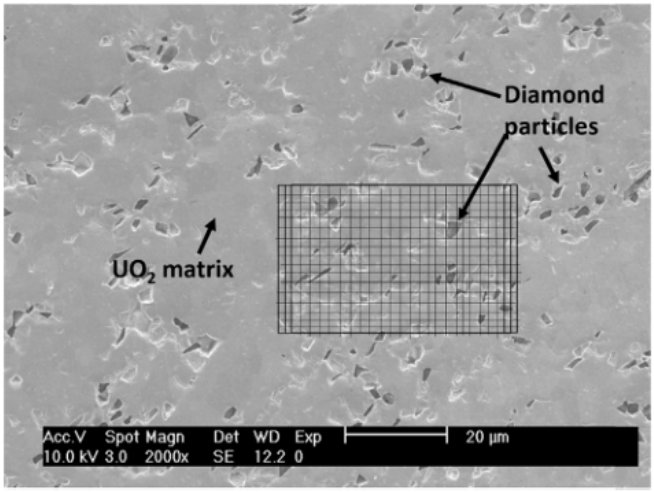

Fig. 2.10: The structure of the UO_2 + Diamond composite fuel. The grid locates the place where a Raman map scan was performed in [62].

On the other hand, even though the SPS needs a very short time to produce the ceramic body compared to traditional techniques, but some graphitization has been observed after sintering at 1400 °C for 5 minutes in the case of the UO_2+diamonds composite [64]. This may be explained by inaccurate measurement of the sam-

ple temperature. In any case, this is a considerable finding because the formation of graphite has a huge influence on the thermal and mechanical properties because the *specific volume of graphite is 1.55 times greater than that of diamond* [65]. In other words, due to the fact that BDBA are normally accompanied with high fuel temperatures, the subsequent graphitization could cause significant volume changes of fuel. This could degrade the core structure and core coolability.

The data on the thermal conductivity of diamonds was published in many references but significant inconsistency in data was found depending on diamond structure and isotopic composition. The scatter originates from different quality of the diamonds used for the measurement. To be consistent with the methodology applied for SiC, the CVD diamond grade was used as the reference data [66]. This data was supplemented by data on high quality natural diamond [67] which should share the same properties [68]. There is a general problem in the case of diamonds that the data on thermal conductivity at higher temperatures are difficult to obtain in the open literature. The extrapolation was necessary in this case.

$$\lambda_{Diamond} = 4.793 \cdot 10^6 \cdot T^{(-1.386)} + 251.6. \tag{2.45}$$

2.2.6 Graphene

The graphene is one of the most modern trend of material research and there are many applications in which the graphene seems to be useful in the future. Regarding the nuclear technology, the graphene is investigated as material suitable for extraction of uranium from seawater [69]. Regarding the accident resistant fuel technology, only the theoretical simplified thermal-hydraulic simulations have been found [70] and, to the author's knowledge, no research paper has been published where some material research was conducted.

The main reason for this may lie in the fact that graphene structure is very brittle, and it can be damaged or totally destroyed during mixing with UO_2 or during pellet compaction process. For this reason, this option will be not considered in the remaining parts of this work.

2.3 Thermal conductivity comparison of composite fuel options

Figure 2.11 shows how addition of 5 vol.% of the single additives gives rise to composite thermal conductivity. Although, the thermal conductivity of SiC is higher than that of BeO, the UO_2+BeO thermal conductivity is higher than that of UO_2+SiC. The root cause is the different structure of the UO_2+BeO where the BeO is in the form of continuous phase (see Figure 2.5) thereby significantly improving the thermal conductivity. All other second phases indicated in this figure are in the form of dispersion within matrix.

The data on the mixture UO_2+K1100 fibers has not been found and thus assuming that this concept has never been investigated. Thus, this composite mixture will be evaluated only theoretically in section 3.3.1. As expected, and in accordance with Figure 2.7, the UO_2+SWCNT and UO_2+diamonds composite exhibits the highest thermal conductivities. Please note that there is a crossing of thermal conductivity dependencies in Figures 2.7 and 2.11. The difference in crossing location between the two figures is approximately 200 K. The crossing may be considered as the evidence of the validity of thermal conductivities data (predictions) for SWCNT and diamond at higher temperatures. The shift can be attributed to the uncertainty in thermal conductivity of SWCNT and the unclear properties of composites based on UO_2. For both types of additives, the thermal barrier resistance between matrix and additive is also not well understood and thus this may play a role in the shift.

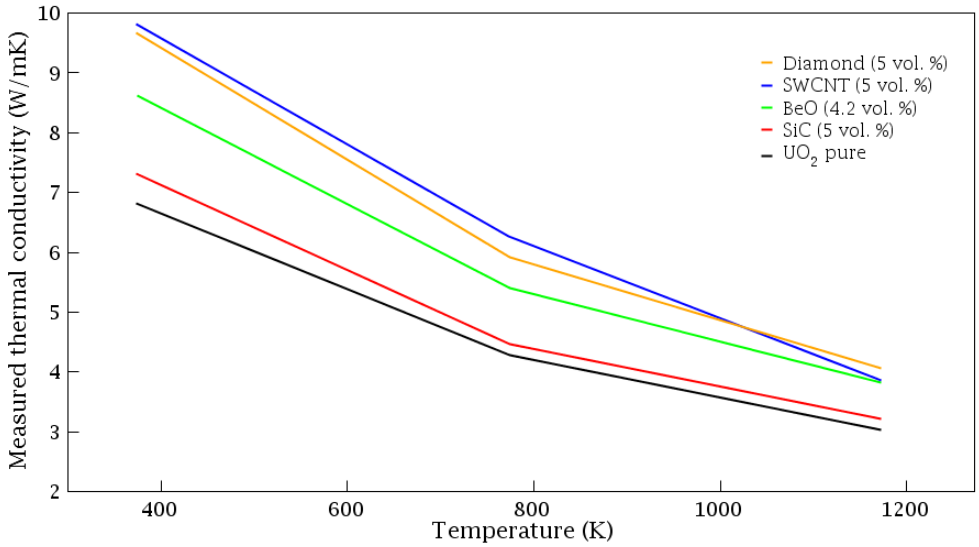

Fig. 2.11: The influence of addition of candidate materials on the composite thermal conductivity (graph was reconstructed based on [52, 63]).

Based on the thermal conductivity data in this chapter and on the summary of the thermal conductivity models in subchapter 2.1, further comparisons and evaluations is made in subhapter 3.3. This part of work is also completed with the information on degradation of thermal conductivity of individual candidates during irradiation with neutrons. The theory on this is presented within the next Subchapter 2.4.

2.4 Degradation of thermal conductivity of candidate materials under neutron irradiation

In the thermal-hydraulic calculations of the nuclear fuels with additives, the influence of the neutron irradiation on the thermal conductivity of additives is often neglected. Assuming that the major contribution of the additives is the thermal conductivity enhancement, the development of the thermal conductivity during neutron irradiation should be well understood before any calculations and analysis. This subchapter summarizes the publicaly available models whereas the own derived model of SiC degradation is derived in section 2.4.4.

2.4.1 Beryllium oxide

The Beryllium oxides is normally considered as radiation stable material and its thermal conductivity degradation under neutron irradiation has already been investigated in some extend. However, reference [44] provides an empirical correlation of the UO_2+BeO fuel thermal conductivity as a function of burnup and temperature as derived from the Halden experiments:

$$\lambda_{UO2-BeO} = \frac{1 + K_{BeO} \cdot V_{BeO}}{0.1148 + 0.0040 \cdot Bu + 2.475 \cdot 10^{-4} \cdot (1 - 0.00333 \cdot Bu) \cdot T} + 0.0132 \cdot e^{(0.00188 \cdot T)} \quad (2.46)$$

where Bu is the fuel burnup in MWd/kgUO_2, T is in °C, V_{BeO} is the volumetric fraction in %, and K_{BeO} is the technological factor which is equal to 0.03 if BeO is in the form of additive (particle) and to 0.05 if BeO forms the matrix (continuous phase).

2.4.2 Silicon Carbide

In case of SiC, the effect of neutron irradiation on material properties has been extensively described in [51] and a limited model of thermal conductivity degradation has been published in a presentation given by Katoh [71].

The model is based on the thermal defect resistance theory used in [72]. The thermal defect resistance ($R_{rd} = 1/\lambda_{rd}$) is defined as the difference in the reciprocal of the irradiated (λ_{irr}) and non-irradiated thermal conductivity ($\lambda_{non-irr}$):

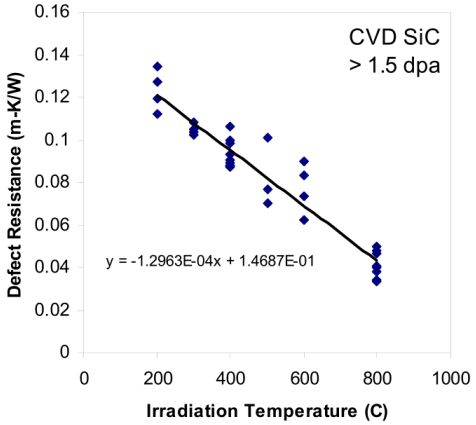

Fig. 2.12: The thermal defect resistance model developed by Katoh, as presented in [71]

$$R_{rd} = \frac{1}{\lambda_{irr}} - \frac{1}{\lambda_{non-irr}}. \qquad (2.47)$$

In this model, the R_{rd} is in Km/W and thermal conductivities λ_i are naturally in W/Km. From Figure 2.12, the model describing R_{rd} as a function of irradiation temperature T_{irr} solely is given by the equation 2.48:

$$R_{rd} = -1.2963 \cdot 10^4 \cdot T_{irr} + 0.14687, \qquad (2.48)$$

where T_{irr} is in °C. Figure 2.12 provides the information how this model was developed and the conditions of validity are also presented here.

The drawback of this model is that it accounts for the influence of irradiation temperature only (up to 800 °C) and the model is valid from the dose of 1.5 dpa. Author of this thesis has decided to develop a more detail model which will be valid in a wider temperature range and which will take into the account the influence of small dose irradiation. The new model is elaborated in section 2.4.4.

2.4.3 Carbon based materials

In the case of carbon-based materials (diamonds, SWCNT, K1100 fibers), very little information is available in order to establish a sufficiently accurate model of the thermal conductivity degradation. For example, Figure 2.13 provides a clear evidence that neutron irradiation has a deteriorating effect on the thermal conductivity of diamonds. A result similar to this one was reported for CVD diamond as well in [73]. But high temperature data is not available in the public literature. No data on K1100 and SWCNT was found regarding their thermal conductivity degradation by neutron irradiation.

Regarding the carbon-based materials, the most investigated and most familiar material is the graphite while there is little knowledge of other materials. This is due to the long history of using the graphite as a moderator in nuclear reactor technology. Similarly to SiC, the irradiation temperature has a strong influence on the thermal conductivity degradation [75], see Figure 2.14.

According to reference [76], the thermal defect resistance approach can be utilized even in the case of graphite materials. However, Figure 2.14 provides the data in the relative form and the thermal conductivities are measured at ambient temperature. Thus, Figure 2.14 cannot be used for the mapping of the thermal defect resistance. For this reason, the simplified model of Snead was utilized in order to show the influence of irradiation on thermal conductivity of graphite [77, 78].

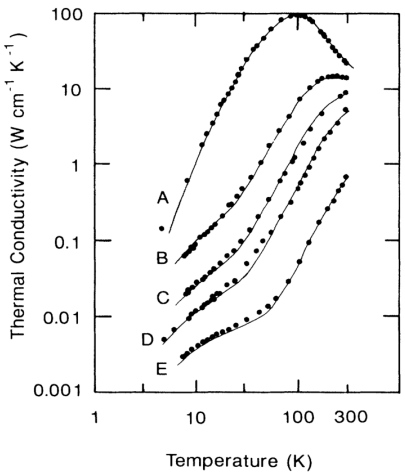

Fig. 2.13: Change in thermal conductivity of single-crystal diamond after fast neutron irradiation [74]. Curve A - nonirradiated, curve B - irradiated with fluence 3.0×10^{16} neutrons/cm^2, curve C - irradiated with fluence 1.2×10^{17} neutrons/cm^2, curve D - irradiated with fluence 6.0×10^{17} neutrons/cm^2, curve E - irradiated with fluence 4.5×10^{18} neutrons/cm^2.

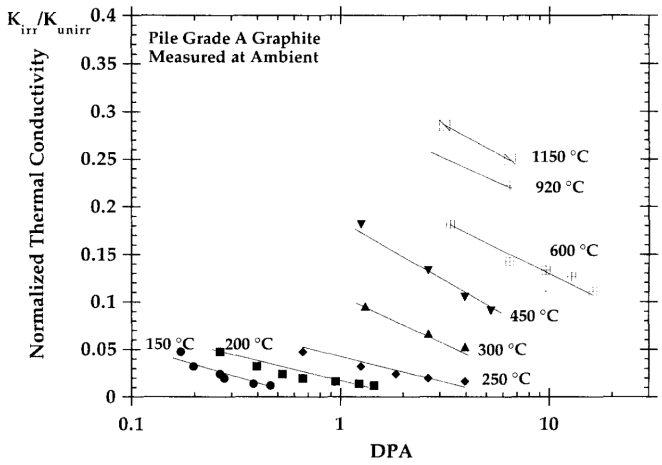

Fig. 2.14: The degradation of normalized thermal conductivity irradiated at several fluences and temperatures ([75], modified).

The Snead's model is graphically represented in Figure 2.15 and is given by an equation representing the ratio of irradiated and non-irradiated material:

$$\frac{\lambda_{irr}}{\lambda_{non-irr}} = (0.25 - 0.00017 \cdot T_{irr}) \cdot A \cdot log(F) + 0.000683 \cdot T_{irr}, \tag{2.49}$$

where T_{irr} is in °C and F is the fluence in dpa. The conversion factor between the dpa and MWd/kgU is derived in section 2.4.4 together with the conversion factor of SiC. One can see in Figure 2.15 that the thermal conductivity degradation is the most severe at lower temperatures. This finding is in a very good agreement with data presented in Figure 2.14.

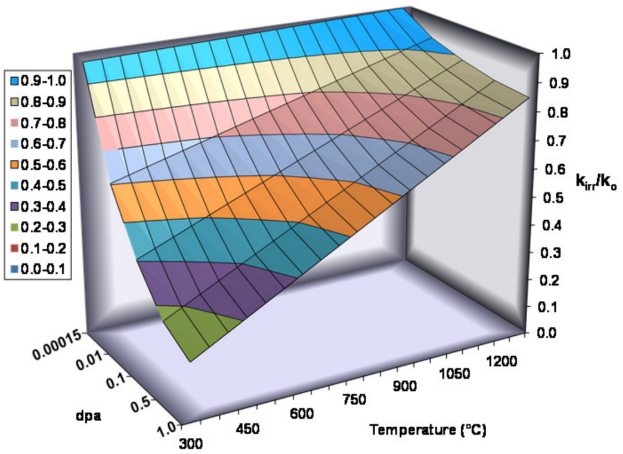

Fig. 2.15: Graphical interpretation of the Snead's model showing its dependence on neutron fluence and irradiation temperature [78].

2.4.4 New model of Silicon Carbide

In many references which deal with the modelling of UO_2+SiC fuels, the influence of neutron irradiation on the SiC thermal conductivity is omitted. Here, a simple model of SiC thermal conductivity degradation was developed by author. The details are not presented here since the model is going to be published in an impacted article later on. The full derivation of the model is presented in the proprietary version of the Ph.D. thesis.

The model is based on the thermal defect resistance theory represented by equation 2.47. The here developed models has the following form:

$$R_{rd,SiC} = f(F, T_{irr}) \cdot g(T_{irr}), \tag{2.50}$$

where T_{irr} is the irradiation temperature, and F is the fluence in DPA.

The function is based on i) experimental data reported on the thermal defect resistance of SiC, and on 2) the known behavior of the SiC thermal conductivity under neutron irradiation. There is a steep increase in thermal conductivity degradation for small doses. This phenomenon is enhanced at lower temperatures. At higher temperatures, where the lattice defects caused by neutron irradiation recombines, the thermal conductivity increase is much smaller. The next phenomenon is that the thermal defect resistance becomes constant from some fluence level.

This is why the model 2.50 is constructed as multiplication of two functions. The first function represents the steep increase in thermal defect resistance and its influence vanishes at higher fluences. The second function is dependent on the irradiation temperature and represents the fact at higher temperatures the increase in thermal defect resistance is smaller.

2.5 Material property models

Throughout this work, many calculations are done in order to compare the nuclear fuel options and the additives from different perspectives. For the sake of completeness, this subchapter simply summarizes all the models.

The thesis presents the UO_2 material property models as it is the basic material used in all computations. It then proceeds to presenting and focusing on the SiC material property models since this work focuses on it as the base case additive in the FEMAXI analysis of the composite UO_2 + SiC fuel. The models on other materials (BeO, SWCNT, Diamonds) are limited to density and specific heat only. The thermal conductivity functions of all the candidate materials were presented in the subchapter 2.2.

2.5.1 Density

The UO_2 density as a function of temperature was modelled with the model presented in [90, 91]:

$$\rho_{UO2} = \rho_0 \cdot K_i^{-3} \tag{2.51}$$

where ρ_0 is the full dense UO_2 (10 960 $kg \cdot m^{-3}$) and the temperature dependent term K_i is expressed as follows:

$$K_i = \begin{cases} K_1 = 0.99734 + 9.802 \cdot 10^{-6}T - 2.705 \cdot 10^{-10}T^2 + 4.291 \cdot 10^{-13}T^3 \\ K_2 = 0.99672 + 1.179 \cdot 10^{-5}T - 2.429 \cdot 10^{-9}T^2 + 1.219 \cdot 10^{-12}T^3 \end{cases} \tag{2.52}$$

The K_1 term is valid at 273 $K \leq T \leq$ 923 K and the K_2 term is valid in the range 923 $K \leq T \leq$ 3120 K.

In the case of SiC, the density model was found using the temperature dependent lattice parameter data from [92] as recommended in [93]. This data was then recalculated to the volume of unit cell V and the density function was then determined using the simple function [94]:

$$\rho = \frac{4 \cdot M}{N \cdot V}, \tag{2.53}$$

where M is the gram formula weight (40.09715) and N is the Avogadros's number. This density function is limited by the maximum temperature of 1500 K.

The beryllium oxide model of density was found in [91]. The model is given by:

$$\rho_{BeO} = \rho_0 \cdot (1 - 3\alpha t), \tag{2.54}$$

where ρ_0 is 2870 kg·m^{-3}, t is temperature in °C, and α is the coefficient of linear thermal expansion in 1/K. This model should be valid up to 2000 K.

The same procedure was used in the case of SWCNT. The coefficient of radial linear thermal expansion α was found in [95] and approximated by the following function (in 10^{-6}K^{-1}):

$$\alpha = \frac{1.675 \cdot 10^4 \cdot T - 6.047 \cdot 10^6}{T^2 + 754.7 \cdot T + 2.273 \cdot 10^6}. \tag{2.55}$$

The ρ_0 is found to be 1984.5 kg·m^{-3} [96]. The validity of this equation is up to 1600 K.

The density model of diamond was derived in a similar way. The diamond molar density up to 3000 K was found in [97]. It was recalculated and fitted by the following density function (in g·cm^{-3} according to the source data):

$$\rho_{diamond} = \frac{1}{1.946 \cdot 10^{-15}T^4 - 1.583 \cdot 10^{-11}T^3 + 4.958 \cdot 10^{-8}T^2 - 1.373 \cdot 10^{-5}T + 3.417}. \tag{2.56}$$

2.5.2 Specific heat

Specific heat of UO_2 was found as [90]:

$$c_{pUO2}(T) = \frac{C_1(\frac{\theta}{T})^2 exp(\frac{\theta}{T})}{(exp(\frac{\theta}{T}) - 1)^2} + 2C_2T + \frac{C_3E_a exp(\frac{-E_a}{T})}{T^2} \tag{2.57}$$

Parameters which were used in the equation 2.57 are listed in Table 2.1:

Constant	**Value**	**Unit**
C_1	302.27	J·kg^{-1}·K^{-1}
C_2	8.463·10^{-3}	J· kg^{-1}·K^{-2}
C_3	8.741·10^7	J· kg^{-1}
θ	548.68	K
E_a	18 531.7	K

Tab. 2.1: Parameters of the c_{p,UO_2} function given by eq. 2.57

The data on SiC specific heat was found in the NIST database [98]. However, the data was fitted with the following polynomial function:

$$c_{p,SiC} = 251.07 + 2.0273 \cdot T - 1.172 \cdot 10^{-3} \cdot T^2 + 7.306 \cdot 10^{-7} \cdot T^3 - 1.192 \cdot 10^{-10} \cdot T^4. \quad (2.58)$$

The BeO model of heat capacity is recommended in [91]:

$$c_{p,BeO} = \begin{cases} 1.455 + 0.606 \cdot 10^{-3} T - 0.544 \cdot 10^{-5} T^{-2} & T \leq 1200K \\ 1.791 + 0.210 \cdot 10^{-3} T & T > 1200K \end{cases} \quad (2.59)$$

Regarding the SWCNTs, the volumetric heat capacity in cal·mol^{-1}K^{-1} can be found in [99]:

$$c_{v,SWCNT} = \frac{5.935T^2 - 463.6T + 8678}{T^2 - 92.09T + 1.865 \cdot T^5}, \quad (2.60)$$

In order to convert it into the kJ·kg^{-1}K^{-1} unit, this function must be multiplied with density and cal to J factor. The validity of this model is up to 1600 K.

The Gustafson model of specific heat for diamond [100] is used in this work. It calculates the specific heat in J·K^{-1}.

$$c_{p,diamond} = 24.3 + 9.446 \cdot 10^4 \cdot T - 5.396 \cdot 10^6 \cdot T^{-2} + 1.566 \cdot 10^9 \cdot T^{-3} - 1.332 \cdot 10^{11} \cdot T^{-4}. \quad (2.61)$$

2.5.3 Young's modulus

The temperature dependence formulae for Young's modulus was found in [101]:

$$E_{UO2} = 23.34 \cdot 10^{10} \cdot (1 - 1.091510^{-4} T) \cdot (1 - 2.752P), \quad (2.62)$$

with porosity P defined as one minus theoretical density (TD):

$$P = 1 - TD \quad (2.63)$$

Young modulus of SiC was found in [102]. The result is in (GPa).

$$E_{SiC} = 428.3 \cdot -0.04 \cdot T \cdot e^{-962/T}, \quad (2.64)$$

2.5.4 Poisson's ratio

The value of Poisson's ratio of UO_2 is assumed constant and equal to $\nu_{UO_2} = 0.316$ [101]. Similarly, the Poisson's ratio of SiC is determined as constant and equal to be 0.21 as recommended in [51] for CVD SiC.

2.5.5 Thermal conductivity

There are many models of UO_2 thermal conductivity. A very wide summary is given in [103]. From the list given in this reference, the MATPRO model was selected as the best fitting to the demands posed in this work. This model considers the influence of temperature, gadolinia content, and burnup. The model has the form:

$$k_{95,UO_2} = \frac{1}{term0 + term1 + term2 + term3 + term4 + term5} + term6 \qquad (2.65)$$

with:

$$\begin{aligned}
term0 &= 0.0452, \\
term1 &= 0.000246 \cdot T, \\
term2 &= 0.00187 \cdot Bu, \\
term3 &= 1.1599 \cdot Gdcon, \\
term4 &= (1 - 0.9 \cdot exp(-0.04 \cdot Bu)) \cdot 0.038 \cdot Bu^{0.28}, \\
term5 &= 1/(1 + 396 \cdot exp(-6380/T)), \\
term6 &= 3.5e9/T^2 \cdot exp(-16360/T),
\end{aligned}$$

where T is temperature in K, Bu is burnup in MWd/kgU, and $Gdcon$ is gadolinia concentration in $\%_W$. The subscript denotes the 95 % theoretical density for which the MATPRO model is primarily intended. But reference [103] also gives a simple correction formula for recalculation the initial thermal conductivity of UO_2 to desired final density.

$$k_{UO_2} = k_{95,UO_2} \cdot \frac{1.0789 \cdot D}{1 + 0.5 \cdot (1 - D)}, \qquad (2.66)$$

where D stands for fractional TD. According to [103], the MATPRO model is valid for the following conditions:

$$\begin{gathered}
300 \leq T \leq 3000\ K \\
0 \leq Bu \leq 62\ MWd/kgU \\
0.92 \leq D \leq 0.97 \\
0 \leq Gdcon \leq 10\ wt.\%
\end{gathered}$$

The models of thermal conductivity of other materials are introduced in the previous subchapter 2.2.

2.5.6 Coefficient of thermal expansion

The coefficient of thermal expansion (CTE) was mentioned several times within this subchapter but it was used in the connection with density calculations. In this section, the CTE of UO_2 and SiC are mentioned specially because they are used within the FEMAXI predictions in subchapter 5.3. The FEMAXI, however, requires the linear heat expansion coefficient in different form of L/L_0.

In the case of UO_2, The Martin's model [104] was used, where the initial length L_0 was measured at 273 K:

$$\frac{L}{L_{273}} = \begin{cases} 0.99734 + 9.802 \cdot 10^{-6}T - 2.705 \cdot 10^{-10}T^2 + 4.391 \cdot 10^{-13}T^3 & 273 \leq T \leq 923K \\ 0.99672 + 1.179 \cdot 10^{-5}T - 2.429 \cdot 10^{-9}T^2 + 1.219 \cdot 10^{-12}T^3 & 923K < T. \end{cases} \tag{2.67}$$

In the case of SiC, the relative linear heat expansion coefficient was derived using the definition of instantaneous linear heat expansion coefficient:

$$\alpha = \frac{1}{L}\frac{dL}{dT}. \tag{2.68}$$

For SiC, reference [51] recommends using α equal to $4.4 \cdot 10^{-6}$/K at $298 \leq T \leq 1273\ K$, and $5.0 \cdot 10^{-6}$/K above this limit. Eq. 2.68 was analytically solved with these values of α and the data was fitted with a single linear function in order to prevent numerical instabilities due to the inconsistency at the temperature threshold. The fitted function has the form:

$$\frac{L}{L_{298}} = -0.001825 + 5.094 \cdot 10^{-6} \cdot T. \tag{2.69}$$

The upper temperature limit of α is not given in [51].

3 Modelling the composite fuel performance

3.1 The methodology

The aim of this thesis is to investigate the performance of the composite nuclear fuel during normal operation and accidents. This kind of study requires mainly a thermo-mechanical analysis of the nuclear fuel performance. A brief neutronic analysis is applied here but is not of the main interest.

Subchapter 2.2 lists the most promising candidate materials which are proposed as the additives into the UO_2. In order to be able to asset the influence of fuel additives on the accident management, one must have mathematical models describing the evolution of the main fuel parameters during the burnup in reactor. The main parameter here is the thermal conductivity of the composite fuel. This is why the mathematical models of TCC were introduced within the second chapter. Together with the material models introduced in the same chapter, the models for prediction of TCC are then verified in the following subchapters.

In subchapter 3.2, a basic comparison of the fuel concepts is performed. The main parameter is the k_∞ as a function of burnup. However, it must be noted here that the results coming from this section are considered as indicative only since this thesis deals mainly with thermo-mechanical of the fuel and the consequent influence on the thermo-mechanical behavior of the nuclear reactor. This is why the results of this section were not considered during the selection of the representative candidate material.

In subchapter 3.3, basic comparison is made which compares the different fuels from the point of view of maximum $LHGR$ and energy stored within the fuel. This section is then followed by subchapter 3.4 where a representative candidate material is selected for detail analysis.

3.2 Composite fuel neutronic performance

Neutronic performance is the most essential characteristics regarding the nuclear fuel. There are many neutronic parameters which must be determined before the fuel is loaded into reactor, e.g. effective multiplication factor (k_{eff}) during burnup, reactivity coefficients or power peak distribution. These effects are inevitably bounded with thermo-mechanical behavior of the fuel. For this reason, a short chapter is placed here which compares the different composite fuel options with respect to infinite multiplication factor k_∞. The UWB code used in this chapter is briefly introduced in subchapter 4.3 together with other codes used in this work.

3.2.1 The four-factor formula

Simply said, the k_∞ provides the information on the neutronic balance within the infinite core. This parameter can be calculated using the four-factor formula, which basically describes the options what can happen with a neutron during its life within a core. The four-factor formula is defined as multiplication of four factors. Their definitions are taken mainly from [105]). The infinite multiplication coefficient is defined as

$$k_\infty = \epsilon p f \eta, \tag{3.1}$$

where ϵ is the fast fission factor, p is the resonance escape probability, f is the thermal utilization factor, and the η is the reproduction factor. The fast fission factor ϵ is given by eq. 3.2 and takes into the account, that some of the neutrons are yielded from the fast fissions:

$$\epsilon = \frac{\text{number of fast neutrons produced by all fissions}}{\text{number of fast neutrons produced by thermal fissions}}. \tag{3.2}$$

While the neutrons are being slowed down during moderation, some of them can be captured at ^{238}U. The probability that this does not happen is called the resonance escape probability p and a simple definition is given by eq. 3.3. This factor is strongly influenced by the fuel-moderator ratio and by the fuel enrichment.

$$p = \frac{\text{number of neutrons that reach thermal energy}}{\text{number of fast neutrons that start to slow down}}. \tag{3.3}$$

When the neutrons are slowed down to thermal energies, some portion of the neutron population is absorbed by the fuel and the rest is absorbed by other materials presented within the core. The efficiency how the neutrons are absorbed within the fuel is described by the thermal utilization factor:

$$f = \frac{\text{number of thermal neutrons absorbed in the fuel}}{\text{number of thermal neutrons absorbed in all reactor materials}}. \tag{3.4}$$

The reproduction factor (η) is the last component of the four-factor formula. It considers, that some of the neutrons absorbed within the fuel does not cause the fission and are absorbed only. Moreover, this factor considers the fact, that after fissioning, 2-3 neutrons appear from the fissioned nucleus. The definition of this factor is:

$$\eta = \frac{\text{number of fast neutrons produced by thermal fission}}{\text{number of thermal neutrons absorbed in the fuel}}. \tag{3.5}$$

Despite the fact that the theory of the four factor formula should be more worked out for full understanding of this topic, author of this thesis has decided for limited description only. Instead of that, if one is interested in deeper mathematical understanding of the four factor formula, author of this thesis recommends to go through the references [105, 106] where a nice insight into this topic is given. The data [105, 106] could not be directly used in this work because the analysis were performed with different codes and models.

3.2.2 UWB composite fuel model

The sample input deck number 3 from the UWB code distribution has been modified for the purpose of the neutronic study. This model is based on the VVER-1000 fuel pin geometry. Figure 3.1 illustrates the fuel pin geometry including the lattice pitch (the triangular arrangement is not shown here). The fuel gap is not included in this model. This is done probably due to the fact that its omitting is a common practice as it affects the results very little [106].

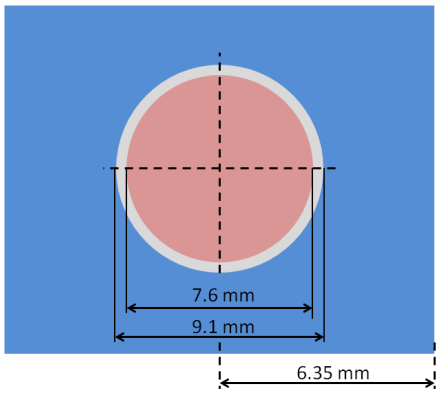

Fig. 3.1: The 2D geometry of the fuel pin used for the neutronic calculations

Six cases of the isotopic composition of the composite fuel were analyzed. The isotopic composition of each case is listed in Table 3.1.

1. The case 1 represents the standard UO_2 fuel with enrichment 4.95 % and 95 % TD. This base case was then used as the platform for the other cases as follows.
2. The case 2 represents the fuel where 10 vol.% of the fuel volume is removed (this corresponds to a fuel with 85.5 % TD).
3. The case 3 represents the composite fuel with 10 vol.% BeO.
4. The case 4 represents the composite fuel with 10 vol.% SiC.
5. The case 5 represents the composite fuel with 10 vol.% Carbon with density of 2.1 g·cm^{-3} which is also very close to the density of SWCNT - see section 2.5.1.
6. The case 6 represents the composite fuel with 10 vol.% Diamond with density of approx. 3.5 g·cm^{-3}.

	Case 1 UO_2-95% TD	**Case 2** UO_2-85.5% TD	**Case 3** UO_2+BeO	**Case 4** UO_2+SiC	**Case 5** UO_2+C	**Case 6** UO_2+C
U238	2.243E-02	2.018E-02	2.018E-02	2.018E-02	2.018E-02	2.018E-02
U235	1.183E-03	1.064E-03	1.064E-03	1.065E-03	1.065E-03	1.065E-03
U234	1.440E-06	1.296E-06	1.296E-06	1.296E-06	1.296E-06	1.296E-06
O16	4.720E-02	4.247E-02	4.975E-02	4.248E-02	4.248E-02	4.248E-02
O17	1.794E-05	1.615E-05	1.891E-05	1.615E-05	1.615E-05	1.615E-05
Be9	-	-	7.272E-03	-	-	-
Si28	-	-	-	4.446E-03	-	-
Si29	-	-	-	2.257E-04	-	-
Si30	-	-	-	1.491E-04	-	-
C12	-	-	-	4.769E-03	1.053E-02	1.755E-02

Tab. 3.1: Isotopic composition of the tested cases (in $at \cdot b^{-1} \cdot cm^{-1}$)

In input deck no. 3, the original burnup scenario consists of 43 depletion intervals (time steps) which were equal in the irradiation power (40 MW/MTU) but different in length. The four initial time steps are equal to 1 day. The next 4 time steps are equal to 5 days, the next 18 time steps are equal to 12.5 days and the rest of the time steps is equal to 62.5 days. This setting leads to final fuel burnup of 50 MWd/kgU. In order to see the effect of fuel addition on long term operation, four extra 62.5 days steps were added to reach the final burnup 60 MWd/kgU.

3.2.3 UWB neutronic results

Several effects of the second phase addition should be taken into account when analysing the k_∞ evolution: the fuel volume is reduced, the fuel temperature is decreased and some compounds contribute to neutron balance by neutron moderation or multiplication.

Unfortunately, the UWB code is not able to compute the four factors from the four-factor formula. Moreover, only the nuclear data libraries for 293, 600, 900, and 1200 K are available in this code so the fuel temperature effect could not be investigated. However, using the references [106, 107] dedicated to neutronic analysis of UO_2+BeO and UO_2+SiC composite fuels, it was possible to explain details of the k_∞ behavior. The k_∞ evolution of the cases listed in Table 3.1 is presented in Figure 3.2.

Figure 3.2a shows the comparison of the standard UO_2 fuel with the Case 2, where 10 vol.% of the fuel volume is removed. The k_∞ curves are very close together and thus difficult to distinguish them. For this reason, the Figure 3.2b compares the data in the relative form, where all the data are related to Case 1. The same is valid for Figures 3.2c and 3.2d, where the standard UO_2 fuel is compared to other cases.

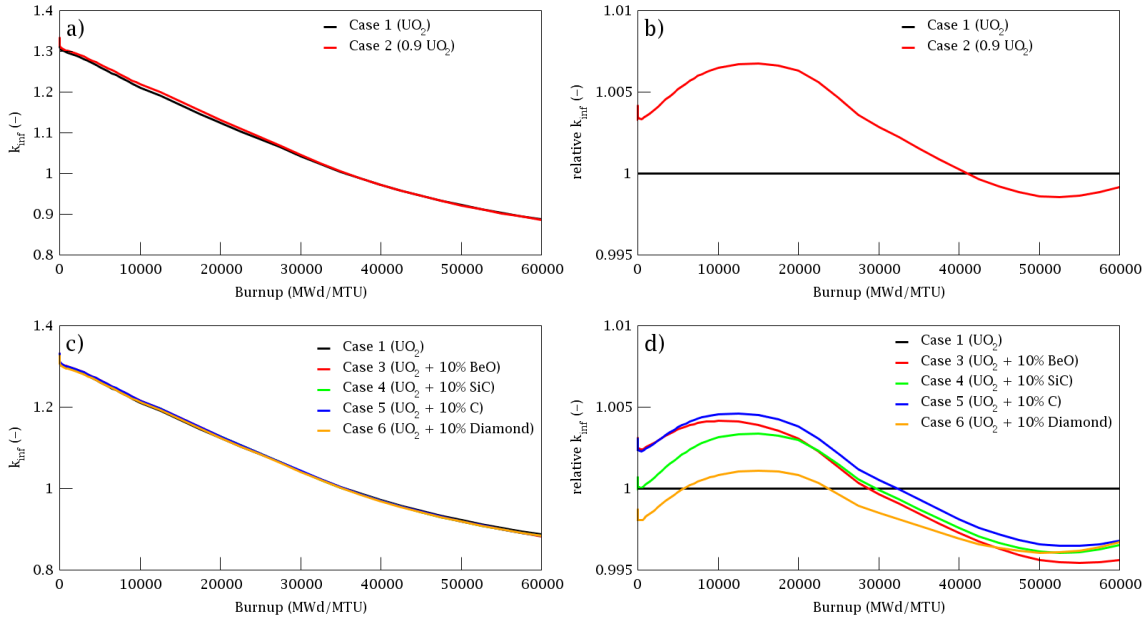

Fig. 3.2: Evolution of k_∞ during burnup calculated for the cases in Table 3.1

In the beginning of life with zero burnup, the reduced fuel volume was found to be the parameter most affecting the neutronic performance [106, 107]. The resonance escape probability is increased due to partial reduction of the influence of ^{238}U resonances in the total macroscopic cross section of the fuel. On the other hand, the fast fission factor is decreased due to less ^{238}U present in the fuel and similarly the thermal utilization factor is slightly decreased as well. A positive effect on k_∞ is accounted to reproduction factor due to less neutron capture in the fuel. The temperature effect was not taken into account in this study but compared to influence of the reduced fuel volume, the effect of reduced fuel temperature and neutron moderation was found very small, at least for the composite fuel with 10 vol.% BeO [106]. But similar results can be expected for the other cases.

The burnup behavior of k_∞ is not investigated in [106] but reference [107] attributes the increased k_∞ of UO_2-SiC fuel to thermal utilization factor: *As the fuel burns up, the K-infinity of UO_2 fuel decreases slower than that of UO_2 with 5 $\%_w$ and 10 $\%_w$ SiC because the thermal utilization factor in UO_2 decreases slower than in UO_2 with SiC.*

The water to fuel ratio may also have an significant impact. The PWR technology is designed to be under-moderated. By removing one tenth of the fuel volume the k_∞ should increase.

For the final burnup stage, Figures 3.2c and 3.2d reveal that there is penalty in k_∞ by all Cases 3-6 compared to Case 1. This is very likely due to the neutron absorption. The composite nuclear fuel UO_2 + 10 vol.% C poses the highest k_∞ evolution because Carbon has very good moderation properties and low absorption and thus this finding is not surprising. On the other hand, the evolution of the other two types of composite fuel being compared is slightly surprising. At the end of life, the k_∞ of composite nuclear fuel UO_2 + 10 vol.% SiC is almost the same as the carbon based one. The influence of Si is almost negligible. Moreover, this type of fuel exceeds the performance of the composite nuclear fuel UO_2 + 10 vol.% BeO.

The reason why the Case 6 (carbon with diamond density) differs from the case 5 was not found. The moderator to fuel ratio may be one of the reasons but this phenomena needs further moder detail research.

The last note in this section is dedicated to the magnitude of the k_∞. The k_∞ of the composite fuels are larger compared to the k_∞ of the standard UO_2 fuel for most of the time. However, it must be mentioned here that this is a specific case related to the model of the VVER-1000 pin used by the UWB code. Analysis performed in [106, 107] where different codes and models were used predicted much stronger and earlier decrease in k_∞ for both cases using SiC and BeO. For this reason, the results obtained here are indicative only. To be completed, Figures 3.3 and 3.4 show the results obtained in the mentioned works, the details are given in captions.

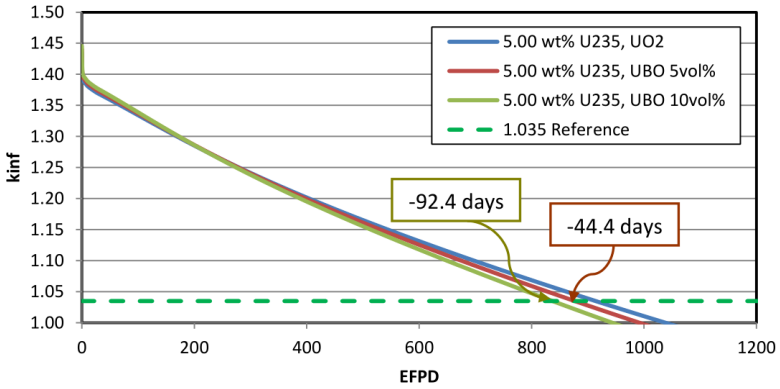

Fig. 3.3: Influence of BeO content on the k_∞. Calculations performed with DRAGON code in 2D infinite square lattice. The fuel pellet has the radius of 4.095 mm, the cladding is of 0.57 mm thickness, the fuel pitch 16.3 mm [106].

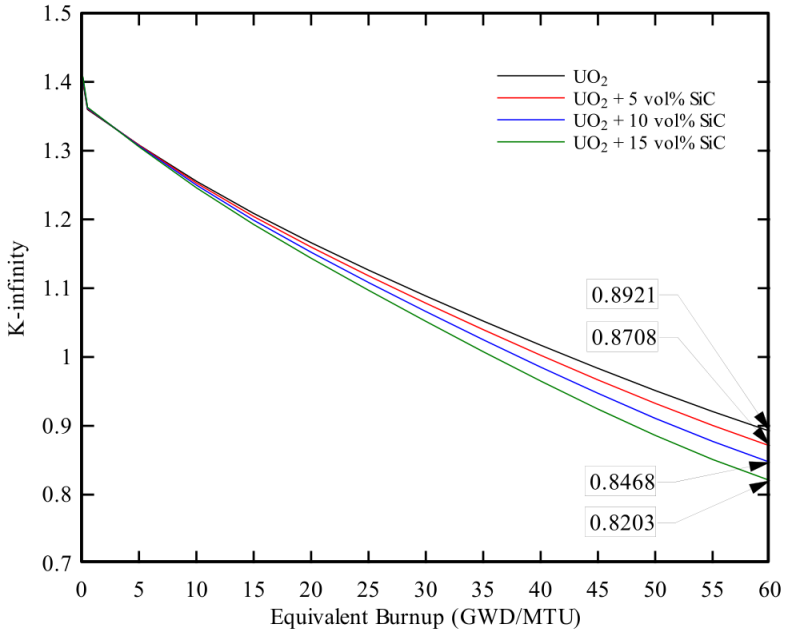

Fig. 3.4: Influence of SiC content on the k_∞. Calculations performed with CASMO-3 code for Framatome Mark-B 15x15 fuel assembly design. Fuel enrichment 4.66% [107].

3.3 Composite fuels comparison

In this wide subchapter, the composite fuel options are compared from the thermal point of view. At the end of this subchapter, one fuel option is selected for detail analysis during normal operation and accidents.

3.3.1 Verificiation of the TCC models

Here, the thermal conductivity models presented in Chapter 2.1 and material properties presented in Chapter 2.2 are combined and compared to experimental values (if available) in order to see their (combined) validity.

Figure 3.5 provides an overview of the composites being investigated in this subchapter. The UO_2 + BeO composite is not investigated in this chapter because the model for determining its thermal conductivity as a function of burnup and temperature is already presented in section 2.4.1.

Figure 3.5a depicts the comparison of the experimental values of thermal conductivity measured at sample containing 5 vol.% SiC with the prediction obtained by using the Hasselman model (eq. 2.30). In this reference, the Hasselman model is presented as a model yielding good predictions regarding the UO_2+SiC composite fuel thermal conductivity up to 20 vol.% SiC. The error bars of measured values were also available in the reference [25] and thus they are shown as well.

The interfacial conductance between UO_2 matrix and SiC grain is one of the input parameters of the Hasselman model. It was determined as a function of temperature using the equation 2.31 and its derivation is presented in section 3.3.2 in detail. For simplicity, the same function was then used for predictions of composite fuel thermal conductivity in all other cases presented in Figure 3.5.

In Figure 3.5b, the predicted thermal conductivity of UO_2 with 5 vol.% diamonds is being compared to experimental results. The starting thermal conductivity of UO_2 is determined for 96.5% TD as indicated in [63]. The prediction of the composite thermal conductivity is subsequently done with Hasselman model as in the previous case. It is clearly visible from this figure, that this model underestimates the composite thermal conductivity. Moreover, if the UO_2 thermal conductivity was corrected to 95 %TD, the Hasselman model results would be almost identical to the prediction for composite with 5 vol.% of SiC.

This is an indication of the Hasselman model limitation. It seems that this model is not suitable for composites having the difference in the thermal conductivity of components bigger than two orders. In the here presented case, the difference in thermal conductivity between matrix and additive is two orders or more depending on temperature. As illustrated in Figure 3.6, for such a high ratio of k_p/k_m, this

constituent becomes dominant among the others in the eq. 2.30 and the model becomes insensitive to difference in thermal conductivity of the additive.

A new model for prediction of the UO_2+diamond fuel thermal conductivity had to be found. The geometric mean model [16] was found to be good in prediction of the thermal conductivity for this specific type of composite. The model is given by the following equation:

$$\lambda_{eff} = \lambda_m^{(1-f)} \cdot \lambda_p^f. \tag{3.6}$$

The results of this model are presented in Figure 3.5b by the blue line. However, there is a problem of the verification of this model for higher SiC contents. Some data on UO_2+ 10 vol.% diamond fuel was published in [63] but significant scatter of the data measured by different laboratories (University of Florida, LANL and INL) was reported here as well. Therefore, it is not possible to verify the model's validity at higher diamond contents, but it is noteworthy to mention that this model yields results which fall within the range of data presented for this diamond concentration.

Figure s 3.5c and 3.5d show the experimental and predicted data on the thermal conductivity of composite fuels comprising from UO_2 and SWCNT and K1100 graphite fibers, respectively. The simplified Miranda model (eq. 2.33) was used to predict the composite thermal conductivity and two cases are assumed in both Figure s: 1) matrix with single additive and 2) matrix with additive covered with protective SiC layer.

As the input data for the Miranda model, SWCNT having a diameter and length of 1.7 nm was assumed. The K1100 fibers are reported to have a diameter 9-10 nm and thus the value of 9 nm was used as the reference. When the protective SiC layer was involved in the prediction, the 10 μm thickness was used, as estimated from [57].

Based on the comparison with measured values in Figure 3.5c, the simplified Miranda model fails to predict the UO_2+5 vol.% SWCNT fuel thermal conductivity. Due to the lower thermal conductivity of SiC, the case with SiC covered SWCNT shows a significant decrease in thermal conductivity compared to the case with single uncovered SWCNT, but the values predicted by Miranda model are still far above the expectations.

Given to the fact that the SiC and K1100 have close values of thermal conductivity, there is a little difference in thermal conductivity between UO_2+K1100 graphite fibers and UO_2+SiC covered K1100 graphite fibers in the Figure 3.5d.

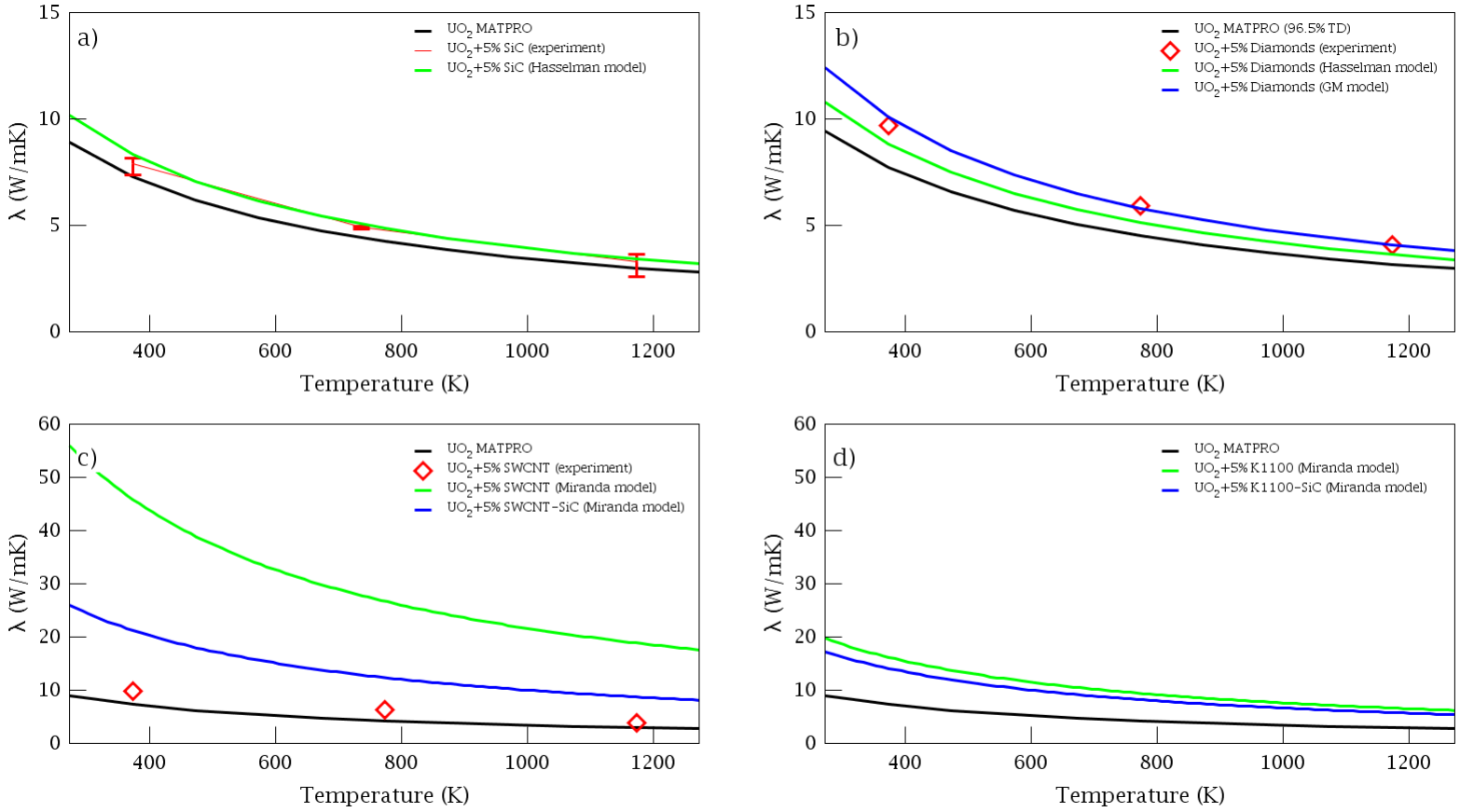

Fig. 3.5: Comparison of the thermal conductivity predictions and measurement of the composite fuel containing 5 vol.% of additives as a) SiC, b) Diamonds, c) SWCNT (with SiC coating), and d) K1100 graphite fiber (with SiC coating).

3.3.2 Interfacial conductance prediction

The interfacial thermal conductance was calculated using the acoustic mismatch model represented by eq. 2.31. here, the longitudinal and shear phonon velocities of SiC, ν_l and ν_t, respectively, were taken from the NIST database [98] and the average phonon velocity ν is then simply determined using the following equation:

$$\frac{3}{\nu^2} = \frac{1}{\nu_l^2} + \frac{2}{\nu_t^2}. \tag{3.7}$$

The phonon velocity of UO_2 was determined for fresh state using the simplified one-dimensional model based on the knowledge of Young modulus E [108] and density ρ [90]:

$$\nu = \sqrt{\frac{E}{\rho}}. \tag{3.8}$$

The resulting dependency of the interfacial conductance is depicted in Figure 3.7 and one can see that it follows the UO_2 heat capacity function which was found in [90] as well.

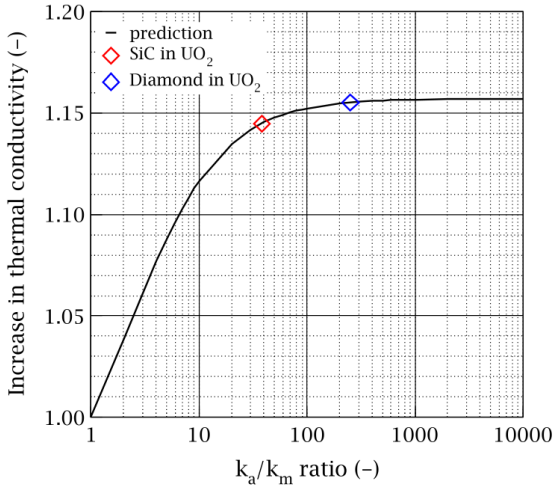

Fig. 3.6: Increament in relative thermal conductivity computed by Hasselman model for UO_2+SiC and UO_2+Diamonds.

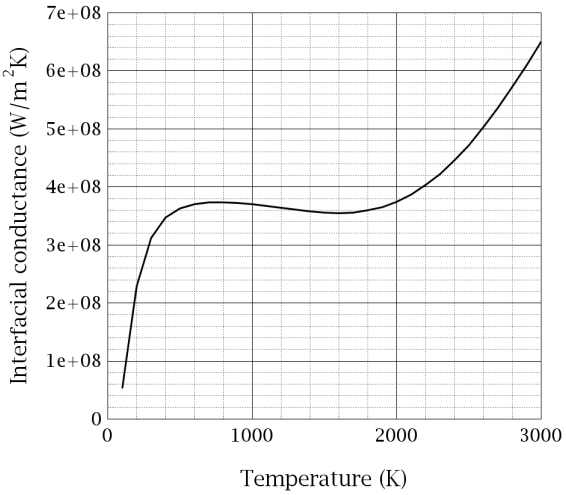

Fig. 3.7: The interfacial conductance h_c between UO_2 matrix and SiC grain as a function of temperature

3.3.3 Prediction of the fuel centerline temperature

The fuel centerline temperature is one of the most important parameters at all. The low thermal conductivity gives rise a steep temperature gradient within the fuel thereby causing high thermal stresses, pellet cracking and increased FGR. Increasing the thermal conductivity allows for increasing the operation limit on $LHGR$ and thus the thermal performance of the fuel pin as well.

The temperature profile within the fuel pellet can be calculated using the famous relationship already given by eq. 1.2.

3.3.4 Maximum LHGR and stored energy

During the operation, the maximum LHGR is limited in the meaning of function of burnup. The limit on that is defined in order to protect the fuel from fuel melting, excessive rod internal pressure (fission gas release), PCMI stress and other [109]. By picking up the first phenomenon - the fuel melting - a new parameter can be used for the additives comparison,

The parameter can be defined as the $LHGR$ which leads to such a high centerline temperature causing the UO_2 to melt. In the here presented case, this definition is changed in order to cover the influence of the second phase (dopant) within the UO_2 matrix. The process being considered is the chemical reaction between the UO_2 and the additive which usually starts at substantially lower temperatures than that of UO_2 melting.

Let us call the new measure "$LHGR$ to Chemical Reaction" (denoted as $LHGR_{CR}$) and let us define it as the $LHGR$ leading to such a temperature within the fuel pellet (expectably at centerline) which leads to chemical reaction between UO_2 and the second phase being encapsulated within the UO_2. Table 3.2 defines the maximal temperature which can occur within the fuel pellet containing candidate materials.

The comparison is based on the Figure 2.11. Here, the averaged relative increase in measured thermal conductivity was used as the correlation factor (CF) to calculate the new thermal conductivity function of each type of composite fuel. The comparison is made for fresh fuel only. The model used for the comparison is one fuel pellet with diameter of 7.6 mm and surface temperature of 400 °C. The pellet height is 10 mm.

Regarding the maximum temperature, beside the information given in subchapter 2.2, the limiting maximum temperature of UO_2+BeO composite was set as equal to its eutectic temperature found in [40] (see Figure 2.6).

The normal operational limit on $LHGR$ is below 400 W/cm but this is applied for the average $LHGR$. The peak $LHGR$ can reach up to 450 W/cm by new types of fuel assemblies. From this point of view, the fuel containing SiC seems as not

Fuel option	CF (-)	T_{max} (°C)	$LHGR_{CR}$ (W/cm)
UO_2	1.00	2840	914
UO_2 + SiC	1.06	1370	454
UO_2 + BeO	1.26	2060	801
UO_2 + SWCNT	1.41	1400	618
UO_2 + Diamond	1.39	1400	608

Tab. 3.2: Comparison of the nuclear fuels based on the maximal allowable LHGR

being safe to operate. Next, the long term behavior of such composite is a still remaining question needed to be answered which implies next safety uncertainties on the operational limits.

Another popular parameter being used for comparison of the accident resistant fuels comprising from UO_2 and additive is the heat energy stored within the fuel. This parameter plays some role during double end guillotine LOCA. The energy stored within the fuel increases the core temperature immediately after the break occurrence [8] (this phenomena is shortly introduced in subchapter 6.1). Table 3.3 displays the Stored Energy (SE) found for the same pellet model loaded with LHGR equal to 300 W/cm. Graphical illustration of the data from Table 3.3 is displayed in Figure 3.3. The SE was estimated using the simple caloric equation:

$$Q = [V_{UO_2} \cdot \rho_{UO_2}(T_{av}) \cdot c_{p,UO_2}(T_{av}) + (V - V_{UO_2}) \cdot \rho_{add}(T_{av}) \cdot c_{p,add}(T_{av})] \cdot (T_{av} - T_{room}). \tag{3.9}$$

In eq. 3.9 and in Table 3.3, the T_{max} represents the centerline temperature and T_{av} stands for the average temperature of the fuel pellet and V is the pellet volume. The T_{room} is set to 20 °C and thus, by occasion, the SE of UO_2 is equal to 100 J approximately. The other values of SE thereby represent the percentage change in SE as well. Moreover, Figure 3.8 contains the data how the SE is distributed between UO_2 and the additive.

In general, the decreased centerline temperature causes the stored energy to decrease. But it is interesting to note that all additives (especially diamonds and BeO) have higher share of SE that pure UO_2. The only exception from this is the composite fuel containing SWCNT. The reason for this is the lower density of SWCNT determined to be 1.984 g·cm^{-3}. It should be noted here, that this value for determined for SWCNT with diameter of 1.5 nm but the density function in Fig. 2 in [96] is very steep and yields strongly different results for small change in radius around this specific value of diameter.

Fuel option	T_{max} (°C)	T_{av} (°C)	SE (J)
UO_2	1035	718	99.97
UO_2 + SiC	988	694	97.37
UO_2 + BeO	872	636	91.55
UO_2 + SWCNT	812	606	83.91
UO_2 + Diamond	820	610	87.82

Tab. 3.3: Calculated values of maximum and average temperatures within the fuel pellet model and corresponding energy stored within the fuel pellet.

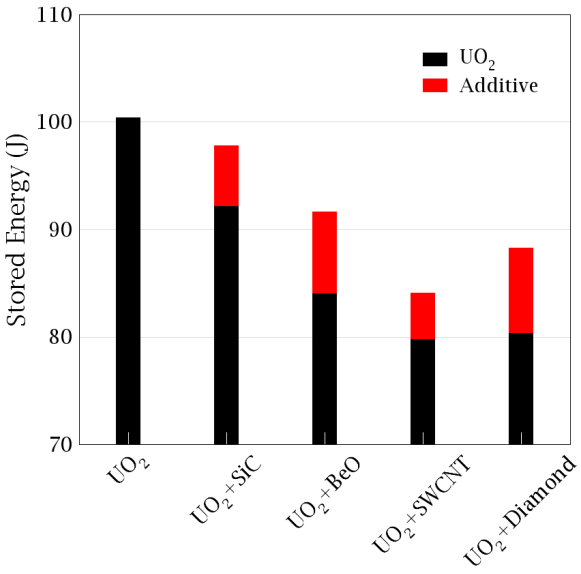

Fig. 3.8: Graphical illustration of the stored energy in Table 3.3 with presentation of the share of UO_2 and additives on the stored energy.

3.4 Selection of the candidate material

Based on the information given in the previous chapters and sections, this subchapter selects one candidate for composite fuel detail analysis.

The first option to be excluded is the UO_2 + SWCNT composite fuel. The reason is very simple - the thermal conductivity behavior of this composite fuel is poorly understood and no reasonable behavior estimate can be done. Moreover, the Miranda model is not suitable for predicting the thermal conductivity of UO_2 + SWCNT mixture and no other suitable model was found.

The second option to be excluded is the UO_2 + diamonds composite fuel. Even though it provides the best thermal conductivity enhancement, the behavior of such a fuel, similarly as in the case of UO_2 + SWCNT, is poorly understood. But author of this thesis wants to express another supportive opinion why to exclude this concept despite its promising properties: the risk that the fuel temperature exceeds the 1400 °C limit when the graphitization occurs is too large especially during the RIA accident when sudden temperature is generated within the fuel. One needs to figure out what will be the impact of the sudden increase in the diamond volume on the composite fuel behavior.

The two remaining options are the UO_2 + BeO and UO_2 + SiC composite fuels. A glance at the results in section 3.3.4 imply that the UO_2 + BeO provides much better operational limits compared to UO_2 + SiC composite fuel. Even its experimentally determined dependence of thermal conductivity on irradiation is known. Unfortunately, during the decision making this data was not available and author of this work has decided to focus on the UO_2 + SiC composite fuel. The main reason why the UO_2 + BeO composite fuel was not investigated is its toxicity. Author of this work finds this type of composite fuel with no perspective for commercial use due to the political, economical and public acceptance when used.

For this reason and despite the fact, that UO_2 + SiC composite provides the worst improvements, the UO_2 + SiC concept is selected for further detail analysis.

4 Software used for modelling

In this chapter, the main codes which were used for modelling of the composite fuel option(s) are briefly presented.

4.1 FEMAXI

There are many computer codes which can be used to investigate/predict the fuel performance during normal conditions, like for example BISON, FEMAXI, FRAPCON, TRANSURANUS. For the purpose of this work, the FEMAXI6 code has been selected since this code, together with its source code, is easily available from the NEA database. The modification of this code, in order to be able to cope with additives like SiC, is not difficult.

The code consists of two main modules - Thermal and Mechanical, as depicted in Figure 4.1. The first module calculates the characteristics related to temperature (temperature distribution, FGR, thermally induced deformation for example) whereas the second module calculates the characteristics related to mechanical behavior [110]. After successful convergence of the results from these two modules, local PCMI analysis is performed. The method of solution is a one-dimensional axis-symmetrical finite element method. The code is constructed to solve the whole fuel pin problems including the pellet–coolant heat transfer phenomena. Beside this, a detail one–pellet analysis is also possible. The possibility of coupling the code with RODBURN and PLUTON is inherently included in order to obtain basic neutronic input parameters [111].

Another advantage of use of the code is the amount of parameters which can be calculated using this code. Beside this, there is a relatively large selection of materials models offered for computation.

In contrast to normal use of this code, this work aims to use the FEMAXI6 code in application the UO_2-additive fuel. A similar study has been done in [102] where the CAMPUS code has been utilized to predict the behavior of UO_2 fuel pellet containing different fractions of SiC. Since this study presents a good starting point for subchapter 5.3, where the modified FEMAXI6 code will be used to analyze the behavior of modified fuel under accidental condition, the study done in [102] is partially reproduced here.

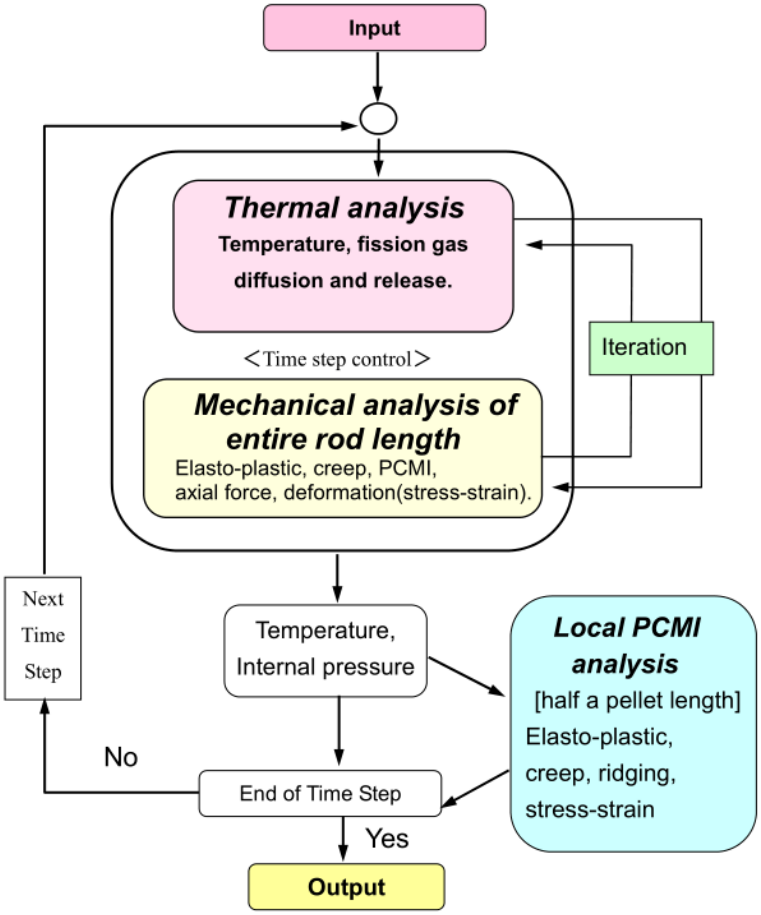

Fig. 4.1: Overview of the FEMAXI-6 structure [111]

4.2 RELAP5

The RELAP5 is briefly introduced here. Based on the information given in the abstract of the RELAP5 manual [112]: *The RELAP5 code has been developed for best-estimate transient simulation of light water reactor coolant systems during postulated accidents. The code models the coupled behavior of the reactor coolant system and the core for loss-of-coolant accidents and operational transients such as anticipated transient without scram, loss of offsite power, loss of feedwater, and loss of flow.*

The code itself is based on a nonhomogeneous and nonequilibrium model for the two-phase system. This system is solved by a semi-implicit numerical scheme. Many models of power plant components, like for example pumps, valves, turbines, heat exchanging structures, separators, accumulators, are involved within the code. The code contains a library of system control components (PID regulators, for example) and the reactor point kinetics is available as well. For the accident simulations, the special models of choked flow or flow at abrupt area change are incorporated.

Originally, the code was developed for the U.S. Nuclear Regulatory Commission (NRC) but later some other organizations have joined the developer team within the frame of the Code Applications and Maintenance Program (CAMP). The code is not under development anymore, only the maintenance is provided but the code is still widely used *to support rulemaking, licensing audit calculations, evaluation of accident mitigation strategies, evaluation of operator guidelines, and experiment planning analysis.*

Instead of RELAP5, it was decided to develop a new code TRACE which will be able to simulate neutronic and thermal-hydraulic processes of an reactor at the same time.

4.3 UWB

The UWB code is a one purpose code written with the intention to have a fast depletion code for simple infinite lattice analysis. The code allows for calculation of burnup depletion within a 2D square, triangular or sphere lattice based on the Monte Carlo simulation approach. The code was written by Martin Lovecky at the University of West Bohemia. For examples of use see [113, 114] for example.

The code's approach to solve the burnup task consists of five steps: initial stage, prediction stage, correction stage, depletion stage, and estimation stage. During the initial stage, the total macroscopic cross section are prepared and the transport solver then calculates the neutron flux in all defined regions together with multiplication factor. The prediction stage estimates the fuel state at the end of the burnup based on the initial state variables. The corrector stage is almost identical to the predictor stage but the predicted effective cross sections are taken as the input data. The output of this stage is then the averaged predicted and corrected values of effective cross sections, relative region powers, estimations of multiplication coefficient, and transport multiplication values. The fuel composition and multiplication coefficient during burnup are calculated during the depletion stage. The final estimation stage is used for comparing the initial and final multiplication coefficients which are calculated by transport solver using the multiplication coefficient estimates. The output is then the estimated multiplication coefficients which are corrected for the expected differences.

The nuclear data library ENDF/B-VII.1 is used as the main source of nuclear data and no other option of nuclear data library is possible within the UWB code.

4.4 TRANSURANUS

The TRANSURANUS code is one of the codes used for predictions of detail fuel behaviour during various scenarios under normal, off-normal and accident conditions. The code was developed in 1976 and it was extended and validated to calculate problems related to VVER technology in 1995. It has a materials data bank for many nuclear reactor technology materials: oxide, mixed oxide, carbide, and nitride fuels, Zircaloy and steel claddings, and different coolants. Implementation of the new models of material properties should be easy too [115, 116, 117, 118].

Thus, the code itself can be used to asset the behaviour of modified composite nuclear fuel. But in this work, the code is used for analysis of the composite fuel during the RIA accident solely.

5 Performance of the composite fuel during normal operation

The fuel performance during normal operation will be investigated because it is one of the most essential knowledge here. Another good reason for this is that some of these parameters have a strong influence on the consequences of accidents are dependent on the conditions under which the reactor (fuel assembly) has been operated. One of these parameters is, for example, the internal gas pressure within the fuel pins which is one of the major causes of the ballooning effect.

The fuel pins are filled with helium in order to improve the heat transfer conditions between pellets and cladding. As the consequence of the Fission Gas Release (FGR) into the plenum, the composition of the fuel pin free volume gas changes by contamination of Ar, Xe, Kr and other gases. The magnitude of FGR strongly affects not only the gas composition, but the plenum pressure within the fuel pin as well.

The state equation shows that the final plenum pressure of fuel pin being subjected to LOCA is conditioned by the initial plenum pressure. Thus, mitigating the FGR from the fuel pellet is a one of the possible ways how the ballooning effect can be diminished. Basically, the simples method how the FGR can be reduced is to decrease the temperature of the fuel pellet because the FGR which is strongly dependent on temperature. Needless to say, addition of SiC currently causes the flattening of the temperature profile within the fuel and thus leading to mitigation of the FGR. Summarized, SiC addition into the fuel should lead to positive side-effect of mitigation of the risk of ballooning during BDBA, for example.

For prediction the behavior of composite fuel, the FEMAXI6 code is used. Using the reference [102] as the base case, verification of the code is done by simulation of one fuel pellet during steady power burnup in subchapter 5.1. This is followed by subchapter 5.2 where the pellet behavior during burnup is explained in detail. In subchapter 5.3, a sensitivity study is done where the influence of SiC content on the fuel performance parameters is investigated. Beside this, in subchapter 6.7, the modified code is used to asset the performance of the modified fuel during accident which was derived from the LOCA type accident.

5.1 Verification of the FEMAXI6 code

According to general practice and reccomendations, [119, 120] e.g., each program should be verified before its use in any TH calculations. There has been numerous studies published using different versions of the FEMAXI6code for calculation of wide spectra of phenomena related to nuclear fuel performance. The FEMAXI6code is often used for analysis of experiments done in research reactors [121, 122, 123, 124]. The verification against Halden data for MOX fuel has been also done with good results [125]. Although the models incorporated in the FEMAXI6code versions are primarily intended for the use with BWRs and western PWRs (with regards to the cladding models), the utilization for the analysis in the field of the WWER technology has been also reported in some literature [126, 127, 128].

For the verification of the FEMAXI6 code, the study [102] is utilized where in turn the CAMPUS code has been verified for the use in the UO_2-SiC application. Specifically, this reference deals with simulation of one fuel pellet exposed at constant LHGR of 200 W/cm with the operation period of 3.8 years in a typical LWR reactor. The parameters being observed were the pellet centerline and surface temperatures, cladding surface temperature, gap width, FGR, and plenum pressure. As it was confirmed that the CAMPUS code yields reliable results by comparison of the results with results predicted by other codes, a sensitivity study has been performed which investigated the influence of SiC content on the previously mentioned and some other parameters.

Figure 5.1 shows the fuel pin and the one fuel pellet model representing the base case characteristics in [102], Table 5.1 lists additional input data.

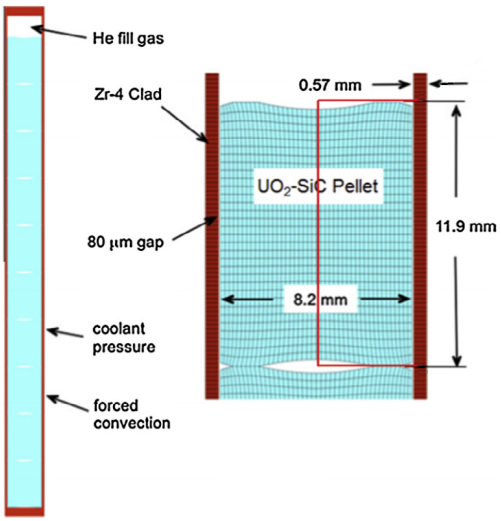

Fig. 5.1: Fuel pin and fuel pellet model used for verification of the CAMPUS model [102]

Parameter	**Value**
Plenum to fuel ratio	0.045
Irradiation time (years)	3.8
Fast neutron flux (n/m^{2}s)	9.5E17
Coolant pressure (MPa)	15.5
Coolant temperature (K)	530
Coolant convection coefficient (W/m^{2}K)	7500
Rod fill gas	Helium
Fill gas initial pressure (MPa)	2.0
Initial fuel density	95% theoretical

Tab. 5.1: Additional data of the base case used for verification of the CAMPUS code in [102]

In order to get reasonably comparable results, there was an effort exerted to reconstruct the base case analysis using FEMAXI6 as accurately as possible. Models used in [102] were identified and, if possible, also used in the FEMAXI6 reconstructed one pellet model. (The exceptions from this are specified within the following text.

During the reconstruction, there was a general problem that the FEMAXI6 code offers a relatively large variety of established models and data [129] which needed to be set while many of them are not used in [102]. A typical example is the Pellet crack and relocation option. In turn, in some models which are implemented both in CAMPUS and FEMAXI6 as well, it was not possible to adjust all parameters listed in [102]. One of these cases is the cladding thermal expansion model which considers the radial, axial and angular thermal expansion coefficients. So, the CAMPUS model accounts for all three coefficients whereas the FEMAXI6 offers the option to alter the two first only. Moreover, to the author's knowledge, there is a very little number of references recommending specific models or their combinations for FEMAXI6 in this kind of burnup applications. Consequently, there was on guidance how the remaining parameters should be adjusted. For this reason, the parameters in the FEMAXI6 input deck which were not identified in [102] were left in the default mode.

As a side note, it should be noted here that a different way was used to determine the cladding surface temperature in the present work. In the FEMAXI6 version, it is not possible to specify the exact value of heat transfer coefficient which is listed in Table 5.1. Instead of that, the option of direct cladding surface temperature specification in the input deck has been used. Based on data in Table 5.1, the cladding surface temperature has been determined as 619 K.

Figure 5.2 shows the results of the base case analysis as predicted by the FEMAXI6 code. Results of some other codes of the same calculation are presented as well. Figure 5.2a describes the evolution of temperatures at fuel centerline, fuel outer surface and cladding inner surface. The temperatures predicted by FEMAXI6 are observed to be lower than those predicted by other codes in the beginning of the simulation. This is caused by larger gap resulting from different fuel densification model (see Figure 5.2c). It was found that the US NRC fuel densification model [130] code predicts the evolution of the gap size in a sufficiently good agreement with other codes but it should be noted here that all fuel densification models included in FEMAXI6 predicted larger fuel gap than the other codes. Even though the magnitude of the gap width predicted by FEMAXI6 is larger compared to predictions of other codes, the trend of gap width and of the gap closure agrees very well with CAMPUS and BISON predictions.

The evolution of FGR was found to be similar to that of FRAPCON. This is because the default condition of minimal FGR rate equal to 0.5% was used in the FEMAXI6 model. On the other hand, the evolution of plenum pressure is different from the FRAPCON prediction in Figure 5.2d.

One can even see a small decrease in plenum pressure starting around 25 MWd/kgU. This is caused by cladding inner diameter increase as the cladding accommodates to expanding pellet leading to an increase in the plenum volume. But at this burnup, the FGR starts as well and compensates for the plenum volume increase. The FGR is of bigger influence and gives rise to further increase in plenum pressure. The same behavior is also partially visible by the ABAQUS prediction.

An interesting fact is that although the same White & Tucker FGR model is used by CAMPUS and FEMAXI6, the FGR is substantially lower by FEMAXI6 prediction. The explanation of this discrepancy lies within the White & Tucker model parameters and in the model form itself, because slightly different forms are applied in both codes. The CAMPUS code uses the semi-dihedral angle between two surfaces equal to 0.5 whereas the FEMAXI6 code (as reported in the FEMAXI6 manual [111]) uses the default value equal to 0.25. When the CAMPUS's value is used in the FEMAXI6 code, the code yields non-realistic results and for this reason the initial value is retained. The White & Tucker FGR model applied in the CAMPUS code also accounts for influence of the grain radius whereas that used in FEMAXI6 code not. To be completed, the lower FGR predicted by FEMAXI6 is also caused by predicted lower fuel temperatures.

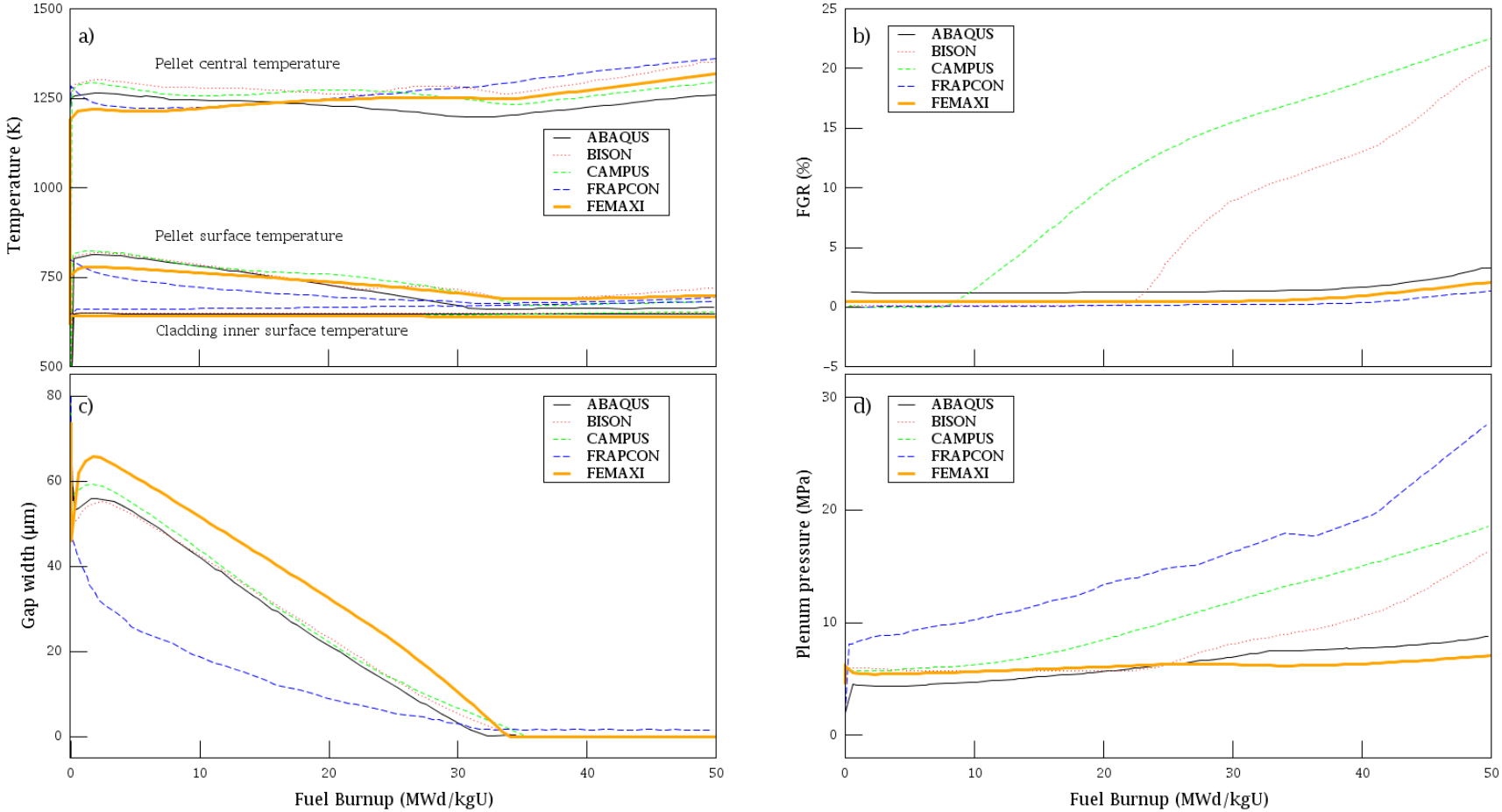

Fig. 5.2: Comparison of FEMAXI6 base case calculation with results presented in [102]

5.2 Fuel pellet behavior

This subchapter provides the information how the one pellet simulated by FEMAXI6 behaves during burnup. For this, the Figure 5.3 included in the next subchapter 5.3 focusing on SiC sensitivity study is utilized. In this figure, the data on standard UO_2 are used for explanation of the fuel behavior. The subchapter 5.3 then follows the information given in this subchapter.

Figures 5.3a and 5.3d show the temperatures at pellet centerline and at pellet surface, respectively. The pellet central temperature is a complex phenomenon influenced by many other parameters, like e.g. pellet density, pellet thermal conductivity, pellet surface temperature, pellet power density. First, the pellet central temperature increases due to the fuel densification (increasing fuel-clad gap) and to the decrease in gap conductance. After that, a small decrease is visible in Figure 5.3a due to the increasing gap conductance. However, the decrease in pellet central temperature is followed by a next increase due to the rapid degradation in fuel thermal conductivity. The thermal conductivity degradation proceeds during the whole process of burnup, but the degradation is the most severe between 0 and 30 MWd/kgU (see Figure 1.3). At 25 MWd/kg, the centerline temperature starts to decline again because the decreasing trend in pellet surface temperature is somewhat increased after 20 MWd/kgU thereby affecting the pellet central temperature in such a way that the effect of cooler surface prevails over the thermal conductivity degradation. At the burnup of 35 MWd/kgU, the gap is fully closed and the decreasing gap conductance increases the pellet central temperature again.

The relationship between the fuel temperature, gap width, and gap conductance is explained as follows. As mentioned before, the pellet central temperature rapidly increases in the beginning as the reactor power level reaches the nominal value but the increase is also partially supported by the rapid fuel densification. This process gradually increases the gap width and thus reduces the gap conductance. However, the swelling component of the pellet radial change dominates with increasing burnup, the gap width is reduced and the gap conductance is being enhanced. Around 35 MWd/kgU, the gap closes and the cladding resistance (together with increased radial pellet creep) suppresses the radial growth of the pellet.

As it was found in [102], the gap conductance is dominated by a gas conductance part of the Ross & Stoute model. A sensitivity study focused on the influence of FGR on gap conductance has been conducted here and it has confirmed that this conclusion is also valid in the case of FEMAXI6 calculation. The root was found in the gas conductance component of the Ross & Stoute gap conductance model. After the gap closure, the gas conductance component still plays the major role in the heat transfer. This component is in direct proportion to the thermal

conductivity of the gas mixture. The thermal conductivity of the gas mixture is reduced by the presence of Xe and Kr which are introduced to the plenum volume by FGR mechanism.

It should be mentioned here, that the effect of bonding process on the gap conductance is not taken into account using the Ross & Stoute model with option [IGAPCN=2] (despite the fact that some models considering the bonding process influence are available in the FEMAXI6 code). The influence of bonding phenomena on the gap conductance was omitted because the effect of SiC presence on the bonding layer is unclear and the physical phenomena modelled are limited to its minimum.

The plenum pressure follows the development of the fuel gap in the beginning of the calculation. This is reasoned by the fact that the volume between fuel and cladding is a part of the plenum volume which accommodates the filling gas. The sharp decrease in plenum pressure at 25 MWd/kgU is caused by cladding radial creep which starts to play a significant role at this moment by increasing the plenum volume.

5.3 SiC sensitivity study

As mentioned earlier, results of the sensitivity study are presented in Figure 5.3. The behavior of the composite fuel is in agreement with expectations. The increasing SiC content leads to decrease in fuel centerline temperature. In the case of 20% SiC content, the centerline temperature was lowered about 100 K in the beginning of the burnup and about 190 K at 50 MWd/kgU compared to the UO_2 fuel.

The pellet surface temperature does not show such a strong dependence on the SiC addition. With increasing SiC fraction, the fuel gap increases. The main factor playing a role in the fuel gap increase is the lower thermal expansion coefficient of SiC compared to that of UO_2 as reported in [131]. Next, the behavior of the pellet surface temperature after gap closure differs from the predictions presented in [102]. In the present work, the individual cases have different trends while reference [102] finds the gap conductance to decrease after gap closure in all cases.

Among other parameters, the fuel temperature strongly affects the FGR behavior of the fuel. Especially in the case of pure UO_2 fuel, the amount of released Xe and Kr is significant and the gap conductance is reduced. As a consequence, the pellet surface temperature is higher compared to other cases. On the other hand, the 2% FGR predicted for the UO_2 fuel is quite small and consequently the addition of SiC effectively reduces the FGR to lower or null values.

The FGR behavior of the UO_2+SiC fuel is worth discussing in more detail. Reference [46] reports formation of non-perfect contact at the UO_2 matrix-SiC grain boundary during the fuel pellet sintering. The imperfections take form of small voids at the interface and this problem was significant especially in the case of SiC whiskers. Moreover, another significant debonding process during long term high temperature tests has been reported in [132]. This gives a rise to discussion of the next development of the fuel structure.

Basically, there are two options what the development process will be like in the reality. The first option is that the free volume of the voids will accommodate the fission gas and thus it will help to retain the fission gas within the fuel. The second option is that, due to the mechanical stress, for example, the voids interconnect and transform the matrix into the open porosity structure. This would lead to increase in FGR and thus to negative influence on the fuel performance during operation and especially during the accidents. Besides this, there is a significant influence of the doping (or second phase addition) on the gas migration within the fuel. The problem is that there is a significant lack of experimental data which limits the possibility of investigation of this process.

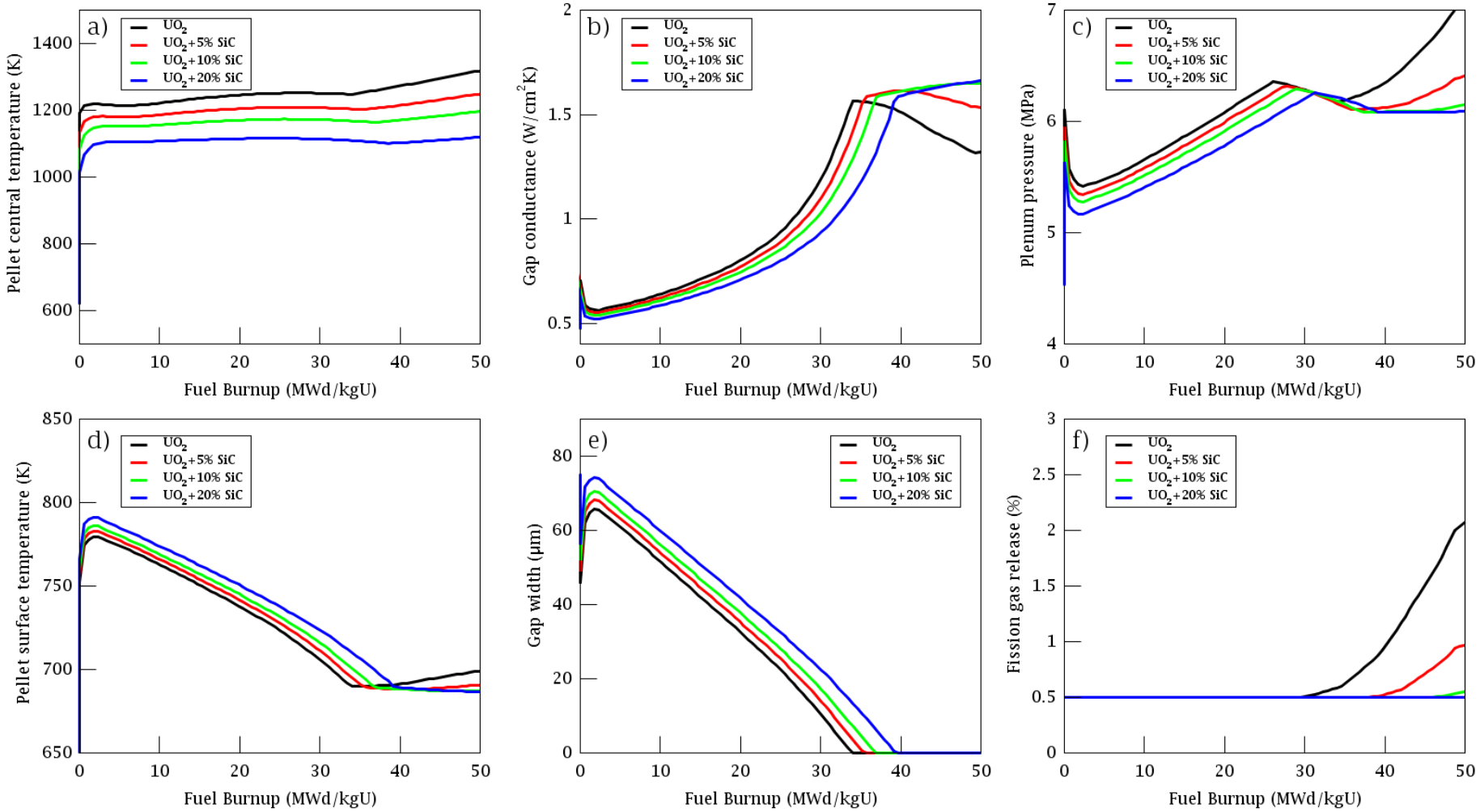

Fig. 5.3: Results of the sensitivity study investigating the influence of SiC on the fuel basic parameters during burnup

The only reference which was found to be related to this topic and which deals with high additive fractions [133] mentions that the Xe diffusion coefficient from UO_2 containing 10-30 mol% was about 20-50 times larger than from pure UO_2. On the other, nuclear fuel containing only 3% of BeO which was tested in the Halden reactor shows a substantial decrease in FGR [44].

Finally, a conclusion can be drawn that the predictions of UO_2+SiC fuel behavior obtained by FEMAXI6 are consistent with those obtained by CAMPUS. The main discrepancies are to be found in FGR and plenum pressure. The different evolution in fuel centerline temperature, which has originally decreasing trend CAMPUS prediction, is probably due to the lower fuel pellet surface temperature.

5.4 Additional parameters of interest

This subchapter provides some additional information on the UO_2 + SiC fuel burnup characteristics which were not mentioned in [102]. First, Figure 5.4 displays the time dependence of the burnup of the fuel with different fractions of SiC. With increasing SiC content, the burnup of the fuel increases too because the lower fraction of UO_2 needs to be more depleted. The fuel with 20 vol. % fraction of SiC has approx. 10 % higher burnup compared to standard UO_2 fuel at the end of the burnup process (1314 days). This is partially explained by considering the fuel porosity but the main reason is the way how the FEMAXI6 calculates the burnup. The subroutine *BURNUP* calculates the burnup based on the pellet weight. In the modified FEMAXI6 code, this parameter was corrected to the SiC content but no modification to the decreased content of fissile material was made. So, the burnup calculation is slightly corrupted. A related point to consider is that the higher burnup of the UO_2 + SiC fuel implies that the UO_2 fraction degrades to higher extend with all the negative high burnup side effects like the rim structure formation etc.

Another parameter of additional interest is a fuel column elongation and a change pellet diameter. Sub-figures within the Figure 5.5 refer about the change of these parameters over the time. FEMAXI6 allows to calculate the radial change and axial elongation according to the usual theory, where the total strain ϵ^{tot} is decomposed into several components as follows:

$$\epsilon^{tot} = \epsilon^{el} + \epsilon^{therm} + \epsilon^{reloc} + \epsilon^{crack} + \epsilon^{densf} + \epsilon^{swell} + \epsilon^{hot-press} + \epsilon^{ps} + \epsilon^{creep}, \quad (5.1)$$

where the strains components refer to elastic strain ϵ^{el}, pellet thermal expansion strain ϵ^{therm}, pellet relocation strain ϵ^{reloc}, pellet crack strain ϵ^{crack}, pellet densification strain ϵ^{densf}, pellet swelling strain ϵ^{swell}, pellet hot-press strain $\epsilon^{hot-press}$, pellet plastic strain ϵ^{ps}, and pellet creep strain ϵ^{creep}.

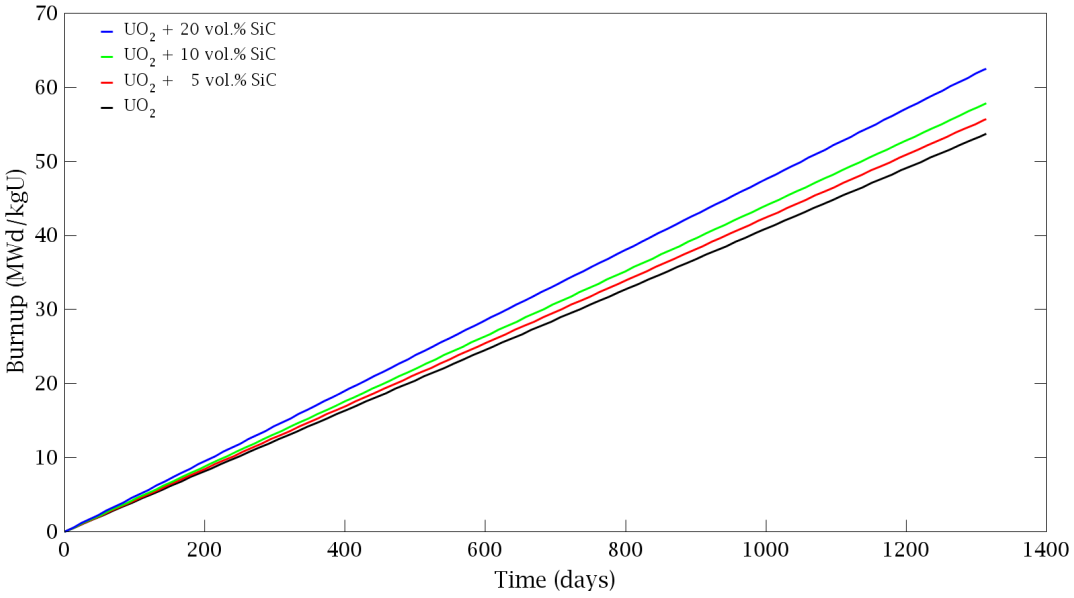

Fig. 5.4: The difference in final burnup at the same final time for different SiC fractions

FEMAXI6 allows to plot the data on some of the components and so, these parameter were calculated and plotted in Figure 5.5 for both, UO_2 and UO_2+10 vol.% SiC fuel. Figures 5.5a and 5.5d refer to UO_2 fuel and Figures 5.5b and 5.5e refer to UO_2+10 vol.% SiC fuel. Figures 5.5c and 5.5f provide the comparison of final state parameters.

Results presented in this figure reflect well the changes made in the modified FEMAXI6 code. Surprisingly, both the final pellet radial displacement and final fuel column elongation reach similar values. The difference lays in the share of the individual components. With respect to reference [102], mainly the thermal expansion model was corrected to the SiC content. For this reason, the final value of the thermal expansion component is different. This difference is, however, compensated by the swelling component, which was not modified within the FEMAXI6 code, and the increased burnup of the modified fuel results in higher swelling component. This indicates, that the modified fuel will have taller fuel column in the zero-power state but the thermal expansion of the regular UO_2 will be more significant during accidents with increased fuel temperature.

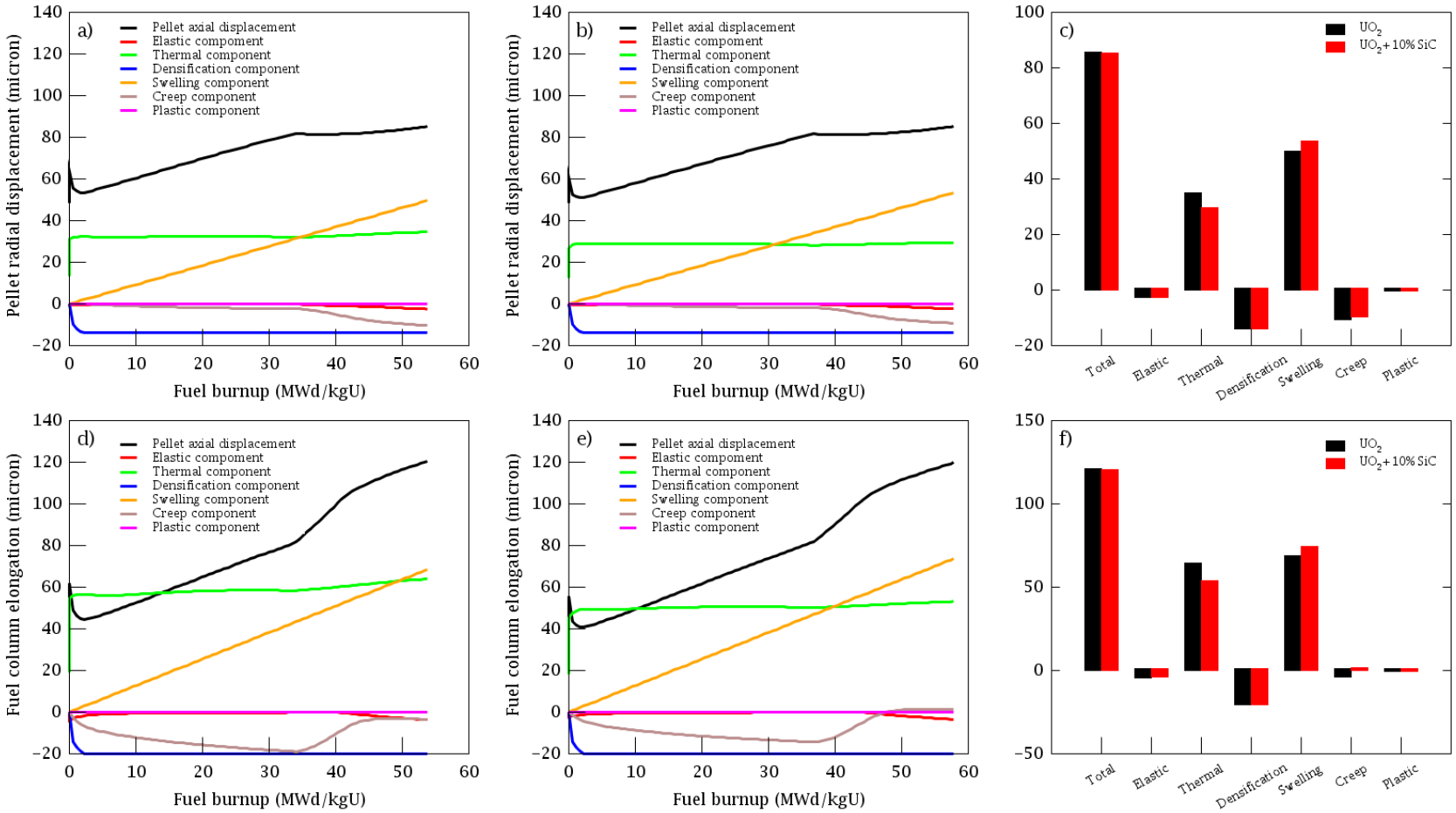

Fig. 5.5: Detail mechanical analysis of the standard UO_2 and UO_2 + 10 vol.% SiC fuel

6 Influence of the composite fuel on LOCA type accident management

6.1 The methodology

In this chapter, the influence of the additive in fuel on the accident management is asset. For this purpose, a method applied in [117] is adopted here. This method originally consists of multi-stage approach. In the first stage, the steady state neutronic analysis of WWER-1000 core with TVSA assemblies is performed. It results in identifying the most loaded fuel pin and its linear heat rate distribution along pin height. The second stage consists of two sub-steps. First, a LOCA analysis is performed for six sets of boundary conditions using RELAP5/MOD3.3 thermal-hydraulic code. Second, modified TRANSURANUS code (v1m1j09 version) is used to read the RELAP5/MOD3.3 results and a more detail analysis was done using this code. It is convenient to say that there was no coupling done between the two codes. Basically, the TRANSURANUS calculated just the response of the fuel based on the input data gained by RELAP5/MOD3.3 for the whole core. But one must also say the TRANSURANUS had to be modified before using in the study [134] because the cladding models in the original version had to be extended to accidental conditions.

This method was adopted in this work, but two changes had to be done. The first change is that, the FEMAXI-6 is used instead of the TRANSURANUS, for the sake of more detailed mechanical analysis. This code, however, is not intended for calculations of accidental conditions. This is probably for the same reason as in the case of TRANSURANUS - the cladding models implemented in the FEMAXI-6 code are suitable only for the steady state and transient analysis. Next, apart from surface cladding temperatures, the core pressure cannot be specified in the input deck and thus cladding stress and strain caused by pressure difference cannot be computed with validity. But because this work deals only with the fuel and the cladding is out of the interest, the FEMAXI-6 is used to calculate the fuel response to the accidental conditions in the reactor core.

The second change consists in the reactor model used. Instead of the full reactor model, the model of the PSB-VVER 1000 experimental facility was used in this work. This facility was built at the Electrogorsk Research and Engineering Centre in Russia and served for thermal-hydraulic tests of VVER-1000 technology accidents, including LOCA type accidents. The advantage of this approach is that there are experimental data available on LOCA test which were used for validation of the model. The model is open to public in [135].

The core of this facility consists of stainless-steel rods being heated by electrical wires (they simulate the VVER-1000 fuel assembly). In the model, this part was modified, and the structure of the fuel rods was changed into standard fuel pins according to geometry of VVER-1000 TVSA-T [136] fuel assembly. With this modified model, the influence of fuel modification on the accident management has been asset.

The nature of the accident being investigated in this work should be discussed here as well. In [117], the accident scenarios investigated were of the classical LOCA type under conditions considering different F type and different burnup stage. The clad surface temperatures did not reach the 1200 °C limit defined for BDBA but they were close to it. Figure 6.1 represents the fuel and cladding temperatures together with its time scale which were simulated in this reference.

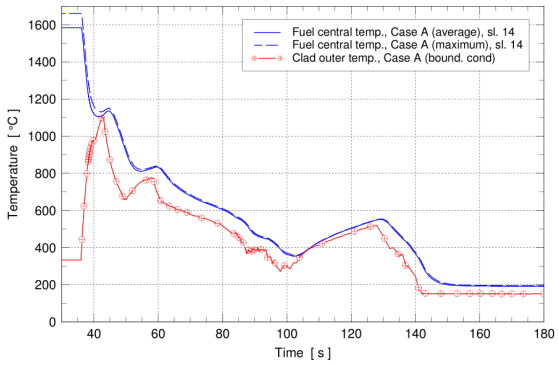

Fig. 6.1: Temperature scenario of the LOCA accident simulated in [117]

In this work, the scenario of the LOCA experiment presented in [135] does not correspond to that simulated in [117]. In this reference, the fast blow out phase is accompanied with depressurization, but this phase is followed by a slow heat up transient leading to BDBA temperatures above 1200 °C. In other words, the typical quenching part of the LOCA accident is missing in this reference. Instead, a series of small ECCS water injection pulses was observed in this experiment which led to partial cooling only and which was distributed over much longer time scale. substantial part of this work is dedicated to analysis of this accident and the reader will be provided by sufficient amount of information within the subchapter 6.2. Based on this experiment, the accident scenario is then created in subchapter 6.3.

So, in general, the accident postulated in this work is not of typical LOCA. It should be rather considered as an accident scenario leading to BDBA accidental conditions.

6.2 The PSB facility

In the following subchapter, the PSB model and its validation will be presented first. After that, the modification of the model to nuclear facility is described. Using the modified model, the influence of the fuel modification on the accident management is investigated.

The PSB-VVER 1000 experimental facility was designed for thermal hydraulic LOCA tests related to the VVER-1000 reactors. Its core consists of one VVER-1000 electrically heated fuel assembly and thus all other parts of the facility are made in approximately 1/300 scale in volume and power (the height scale is kept 1:1). The stainless steel heating rods are heated by electrical current using nichrome wire encapsulated within MgO insolation. In order to give a basic overview of this experimental stand, the scheme of the PSB facility showing thef core and auxiliary systems is depicted in Figure 6.2. The main parts of the PSB facility (core and loops) are depicted in Figure 6.3 in more detail.

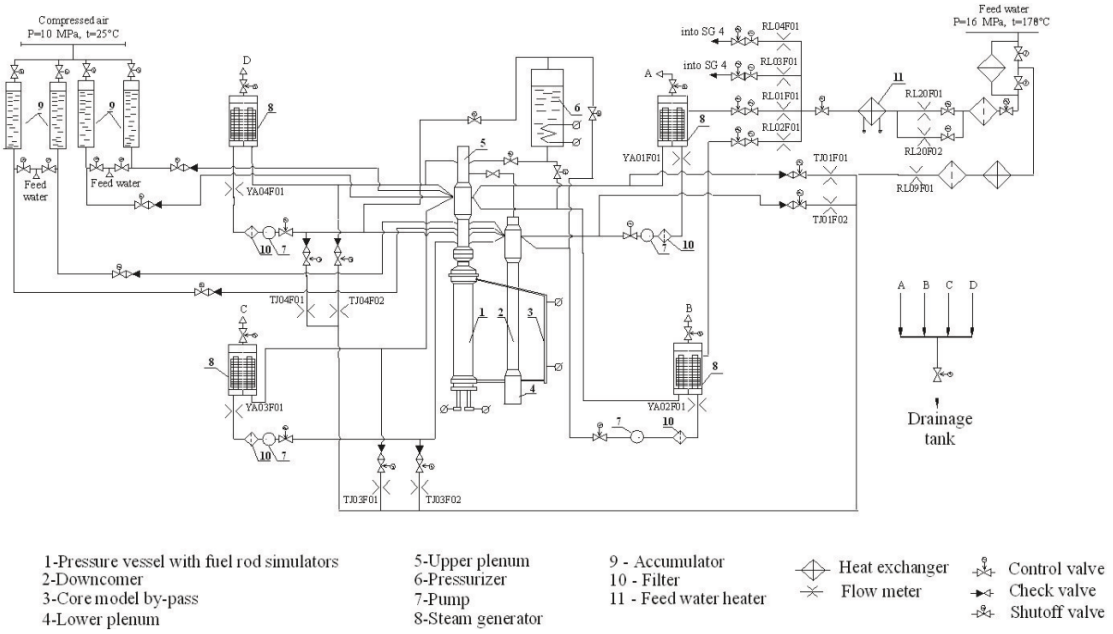

Fig. 6.2: General scheme of the PSB facility [137]

The facility has four loops (each with main coolant pump and steam generator) and the pressurizer can be connected to two of them. The downcomer and core bypass are installed using separate systems out of the core. The safety systems of the facility consist of high-pressure injection system and low-pressure injection system. During thermal hydraulic experiments, the temperatures are measured with thermocouples located at fuel pins and at various positions in the facility. The water level within the facility is measured using pressure sensors. See references [135, 137] for more details on the PSB facility.

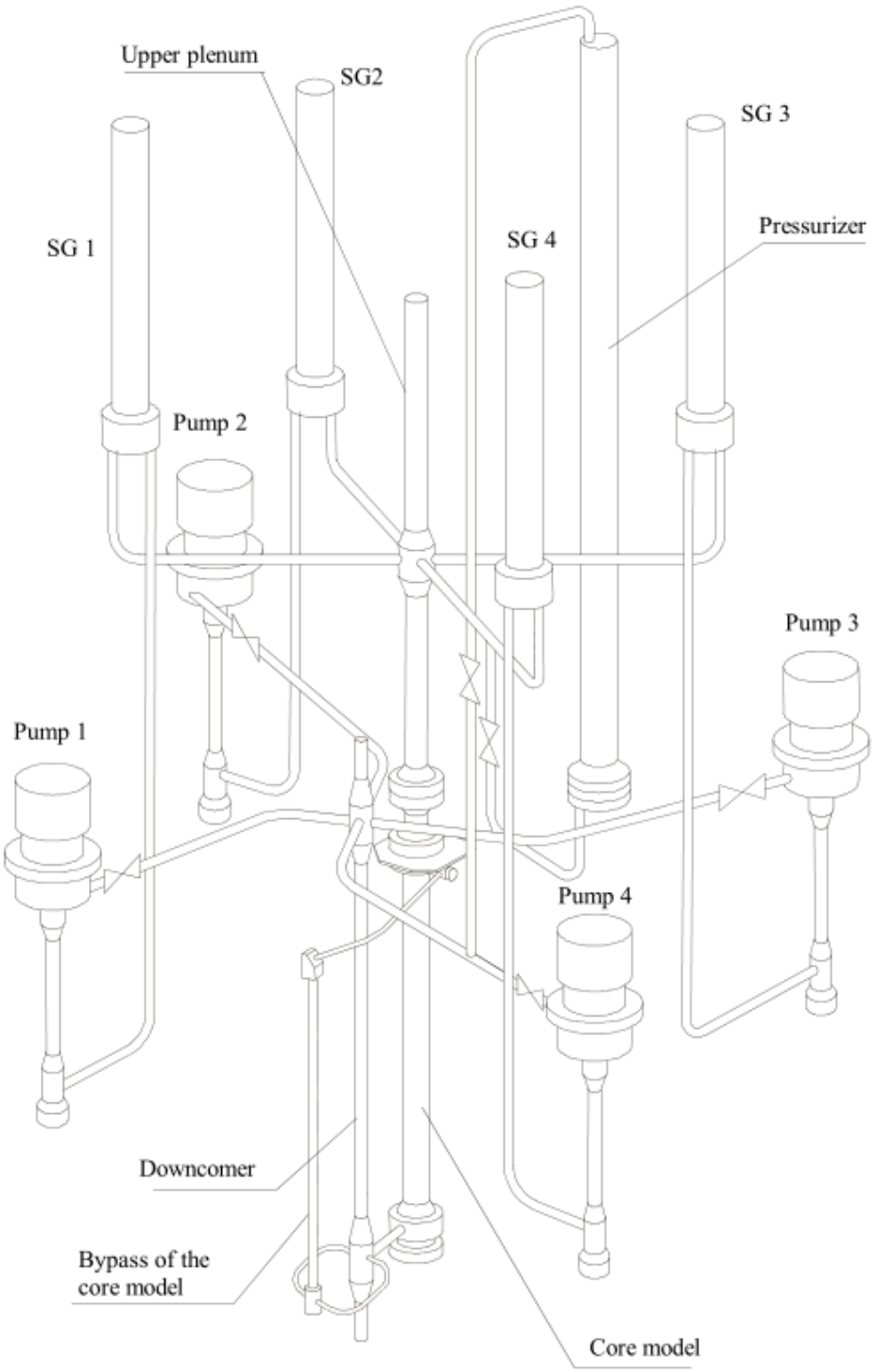

Fig. 6.3: General view of the PSB facility [135]

The model of the facility including its nodalization and main parts modelled is depicted in Figure 6.4. The core is divided into 15 nodes but only 14 of them are modelled with heat structures. The last node without the heat structure represents the upper plenum of fuel pin.

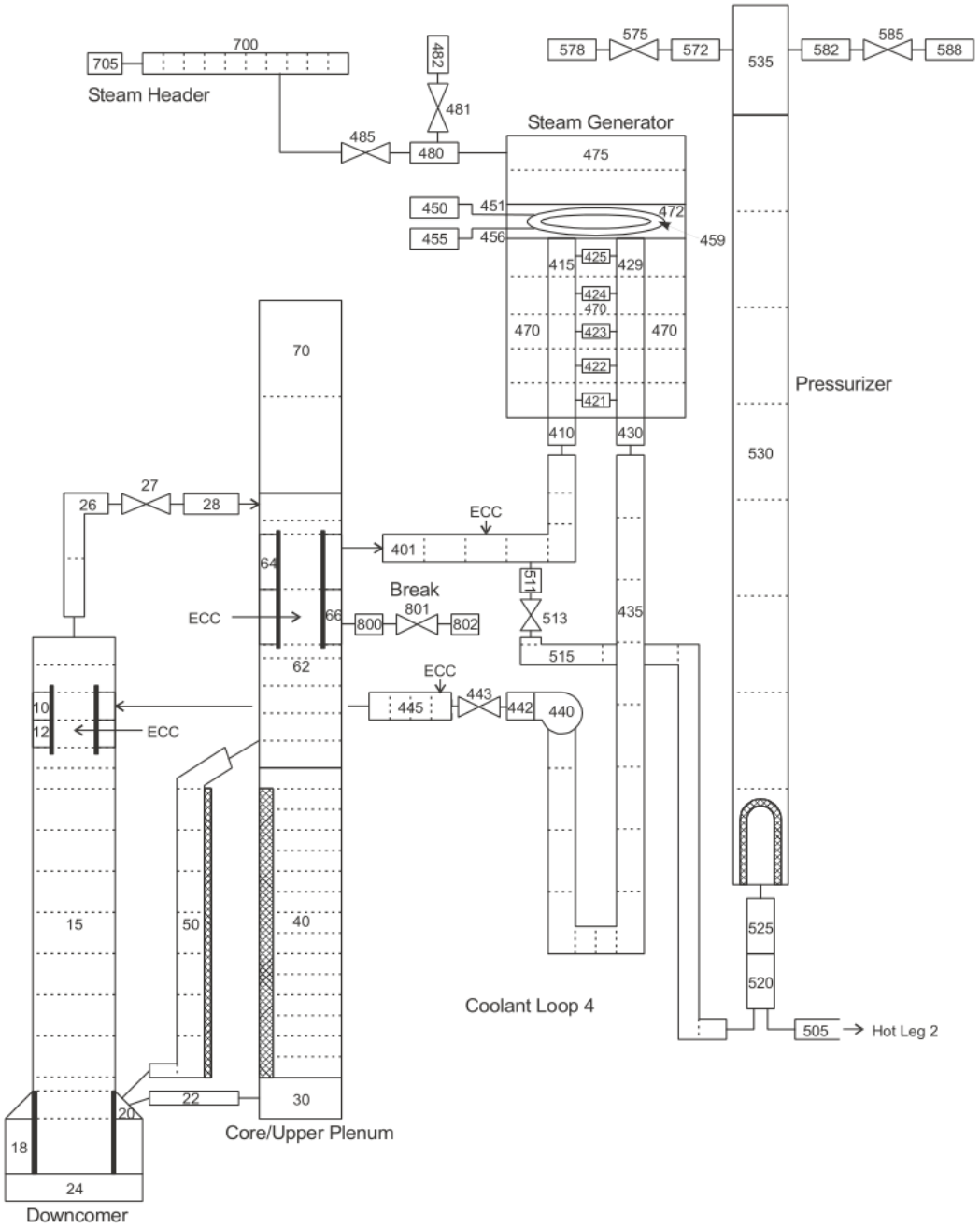

Fig. 6.4: The RELAP5 model of the PSB facility [135]

The reference [135] contains also the experimental data from the 11% Upper Plenum LOCA test. The programs g3data [138] and WebPlotDigitizer [139] were used to read the data from graphs.

The test scenario is presented in the left column of Table 6.1. The table represents the main actions of the test accident and the boundary conditions defined in the model. For illustration, the right column shows the time of each event as defined or calculated by the PSB model. One can see that there is a clear difference in the experimental and calculated data of the test by those events which were left as the variable. Similar behaviour can be thus expected in this work.

Event	**Experiment (s)**	**Calculation (s)**
Break opens	0	0
SCRAM/power decrease	5 *	5
Pressurizer heaters turned off	6	2
Main coolant pumps tripped	10 *	10
Steam generator 4 feedwater flow ends	10 *	10
Steam generator 1 feedwater flow ends	13 *	13
Steam generator 3 feedwater flow ends	14 *	14
Steam generator 2 steam flow ends	17 *	17
Pressurizer above heaters empties	19	21
Steam generator 1 steam flow ends	20 *	20
High pressure injection starts	21	13
Steam generator 4 steam flow ends	23 *	23
Steam generator 3 steam flow ends	24 *	24
Primary pressure drops below secondary pressure	86	86
Accumulator 4 injection starts	165	144
Accumulator 2 injection starts	175	139
Accumulator 3 injection starts	184	144
Accumulator 1 injection starts	194	144
Core heatup starts	222	168
Core bypass heater tripped	559	–
Experiment terminated	1037	798

* Set as boundary condition in the calculation

Tab. 6.1: Time sequence of the PSB 11% upper plenum break test [135]

The experimental data is in detail presented within the next parts of this subchapter. The experimental data from the test was used for the RELAP5/MOD3.3 code assessment. Whereas the reference [135] assess the RELAP5/MOD3.2 code version, the RELAP5/MOD3.3 version is used in this work. With the newer version of RELAP5, the model had to be validated again. In order to asset the RELAP5/MOD3.3 version, following representative set of parameters was selected:

- Upper plenum pressure
- Differential pressure in the lower portion of the core simulator
- Differential pressure in the middle portion of the core simulator
- Differential pressure in the upper portion of the core simulator
- Differential pressure in the lower portion of the upper plenum
- Differential pressure in the upper portion of the upper plenum
- Accumulator 1 liquid level
- Accumulator 1 pressure
- Break flow rate
- Pressurizer liquid level
- Pressurizer heater power

The upper plenum pressure is selected for the comparison purposes because it represents one of the most basic parameters of LOCA accidents. The same is valid for the Break flow rate. Differential pressures are selected because they represent the liquid volume along the core and upper plenum. Accumulator liquid level and pressure are evaluated as well because they represent the basic data on water inventory and ECCS characteristics. This is valid for the pressurizer liquid level as well. The pressurizer heater power is selected as the representative measure of control systems actuation.

These parameters, the comparison between the experimental data, and calculation results, are shown in Figures 6.5 - 6.15 located in the next part of this work. Sometimes a significant difference can be found between the experimental data and calculation. Reference [135] provides explanation of the physical phenomena in the system during the test as well. Some effort has been expended on explanation the differences between experimental data and calculation results.

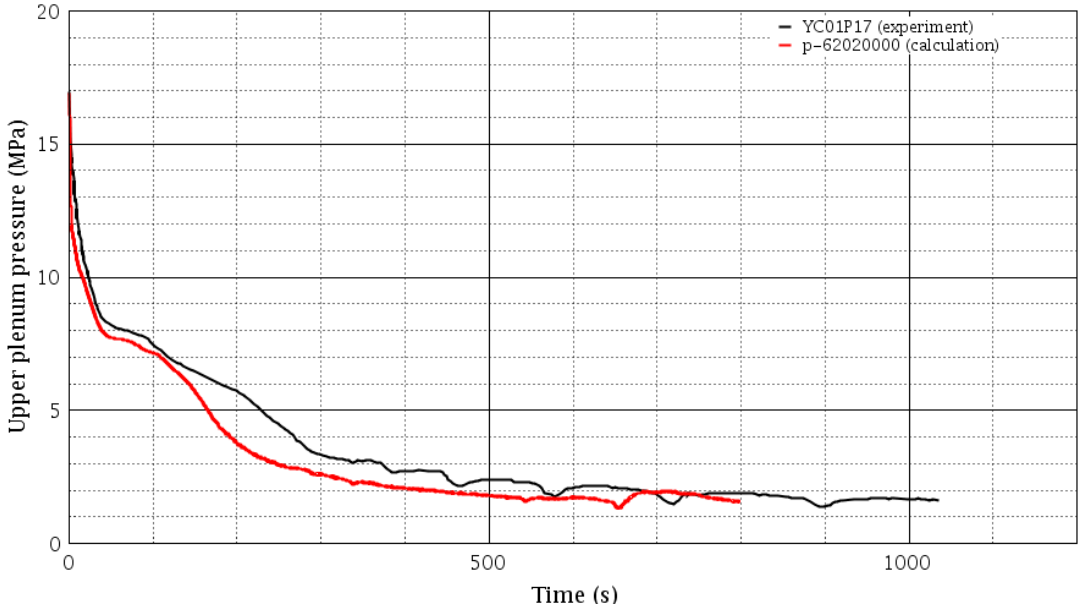

Fig. 6.5: Upper plenum pressure (calculated at the position of the break)

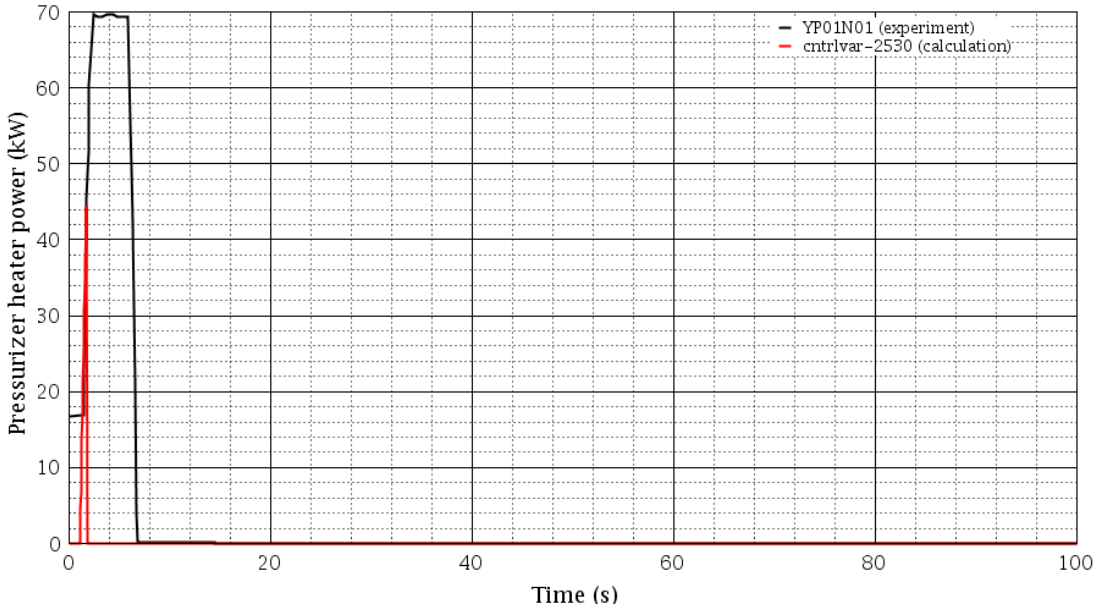

Fig. 6.6: Pressurizer heater power

Starting from Figure 6.5, the upper plenum pressure decreases more rapidly in the calculation than in the experiment. But the depressurization was slowed down approximately at the same time (50 s), as the liquid began to boil. In the experiment, accumulator (ECC) injection began near 200 s (see Figure 6.10) which increased the depressurization rate by partial condensation of the steam on cold water being injected. In the calculation, due to the faster depressurization, the ECC started earlier (near 140 s) and this further also increased the depressurization rate.

After 300 s, a cyclic behavior was observed in the experiment. This is because the ECC injection increased the steam condensation which was followed by an increase of depressurization rate. This further increased the injection flow. As the liquid level began to increase in the core, the heater rods were quenched and the vapor generation rate was increased. The higher vapor generation increased the pressure preventing the ECC water from entering the core. Without the ECC water, the water evaporated and the heater rods began to heatup again. The same effect can be observed in the calculation but it is much less pronounced as in the calculation and starts earlier at the time approx. 250 s. The earlier starting time is caused by faster depressurization and thus faster reaching the saturation temperature. The lower amplitudes are also probably caused by faster depressurization when the ECC injection is not able to provide sufficient amount of water compensating the steam amount escaping through break.

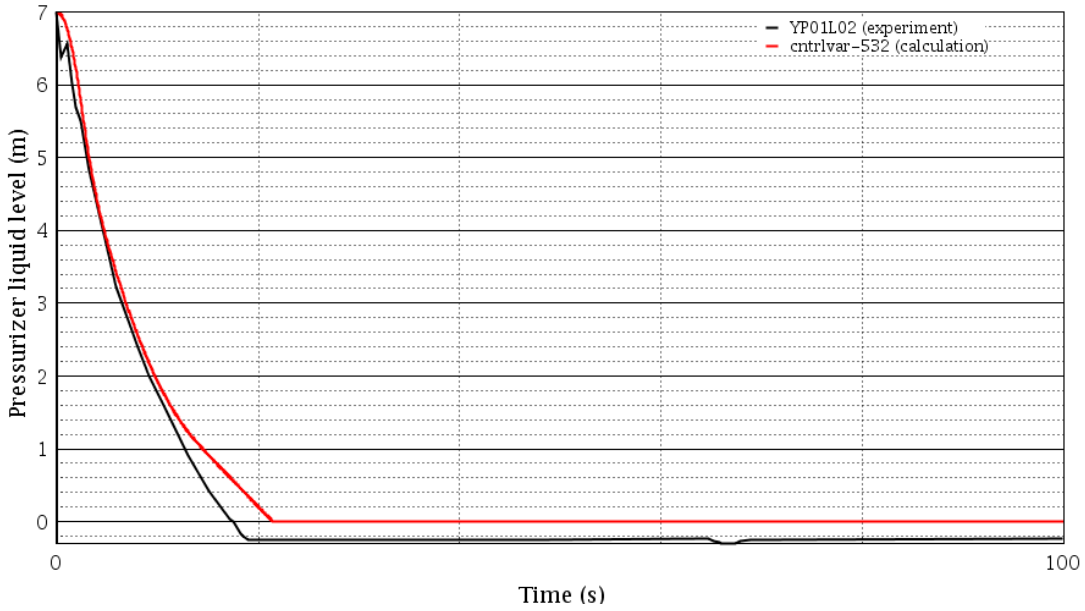

Fig. 6.7: Pressurizer liquid level (exp. data uncertainty = 0.3 m)

Figure 6.6 represents the pressurizer heater power. In the experiment, the power to the heater was shut off when the UP pressure fell below 13.73 MPa and the same condition was implemented in the model. But in the calculation, this pressure level was reached after 2 s, consequently, the pressurizer heater was turn off and did not reach the maximal allowed value of 70 kW.

Figure 6.7 represents the water inventory in the pressurizer. The zero level is considered at the position of the heater top and the maximal level is at the top of the tank. This portion of the pressurizer drained slightly slower in the calculation than in the experiment.

The calculated break flow rate is shown in Figure 6.8. The total amount of released water is approximately the same for the first 20 s. After that, the calculation overestimates the break flow rate until the time of approx. 80 s when the measured flow rate becomes higher. As a result, the amount of released water is again the same at the time 180 s and after that the amount of released water is lower in the calculation.

The pressure and liquid level in accumulator 1 are related quantities as can be seen from Figures 6.9 and 6.10. These characteristics are basically identical for all accumulators. The faster depressurization in calculation causes also the faster start of ECC injection. The start of periodic injection can be also identified at the time of 250 s as in Figure 6.5. The liquid level decrease is much ”smoother” within the first 550 s while the experiment data shows the development of ”step-wise” decrease at the time of approx. 350 s. This difference is related to the fact that the heatup process within the core was delayed in the calculation.

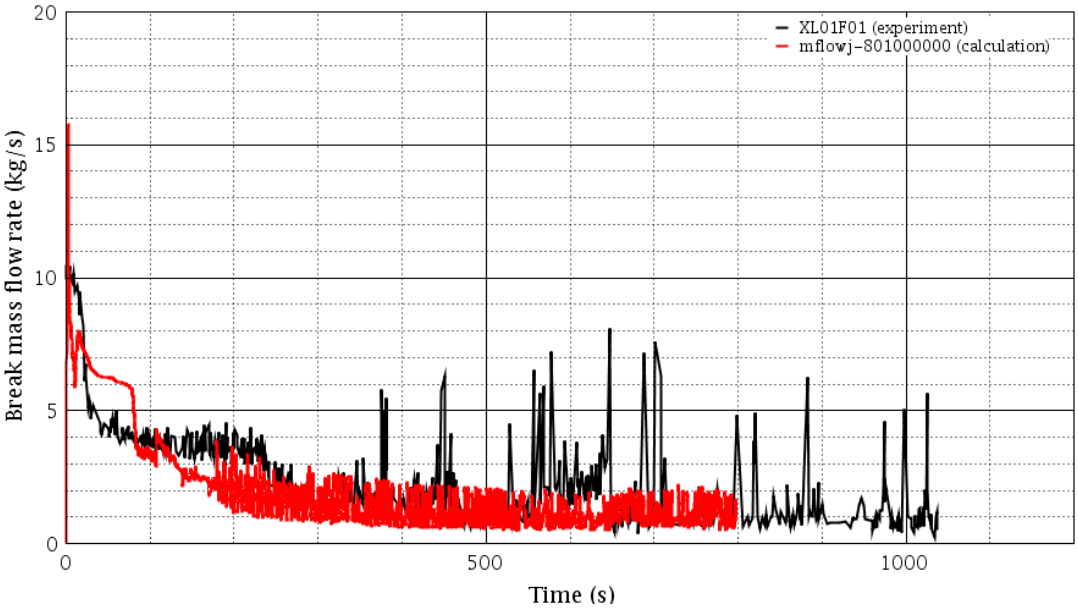

Fig. 6.8: Break mass flow rate

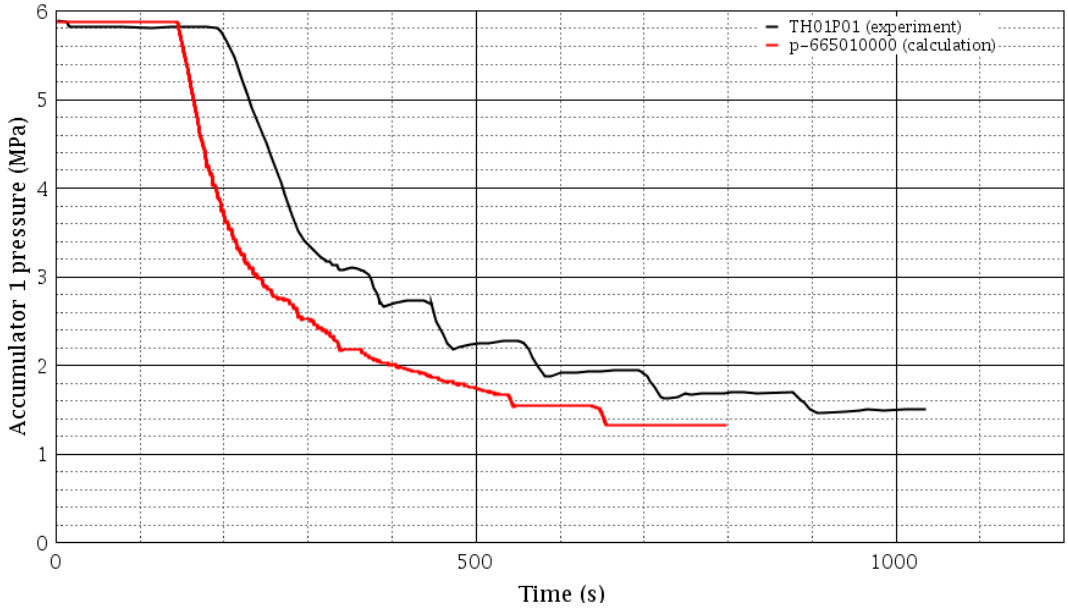

Fig. 6.9: Accumulator 1 pressure

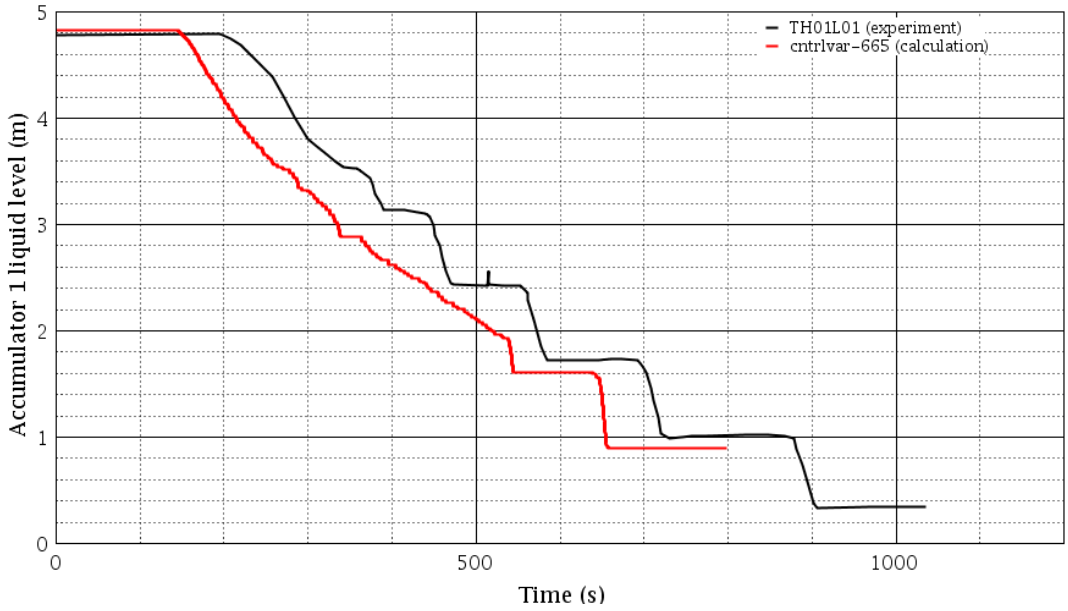

Fig. 6.10: Accumulator 1 liquid level

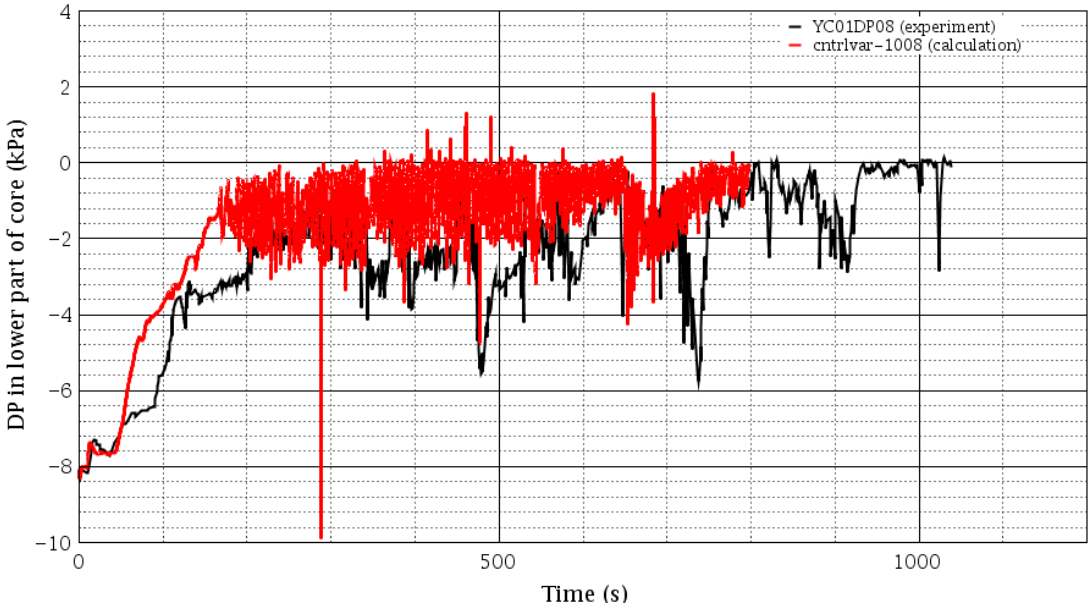

Fig. 6.11: Differential pressure in the lower part of the core

Figures 6.11 – 6.13 show the differential pressures along the height of the core. The differential pressures are equivalent to the amount of water presented between the pressure measurement points. In the beginning of calculation, there is generally a good agreement with experimental data. Later, the code overpredicts the amount of water within the lower part of the core. The peak in differential pressure around 200 s in the middle part of the core was not calculated by the code.

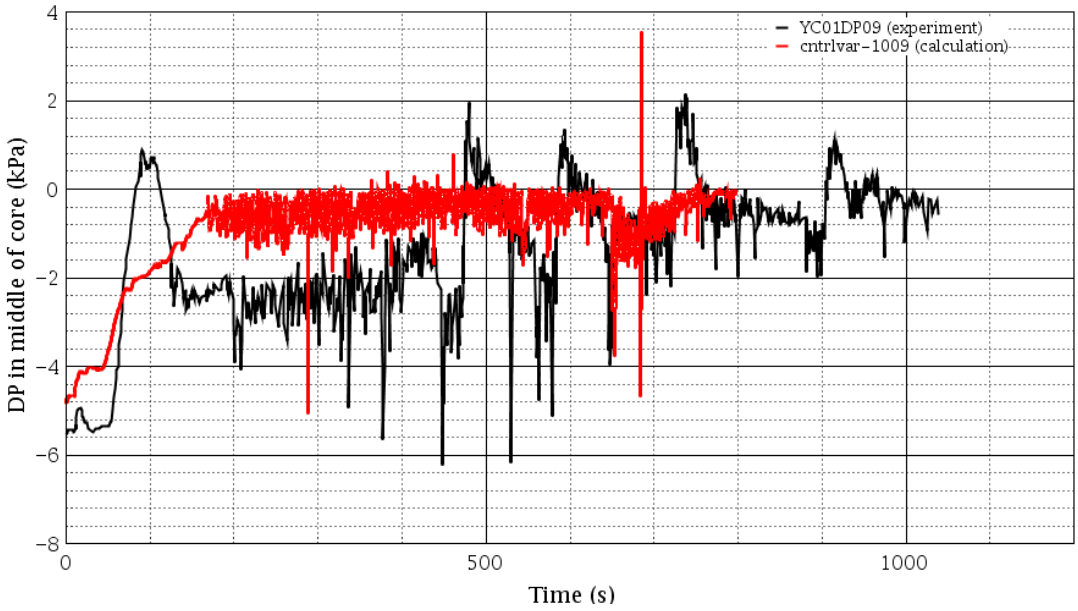

Fig. 6.12: Differential pressure in the middle part of the core

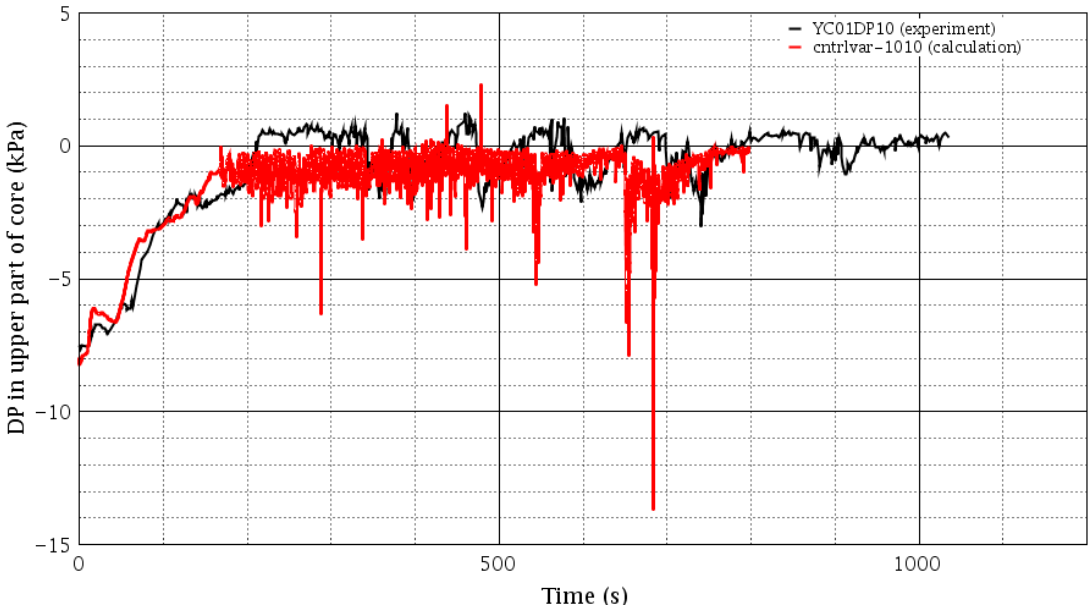

Fig. 6.13: Differential pressure in the upper part of the core

One should also note that the measured differential pressure exceeds the zero value sometimes, but this is not realistically possible. This is an indication of a problem with measurements. Both the cases, the measurement and calculation data, reflect the influence of water injection to core by pressure decrease and consequent return to wards its initial value.

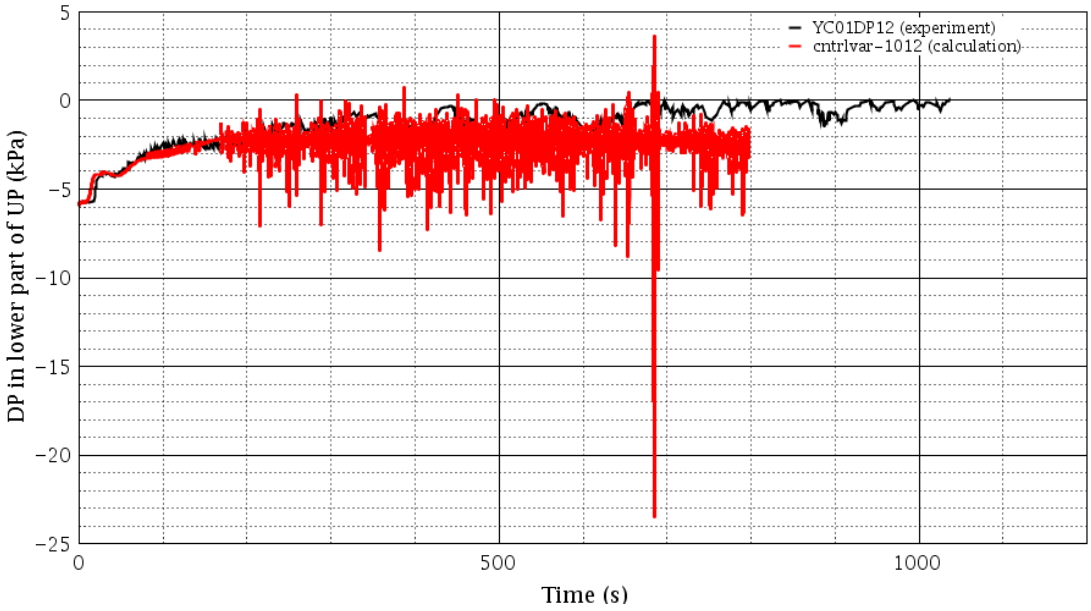

Fig. 6.14: Differential pressure in the lower part of the upper plenum

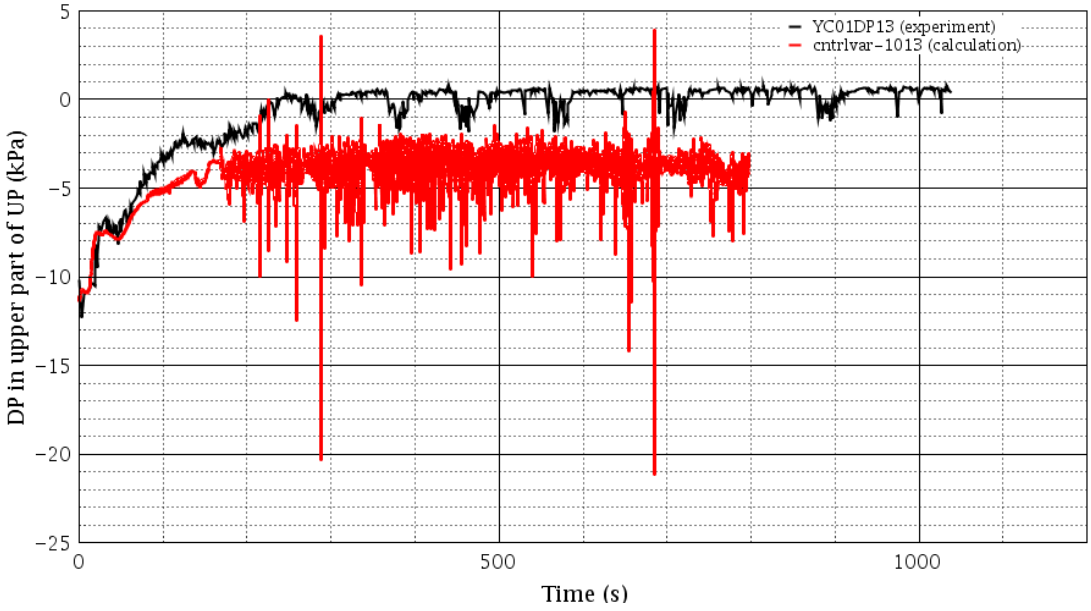

Fig. 6.15: Differential pressure in the upper part of the upper plenum

Figures 6.14 – 6.15 show the differential pressures in the upper plenum. There is more liquid retained within upper plenum in the experiment than in the calculation. The reasoning of this fact is probably the same as in validation of RELAP5/MOD3.2: parameters of the counter current flow limitation (CCFL) model between core and upper plenum are not adjusted properly and this prevents the water from falling back to the core.

The experimental and calculation data presented in Figures 6.5 – 6.15 was used for the RELAP5/MOD3.3 assessment. The code assessment was done according to a procedure established by NRC. This procedure was originally developed by LANL [140] and defines qualitative code-experimental comparison "descriptors" such as "excellent, reasonable, minimal and insufficient" [141].

The ACAP (An Automated Code Assessment Program, [142]) was used to evaluate the agreement between the calculation results and experimental data. ACAP is a program providing several statistical methods (metrics) for comparison of various statistical data sets. Each metric can be used as a single measure but normally a combination of several metrics is used using weight factor for each metric. All selected measures are then recalculated to one single number ranging from 0 to 1, which is called Figure of Merit (FOM).

As an example, conversion of the Mean Error Magnitude (MEM) to FOM is presented below. MEM is defined as:

$$MEM = \frac{1}{N}\left\{\sum_{i=1}^{N}|O_i - P_i|\right\}, \tag{6.1}$$

where O is the base data point, P is the comparative data point and N is the total number of data points. For the case of normalized data, the equation (6.1) turns into:

$$MEM^* = \frac{1}{N}\left\{\sum_{i=1}^{N}|O_i^* - P_i^*|\right\}, \tag{6.2}$$

where:

$$O^* \equiv \frac{O}{|O_{max} - O_{min}|}, \tag{6.3}$$

$$P^* \equiv \frac{P}{|O_{max} - O_{min}|}. \tag{6.4}$$

Finally, the FOM value is for the case of normalized MEM calculated as:

$$FOM_{MEM} = \frac{1}{MEM^* + 1}. \tag{6.5}$$

The relationship between FOM value and the descriptors is shown in Table 6.2. For easier distinguishing, each descriptor is indicated with a colour as well.

Based on recommendation in [144] for time dependent data without oscillations, four metrics and their weightings, respectively, were selected for the code assessment. These four metrics are listed in Table 6.3.

Descriptor	FOM range (-)	Color
Excellent agreement	FOM >= 0.77	green
Reasonable agreement	0.67 =< FOM < 0.77	blue
Minimal agreement	0.59 =< FOM < 0.67	yellow
Insufficient agreement	FOM < 0.59	red

Tab. 6.2: Magnitude of FOM descriptors used for assessment of TH codes [143]

Metric	Weight factor(-)
Size-Independent "Predicted – Perfect" L2 Norm	0.15
Degree of Randomness	0.15
Mean Error Magnitude	0.35
D'Auria FFT (k=0)	0.35

Tab. 6.3: Metrics and their weights used for validation of the PSB model against experimental data [144]

Parameter	FOM (-)	Assessment
Upper plenum pressure	0.916	Excellent agreement
Differential pressure in the lower part of the core	0.722	Reasonable agreement
Differential pressure in the middle part of the core	0.728	Reasonable agreement
Differential pressure in the upper part of the core	0.731	Reasonable agreement
Differential pressure in the lower part of the UP	0.669	Minimal agreement
Differential pressure in the upper part of the UP	0.673	Reasonable agreement
Accumulator 1 liquid level	0.858	Excellent agreement
Accumulator 1 pressure	0.827	Excellent agreement
Break flow rate	0.75	Reasonable agreement
Pressurizer liquid level	0.936	Excellent agreement
Pressurizer heater power	0.618	Minimal agreement

Tab. 6.4: FOM values for selected parameters of the LOCA experiment

Using the above stated metrics and their weightings, FOM factors were calculated for each parameter and the validation of the model was done. The result of the validation assessment is shown in Table 6.4.

In general, the code shows a reasonable agreement especially as far as the differential pressure in the core and upper plenum is concerned. But it is possible to see excellent agreement between experiment and calculation especially within (roughly) the first 80 s. Within this period, the natural convection played the major role in the system (the primary pressure dropped below the secondary by the time 86 s).

The code shows also reasonable agreement for the break flow rate simulation. But it must be mentioned here that break flow rate calculation is critical for this type of simulation. The break flow is influenced by settings of break discharge coefficient which was set according to general recommendation given in the RELAP5/MOD3.3 input manual vol. V [145]. Selections of different discharge coefficient has a significant impact on the results of the whole simulation. The upper plenum pressure is judged to be in excellent agreement. The depressurization was faster in the calculation on the one hand, on the other hand the pressure simulation reflects all important processes which happened.

Additional information on the code accuracy can be gained by an analysis of the heater rod temperatures during the experiment and calculation. The experimental and calculated heater rod surface temperatures are presented in Figures 6.16 - 6.17.

The first worth of mentioning is the different time. The experiment was terminated at 1037 s in order to prevent the heater rods from damage. The simulation was terminated at 798 s when the stainless-steel reached the temperature of 1073 K and thus exceeded the temperature range for which the stainless steel properties were defined within the original model.

The next issue which should be discussed is the different time of heatup start and heatup progress. There is a time discrepancy about 50 s between the start of the measured and calculated heatup. A similar time difference was observed in the calculation with RELAP5/MOD3.2 as well. In [135], this is also explained by faster depressurization in the core (the lower core pressure results in earlier boiling).

After the start of heatup, the core went through a subsequent series of heatups and quenching as a response of ECCS water injection (see Figure 6.10). Author of this work suggest the following explanation of the steep temperature increase at 350 s: with faster depressurization and more extensive boiling, more of the length of the heating rods is involved in the heat up process and the ECCS water injections are not able to sufficiently cool down the core.

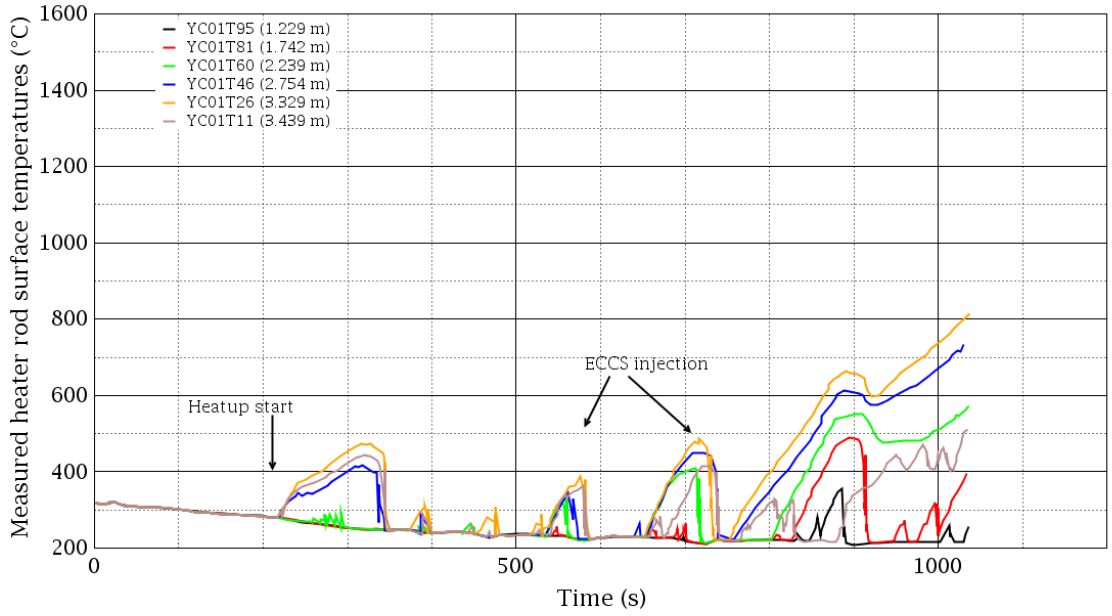

Fig. 6.16: Measured heater rod surface temperatures during the LOCA test [135]

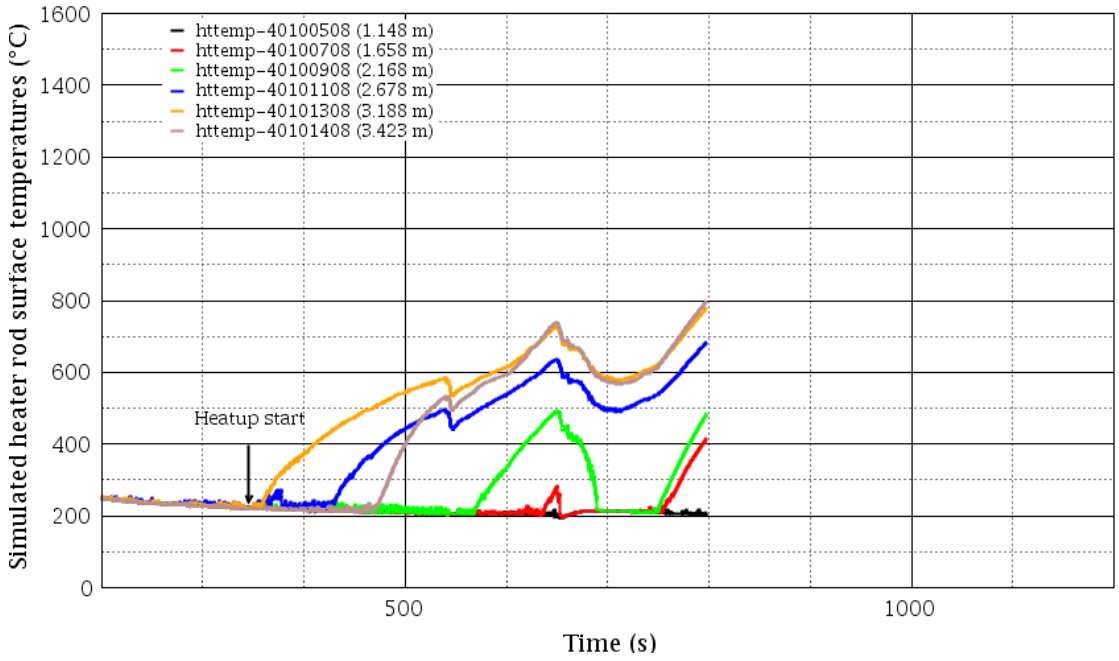

Fig. 6.17: Simulated heater rod surface temperatures for the LOCA test

6.3 The PSB model modification

As mentioned at the beginning of this chapter, the PSB model had to be modified in order to be able to predict the influence of fuel modification on the accident management. Only the heating rods were subjected to modification, their cross section and geometry are depicted in Figure 6.18.

As the representative fuel assembly for the PSB heating rods modification, the VVER-1000 TVSA-T fuel assembly [136] was selected. This type of fuel assembly shares the same outer diameter of fuel pin (heating rod). It has a cladding thickness of 0.65 mm and pellet outer diameter of 7.6 mm. To be consistent with the PSB model, no inner hole within the fuel pellet has been modelled (nevertheless, the inner hole has been not used later by the modified TVSA-T [146, 147, 148]). In the modified model, the cladding has been modelled as pure zirconium and pure helium was assumed in the fuel gap.

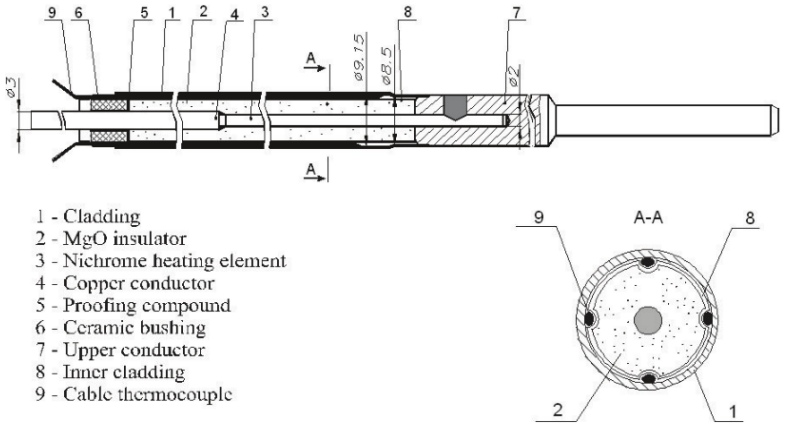

Fig. 6.18: Cross sections of one heating rod of the PSB facility [141]

Next, the temperature range of the stainless-steel properties have been extended because the material properties were defined only up to 1073 K which is insufficient limit for the accident modelling. Currently, the temperature range is defined up to the 2000 K. It is not clear from [135] what type of stainless steel was used. Thus, the procedure used in part 3 of [101] was used in this work as well. The data original points defined in the model were extrapolated up to the temperature 1671 K (cca 1400 °C) where the 304 stainless steel starts melting. The volumetric heat capacity was defined as constant after that temperature and the thermal conductivity was decreased to one half of the value for the temperature of 1727 K where the melting stops. The thermal conductivity remains constant after 1727 K.

The original and extrapolated values of thermal conductivity and heat capacity are depicted in Figures 6.19-6.20.

On the other hand, the temperature range extension has the only sense for an ideal TH modelling. In the reality, the core undergoes a structural deformation process during the accident because of the chemical reaction between zirconium and steam and other phase changes or reactions of other materials. E.g., the reaction between zirconium and steam was widely reported as one of the major problems which must be avoided during the accident. Based on [149], the reaction occurs in the temperature range of 1100-1500 °C, particularly at 1200 °C, but some literature mentions the beginning at 900 °C ([150] for example). This reaction is exothermic which means that it introduces another significant amount of heat into the system and besides large cladding temperature gradients an uncontrolled temperature escalation may be the next consequence. One of the products of this reaction is the ZrO_2 which further reacts with UO_2 at 1310 °C [151]. Approximately at 1400 °C, the stainless steel, an important structural material within the core, starts to melt.

These and other reactions and their effects have significant impact on the scenario of accident by promoting of the core degradation process thereby restricting coolant channel. But for simplicity, they were not considered in the predictions. The TH simulations presented in this work are limited to the conditions that the geometry of the PSB facility remains unchanged, no chemical reactions occurs and the heat is generated by the fuel pins.

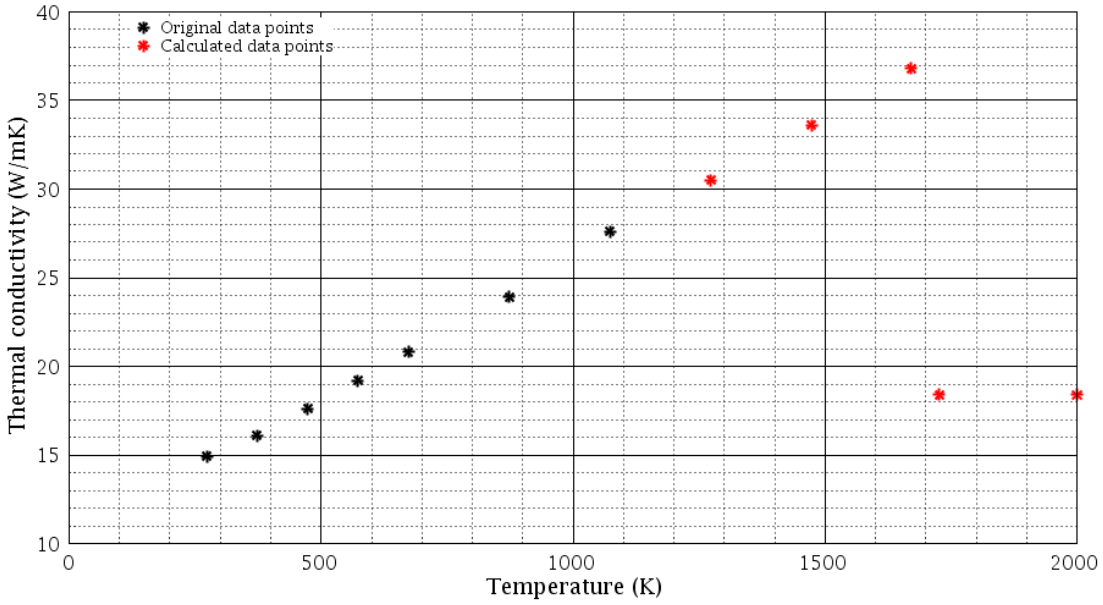

Fig. 6.19: Enlarged thermal conductivity temperature range of the stainless steel. The code interpolates between the depicted points.

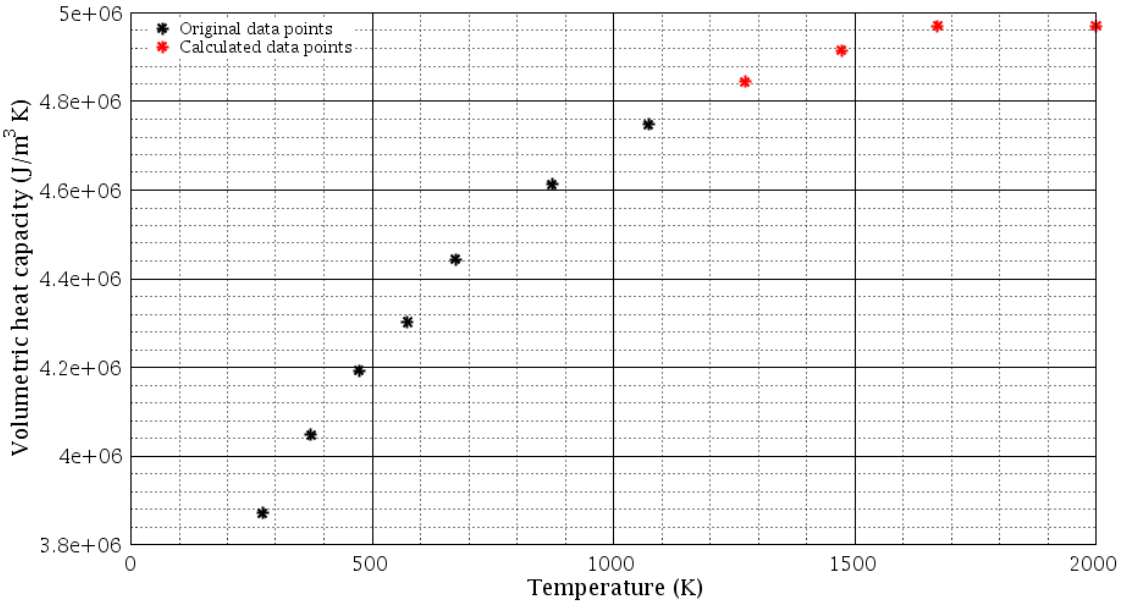

Fig. 6.20: Enlarged heat capacity temperature range of the stainless steel. The code interpolates between the depicted points.

6.4 Influence of the fuel burnup

The modified PSB model allows to analyze the influence of fuel burnup and SiC content on the management of the LOCA type accident. This is done by modification of the thermal conductivity and the heat capacity of the fuel. Whereas the thermal conductivity function was defined as dependence on burnup and temperature, the heat capacity is defined only as a function of temperature.

Omitting the burnup dependence in the heat capacity function is possible because the neutron irradiation effect is negligibly small for the case of SiC [51] and reference [90] reports only a small increase with burnup in heat capacity for the case of UO_2. On the other hand, SiC has larger heat capacity than that of UO_2 and therefore it has to be taken into account. The heat capacity of the composite fuel was calculated through the simple rule of mixtures (Voigt model - eq. 2.1) where the mixture heat capacity is weighted by the volume fractions of the constituents.

In this subchapter, the influence of the burnup will be analyzed in the first step. This will be done for the case of UO_2 only. The influence of the SiC content will be analyzed in the second step in the following subchapter. Consequently, the separation of the analysis into two steps will help to easily distinguish their separate influence.

The influence of the burnup was analyzed for five fuel burnup stages: 0, 15, 30, 45, and 60 MWd/kgU, respectively. Figure 6.21 shows the values of thermal conductivity. The thermal conductivity of the UO_2+10 vol.% is depicted as well. The composite fuel thermal conductivity was calculated with respect to the degradation of the SiC thermal conductivity (the degradation model is presented in section 2.4.4). For all the cases presented in Figure 6.21, the fuel steady state temperature profiles are depicted in Figure 6.22 as calculated by RELAP5. It is interesting to see that the influence of SiC is more pronounced at the final burnup stage.

With regards to the original version of the PSB facility model, the core of the PSB facility is modelled using 14 nodes thereby providing 14 temperature - time vectors for the analysis. For the sake of clarity of the graphs, this amount of data was limited to two main parameters: average cladding temperature and maximum cladding temperature. The maximum cladding temperature is not calculated for any specific location along the core. Instead of that, this parameter is calculated as the maximum temperature of any of the 14 nodes. The average and maximum cladding temperatures are shown in Figures 6.23 and 6.24.

For the WWER reactors, there is a 1200 °C temperature limit which defines the acceptance criteria of the BDBA accident [109]. Needless to say, this temperature limit is almost the same for the PWR reactors, according to the NRC regulations. That is why, this temperature limit is also depicted in Figure 6.24.

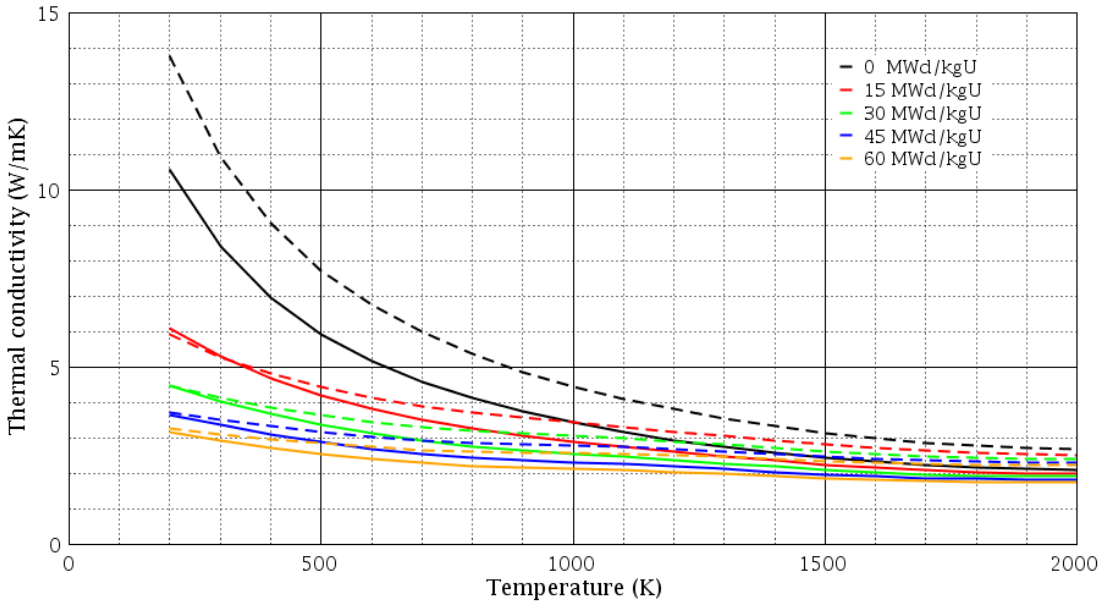

Fig. 6.21: Thermal conductivity of the fuel at different burnups used in the analysis (solid line - pure UO_2, dotted line - UO_2 + 10% SiC composite)

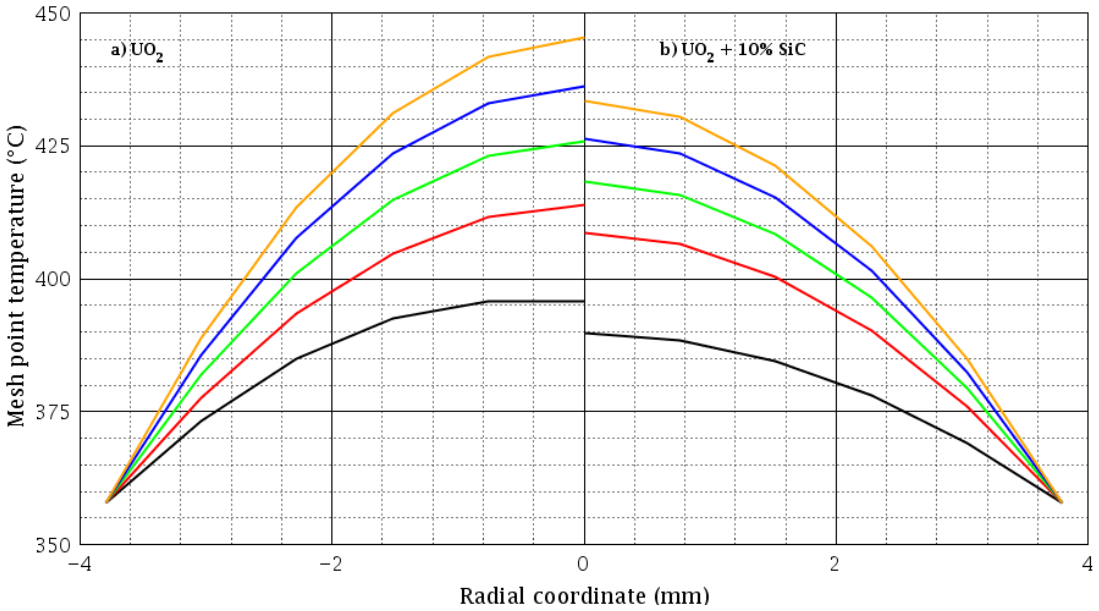

Fig. 6.22: Temperature profile within the fuel pellet calculated for standard UO_2 fuel (left side) and composite UO_2 + 10% SiC fuel (right side) at different burnup stages defined in Figure 6.21.)

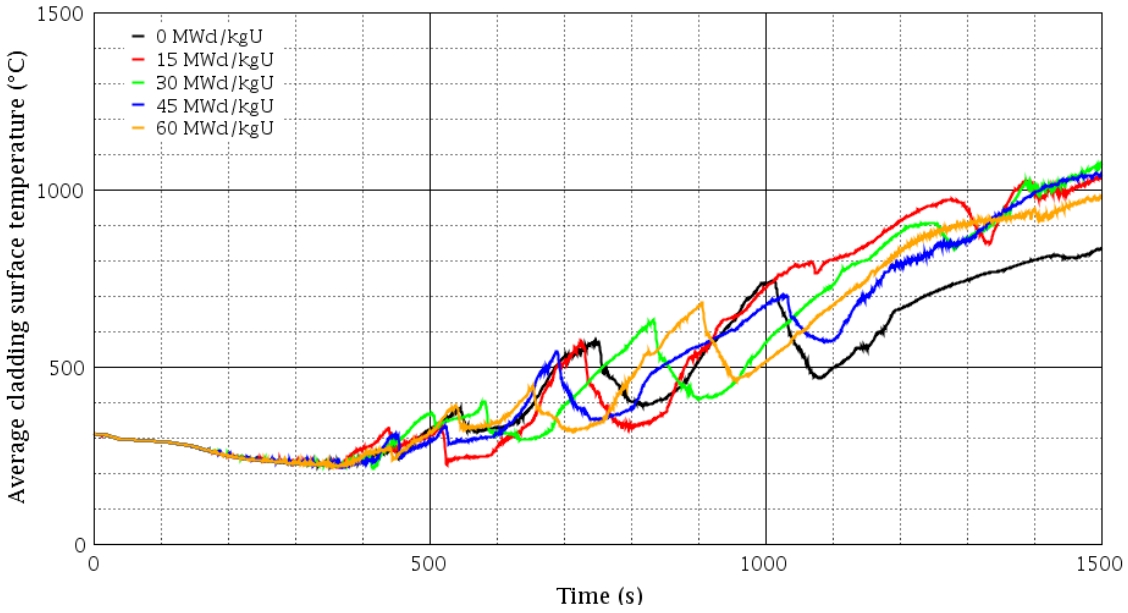

Fig. 6.23: Predicted average cladding temperatures for different burnups during the LOCA accident

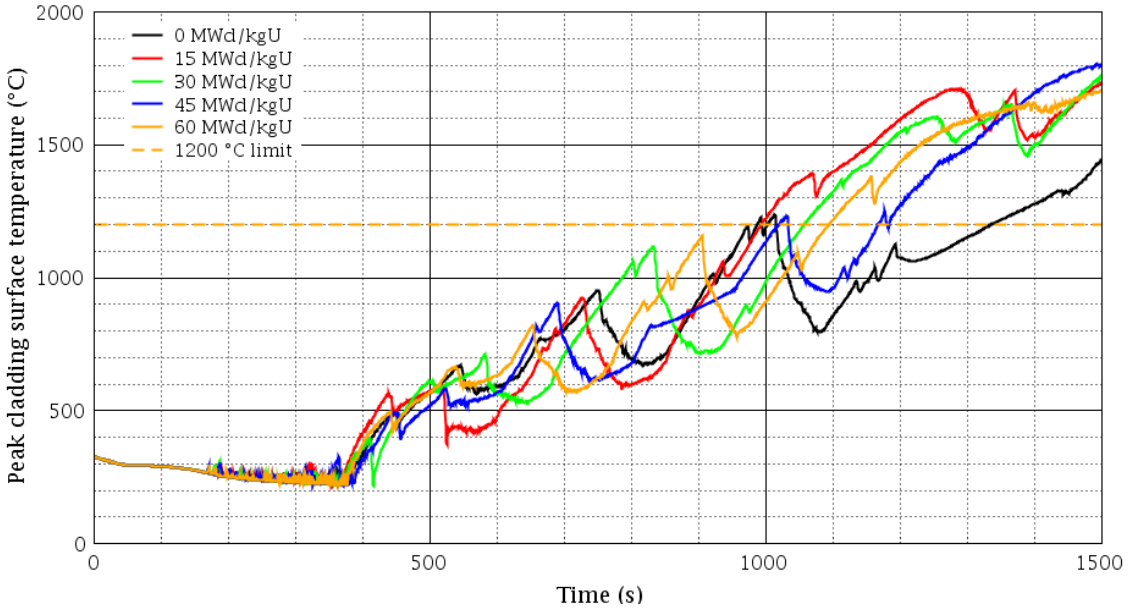

Fig. 6.24: Predicted peak cladding surface temperatures for different burnups during the LOCA accident

One can clearly see that both average and peak cladding temperatures pose the same tendency to raise. But the peak cladding surface temperature data are not influenced by the lower cooler parts of the fuel pins and thus the temperature changes are more pronounced. The temperatures increase with time having the typical peaks caused by ECCS water injections. However, while there is a sharp temperature increase around 400 s for all the cases, there is no visible time trend in the peak formation after this time. This is valid especially after the time of 500 s. It is interesting to see that all cases have a similar trend and are close together thereby creating a kind of a "temperature band".

The maximum temperature limit was reached shortly before 1000 s of the simulation time and all predictions reached this temperature limit within less than 200 s after that. But it may be noticed that the temperature dependence for 0 MWd/kgU, which reached this temperature limit as the first one, returned back below this temperature limit within approx. 80 s and it exceeded the temperature limit again at the time 1335 s. Similar situation happened in the prediction for the 45 MWd/kgU burnup as well.

The similar behavior of all predictions is an indication that there is no (or very little) influence of the burnup on the process of the core heatup and accident management. The main parameters are possibly the ECCS water inventory, the ECCS setup, the core depressurization rate and the core power after the shutdown. This conclusion should be valid especially for the classical LWR reactors fueled with fuel assemblies with different burnups. In such a case, it would be meaningful to omit the burnup sensitivity study and one simulation for an "average" burnup of a representative FA should be sufficient in order to obtain a representative prediction.

The postulate on burnup independence can be next supported by the plot of the heat being transferred from the core which is represented by the total heat flux from the core to the coolant.

Figure 6.25 represents a detailed analysis of the core to coolant heat flux for each burnup case. The upper graph shows the actual heat fluxes with detail of the very beginning of the prediction. The lower graph demonstrates the integrated heat fluxes which were divided by the integrated heat flux of the prediction with 0 MWd/kgU burnup. The detail of the first graph reveals that there is a clear dependency of the core to coolant heat flux on the burnup. With higher burnup, the heat being extracted from the core is higher. This is an important detail because the amount of transferred heat significantly influences all other parameters related to the coolant pressure, temperature and water steam mixture quality. Given to fact that coolant pressure is the most basic parameter for the emergency systems (at least in the PSB facility model), the core to coolant heat flux plays almost an essential role in the accident scenario. This simple postulate, however, needs to

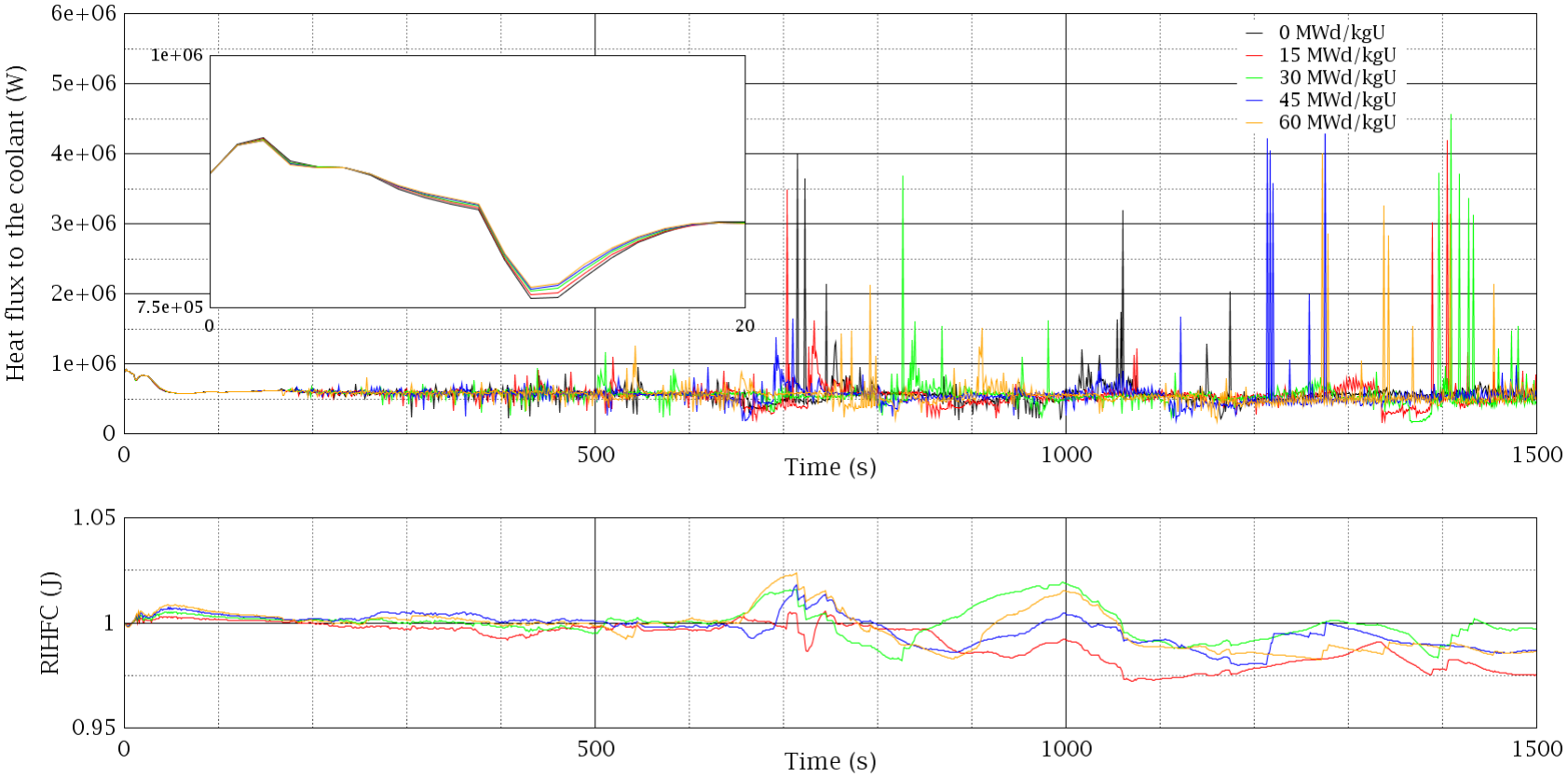

Fig. 6.25: The total heat flux from fuel pins to the coolant and Relative Integrated Heat Flux to the Coolant (RIHFC) - results are related to the simulation for 0 MWd/kgU

be more explained and needs to be introduced in relation to other processes acting during the accident predictions.

For each burnup case, the depressurization rate is slightly different. E.g., the primary pressure falls below the secondary pressure with the time difference of 0.1 s between the cases for lowest and highest burnup. But the pressure has the influence not only on the core to coolant heat flux, but on many other phenomena, like for example mass flow in loops, mass flow in adjacent systems (downcomer and bypass), start of ECCS systems, steam condensation and other. Naturally, these other phenomena are in mutual relation and deviation in one system has impact on other systems. The different depressurization rates cause small deviations in all above mentioned systems and processes. The initially isolated deviations accumulate, affect each other and, as consequence, the logical distribution of the integrated heat fluxes changes dramatically around 170 s in the lower graph.

Given to the relatively large complexity of the model, it is difficult to identify the most important initial processes which causes this abrupt change in the sequence of the relative integrated heat fluxes. The term "butterfly effect" describes the situation after 170 s quite well. After the time of 170 s, the initial heat inventory represented by the temperature profile within the fuel pellets plays almost no role and thus the scenario of the most severe late part of the accidents is basically unaffected by the initial value of thermal conductivity. It seems that the ECCS setup (water inventory, length of tubes, their diameters, pressure limits on ECCS activation etc.) plays key role in accident management.

In conclusion, the most important finding, drawn from this subchapter, is that the improvement in thermal conductivity contributes to mitigation of accident only in the first stages of the LOCA accidents. The consequent development of the accident depends mainly on the other parameters affecting the accident, like for example the response time of ECCS, mass flow rates and water inventory of ECCS injections, system capability of heat removal, decay heat generation etc.

6.5 Influence of the SiC content

In the previous subchapter 6.4, the burnup change was represented only by the modification of the thermal conductivity. As will be shown in this part of the present work, the conclusions drawn for the standard UO_2 fuel burnup predictions are also partially valid for the analysis of the accident with the composite fuel.

Apart from the burnup sensitivity study, where only the influence of the thermal conductivity on the accident progress has been investigated, the SiC addition affects the fuel thermal conductivity and fuel heat capacity as well. The increase in heat capacity after addition of 10% SiC is relatively small, as can be seen in Figure 6.26, but it will still have some influence on the accident progress because the higher heat capacity mirrors in higher thermal inertia during time transients.

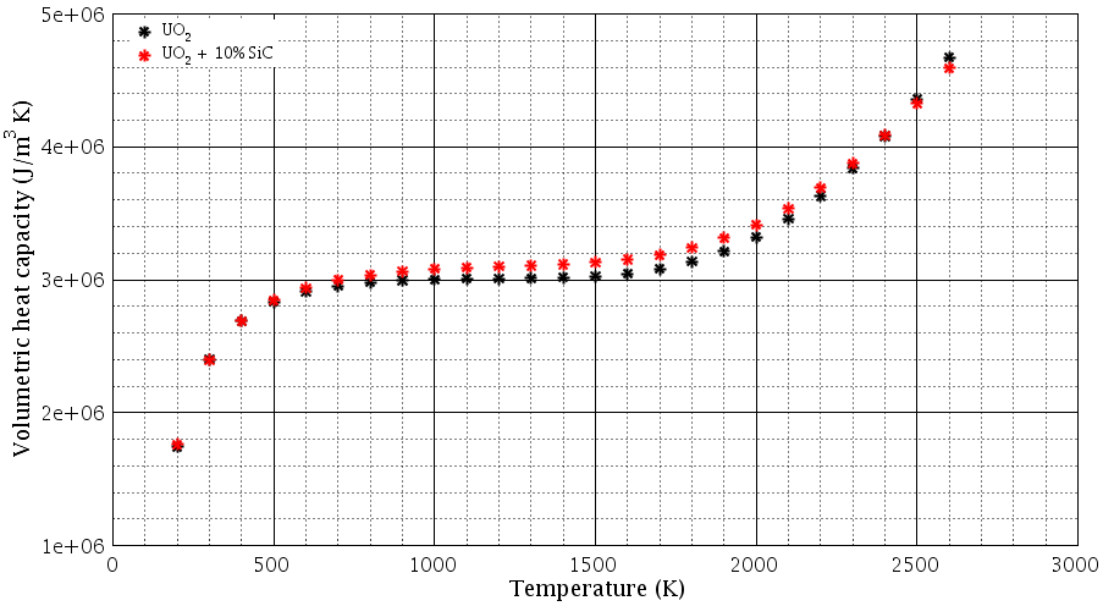

Fig. 6.26: Heat capacity functions of UO_2 and UO_2 + 10% SiC used in RELAP5 calculation

The same simulations like in the previous subchapter has been carried out and comparison with standard UO_2 fuel burnup cases are shown in Figures 6.27-6.31. But instead of direct comparison of each case, the results were reprocessed in terms of determining the maximal and minimal values of peak cladding temperatures. Based on the data presented in these figures, the span of the predicted temperatures was calculated, which is depicted in Figure 6.32 in the form of upper and lower limits.

The first issue in Figure 6.32 which is worth mentioning and which is visible at first glance is the span of the temperatures bands. The temperature span of the composite fuel is observed to be clearly thinner than that of standard fuel. It seems that

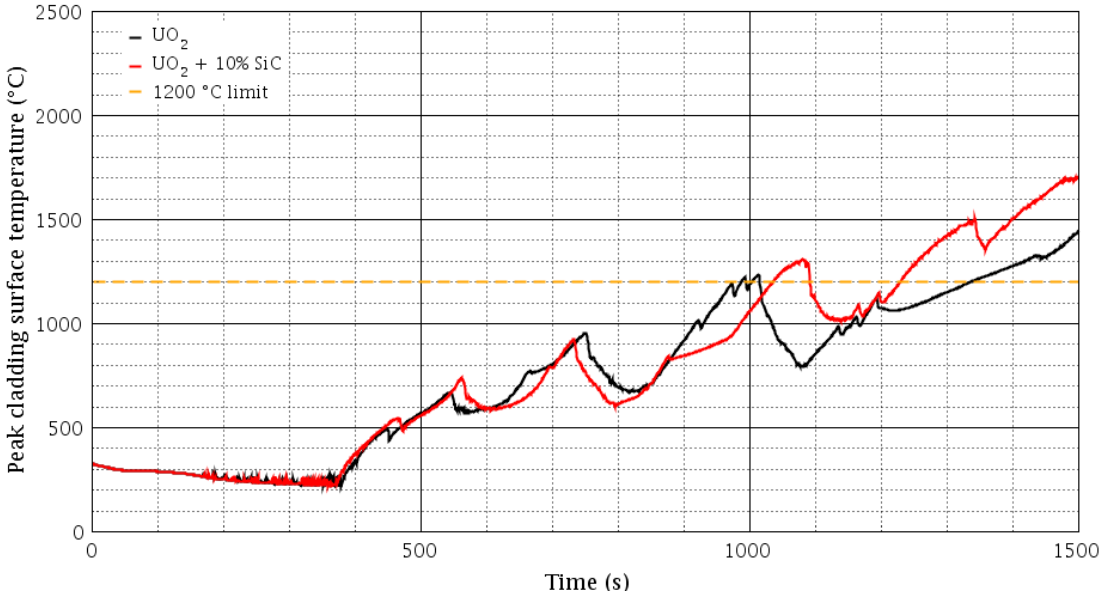

Fig. 6.27: Prediction of peak cladding temperature for burnup of 0 MWd/kgU

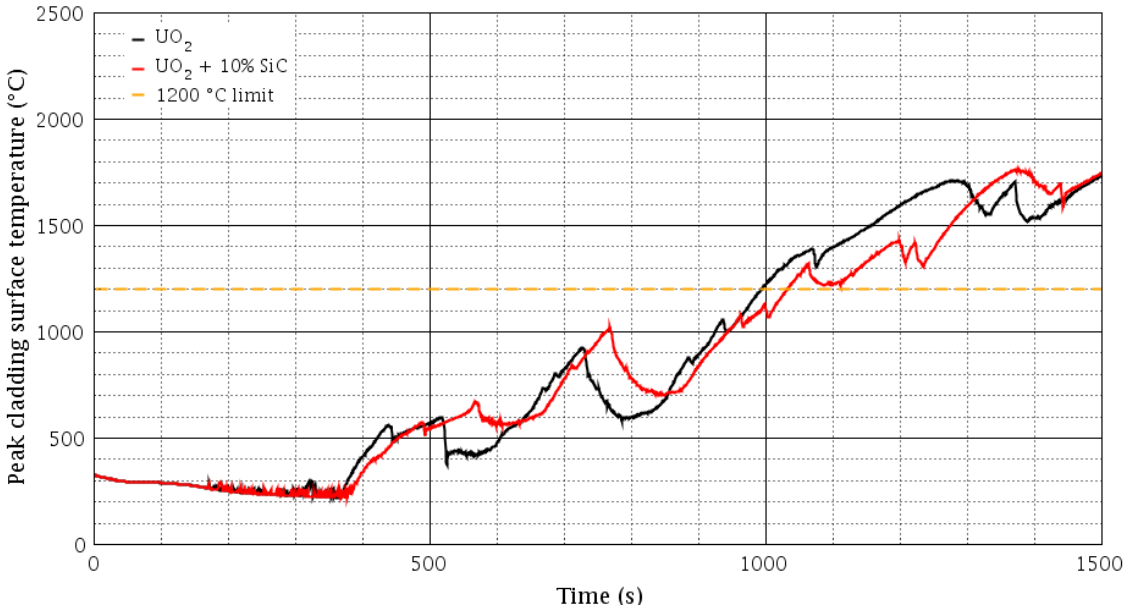

Fig. 6.28: Prediction of peak cladding temperature for burnup of 15 MWd/kgU

enhancement of the heat capacity contributes to thermal stability during simulations. Another aspect of this is the fact that for most of the period the composite fuel temperature span seems to be encompassed within the standard fuel temperature span. But the second observation is very questionable because in order to confirm this conclusion, more precise study should be done which would be based on the calculations for more burnup cases. But in general, the maximal temperatures predicted for the composite fuel appear to be almost the same as those for standard

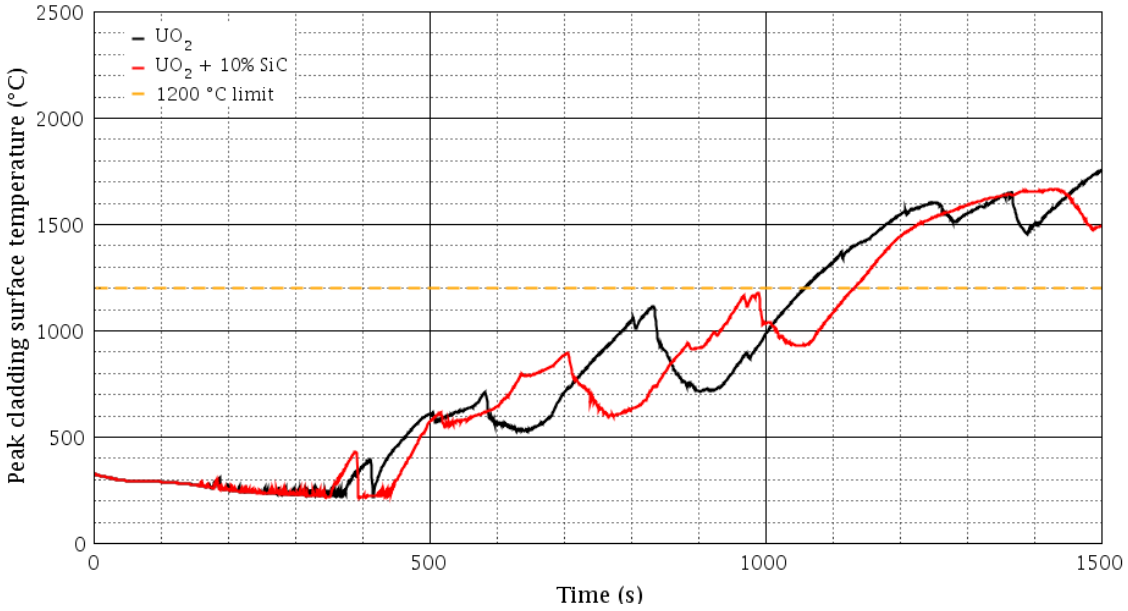

Fig. 6.29: Prediction of peak cladding temperature for burnup of 30 MWd/kgU

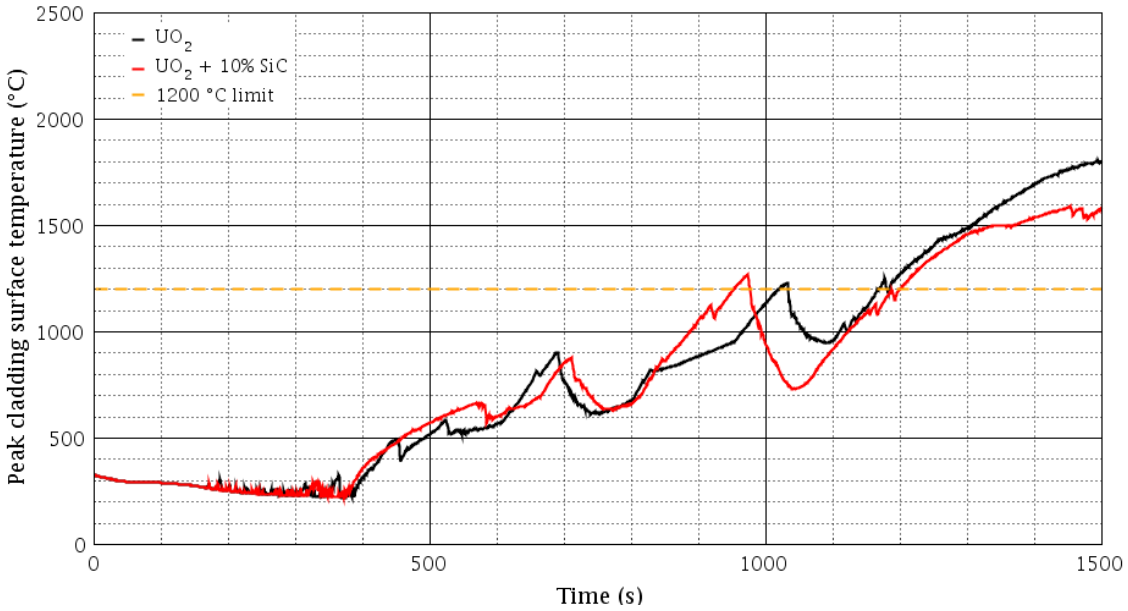

Fig. 6.30: Prediction of peak cladding temperature for burnup of 45 MWd/kgU

fuel until 1000 s, after this time the maximal composite fuel temperatures appear to be lower. A related point to consider is the lower limits. The lower limit of composite fuel is found to be the same or higher for most of the time and especially at higher temperatures. This is slightly negative finding from the point of view of the excepted LOCA scenario because this gives an indication that coolability of the core may be expected to be lower for this type of fuel.

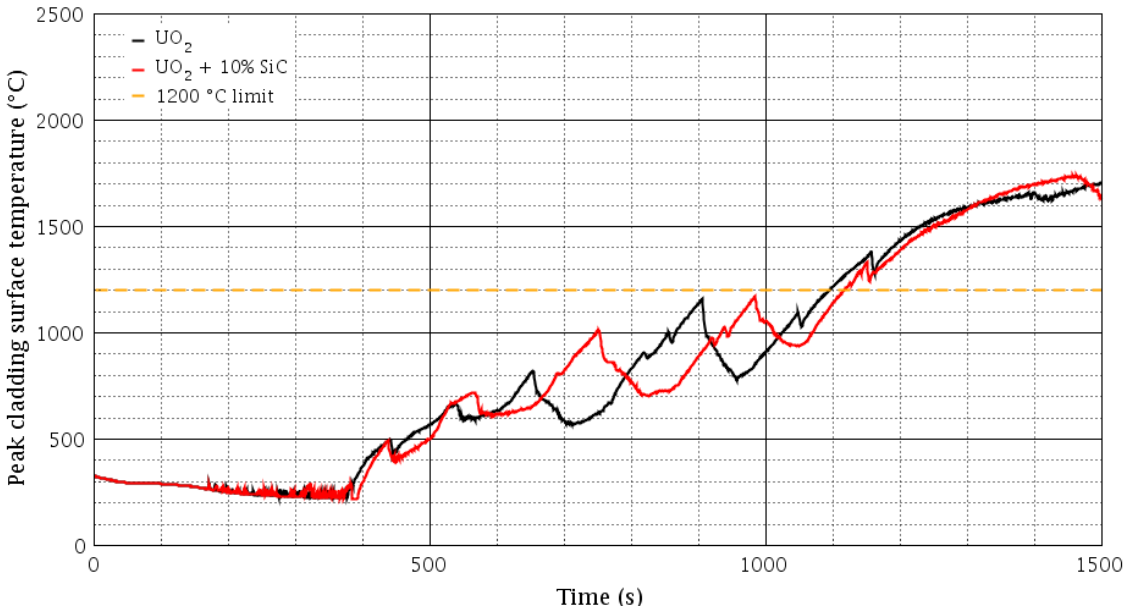

Fig. 6.31: Prediction of peak cladding temperature for burnup of 60 MWd/kgU

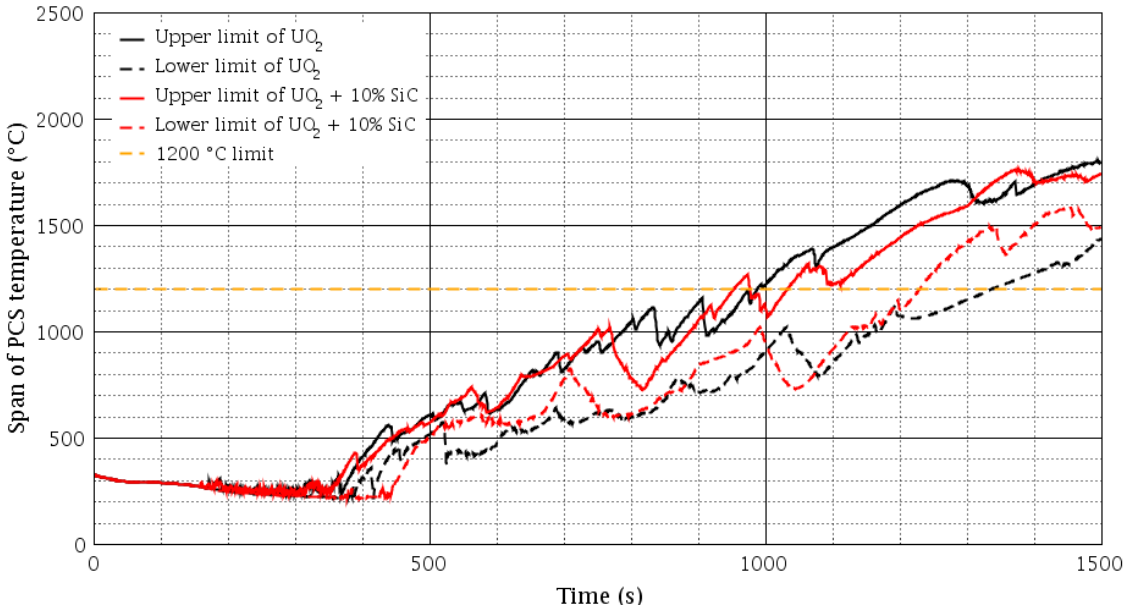

Fig. 6.32: Span of the cladding temperatures presented in Figures 6.27–6.31

6.6 Initial and boundary condition of the FEMAXI response simulation

This subchapter defines the initial and boundary conditions which were used in the FEMAXI calculation of the composite fuel response of the accident (accident response simulation). In total, 10 accident response simulations were performed based on the initial and boundary conditions described below. Five of the accident response simulations were performed for the standard UO_2 at burnup stages of 0, 15, 30, 45, and 60 MWd/kgU of the standard uranium dioxide fuel and the same procedure was repeated with the composite UO_2 + 10 vol.% SiC fuel.

The initial and boundary conditions are partially derived from the PSB model (mainly the geometric and thermal characteristics of the fuel pin) and from the FEMAXI one pellet model which was validated in subchapter 6.3.

6.6.1 Initial conditions

In order to be consistent with the PSB model, the fuel pin subjected to accident has been modelled as consisting from 14 axial segments of fuel column. Except for the most upper one, all axial segments have an identical length of 255 mm. The most upper one is 215 mm long. In common, the fuel column is 3530 mm height. Upper plenum volume was calculated to be 10 cm^3. No lower plenum volume was modeled since this volume is used to be negligibly small compared to the upper plenum volume. The pellet and cladding diameters were identical to that defined in the modified PSB model (see subchapter 6.3).

The fuel pellets were modelled as single cylinders without dishes, holes, and chamfers and of average height of 10 mm. The theoretical density used was 95 %. The cladding material was assumed in the stress relieved state. Pure helium was assumed as the gas filler with filling pressure of 2 MPa.

As mentioned above, there are five burnup stages at which the accident response is simulated (0, 15, 30, 45, and 60 MWd/kgU). In order to reach the fuel state at this burnup, a preconditioning phase had to be carried out before the accident. Table 6.5 provides the data after how many days is this burnup reached in the FEMAXI calculation and what is the equivalent burnup of the composite UO_2+SiC fuel. According this table, the fuel was operated before the accident was started.

After reaching the target burnup of the preconditioning phase, the accident scenario was defined by the temperature boundary conditions which are described in the following section 6.6.2.

The FA power after SCRAM depends mainly on the operational history [152], but the LHGR during the accident was also adopted from the PSB model.

Time (days)	**UO_2** (MWd/kgU)	**UO_2+SiC** (MWd/kgU)
1	0	1.0
317	15	16.1
633	30	32.2
949	45	48.3
1265	60	64.3

Tab. 6.5: Time needed to reach the target burnups of the preconditioning phases and the equivalent burnup of the composite UO_2 + SiC fuel

6.6.2 Boundary conditions

The boundary conditions used in the accident response simulations were defined by the cladding surface temperatures along the fuel pin. For each axial segment, a time dependent temperature vector has been generated. Using the conservative approach, each vector was calculated as the maximum temperature from temperature vectors generated from the 0, 15, 30, 45, and 60 MWd/kgU of UO_2 accident simulations at each time point. These temperature vectors were then used in all accident response simulations and thus unified conditions are assured. So, only the effects of the fuel response are assured to be observed. The time dependent vectors are presented in Figure 6.33.

During the development of the physical model of the accident response simulation, several changes were done compared to the single pellet model in subchapter 5.1. This was done because some bugs were found within the FEMAXI code which introduced numerical instabilities and had a strong influence on the results, especially on the cladding parameters.

In the FEMAXI accident response simulation, the cladding outer surface corrosion model had to be turned off because it introduced numerical instabilities into the whole calculation after closing the fuel cladding gap. Next issue was high temperature creep model. It was found that this model introduces numerical instabilities into the cladding deformation prediction yielding abrupt change in cladding radius and elongation. This problem was identified irrespective the cladding high temperature creep and deformation models used and thus the plasticity and creep of the cladding were ignored during the simulations. Consequently, the cladding mechanical behavior is the same in all cases regardless the irradiation time.

The fission gas release model has been changed as well. In the FEMAXI response simulation, the default FEMAXI6 settings of 0.5 % minimum FGR was not applied in order to investigate the FGR magnitude during the accident.

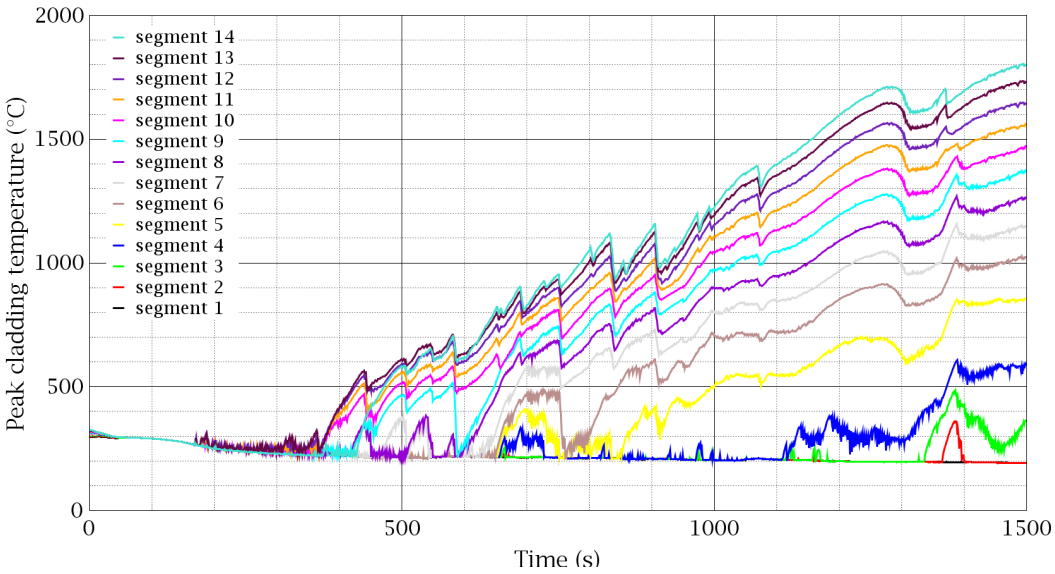

Fig. 6.33: The cladding surface temperature of axial segments used as the boundary condition in the accident simulation with the FEMAXI6 code

6.7 Results of the FEMAXI response simulation

In order to present calculation options of FEMAXI6 and for the sake of clarity, only the simulations at 0, 30, and 60 MWd/kgU were selected here as the representative cases of the accident response simulation. The results obtained from simulations at 15 and 45 MWd/kgU usually fall between the ranges obtained from the three other simulations.

Several parameters were selected in order to describe the behavior of the fuel during the accident and one can see the development of the selected parameters as a function of burnup. The selected parameters are depicted in the following figures starting from Figure 6.34. In cases where the parameter is related to the pellet properties (stresses, temperatures), the characteristics of the most upper 14^{th} axial segment of the simulated fuel pin are presented here because this segment is the most loaded from all of the segments.

Figure 6.34 denotes the development of the fuel centerline temperature. Here, the cladding surface temperature is plotted as well. All centerline temperatures follow the cladding surface temperature except for the beginning of the simulations when the centerline temperatures follow the decreasing LHGR. Due to the low LHGR after SCRAM, there is no significant difference in fuel centerline temperature between all cases. Noteworthy is the close development after the time of 400 s when the abrupt increase in temperature starts. Here, the centerline temperatures are very close to the cladding temperature but they are still above this temperature.

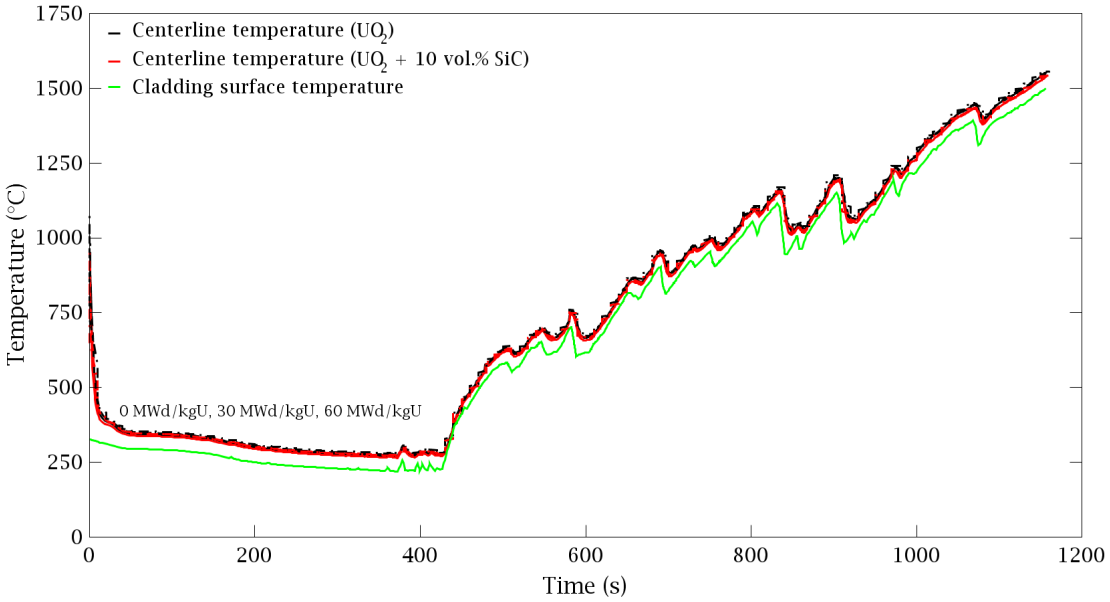

Fig. 6.34: Pellet centerline temperature in the most upper 14^{th} axial segment

The only exception are the temperatures of the fuel burned at of 60 MWd/kgU which seemingly undergo the cladding temperature. In reality, these temperatures are above the cladding surface temperature as well but the FEMAXI6 output file specifies the time data with insufficient accuracy for the case of such high burnup. This is because the FEMAXI6 is designed for solution of steady states. The time dependent heat conduction is not implicitly incorporated within the code.

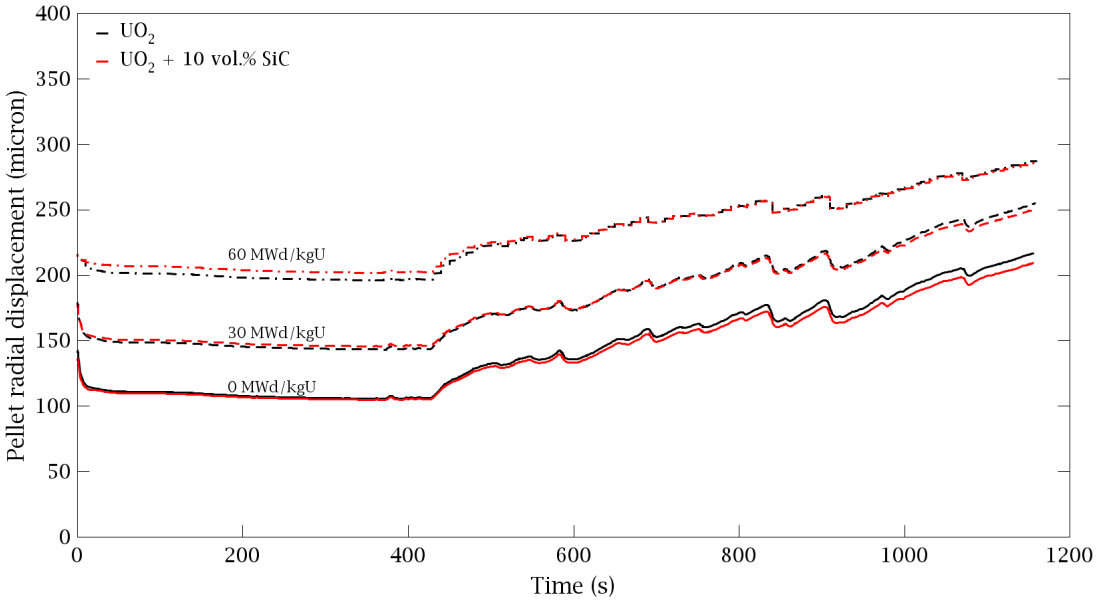

Fig. 6.35: Pellet radial displacement the most upper 14^{th} axial segment

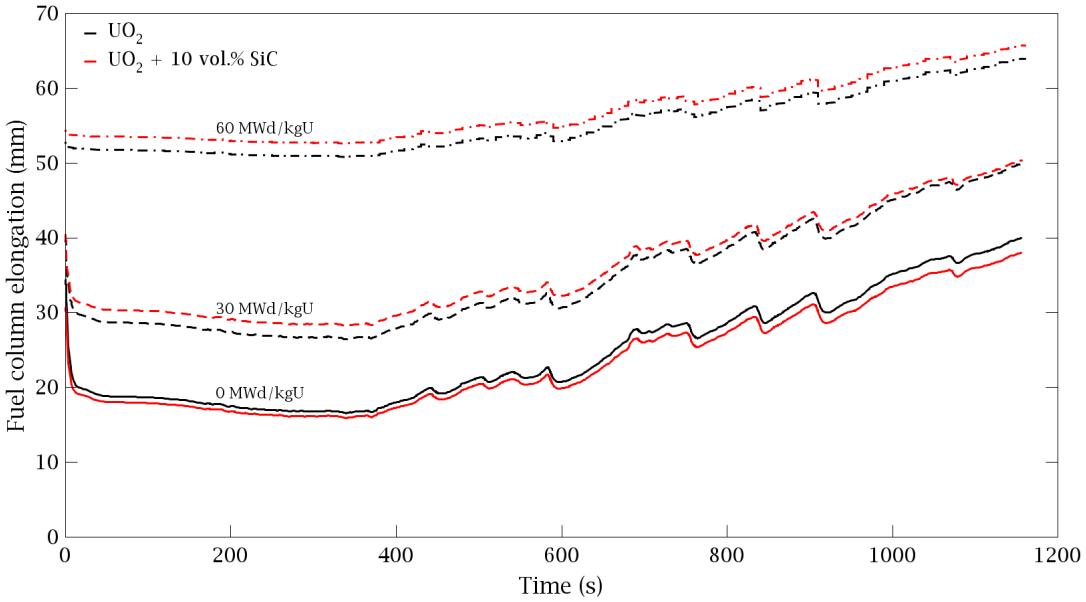

Fig. 6.36: Fuel column elongation during the accident

Another noteworthy fact is the end time of the accident. In Figure 6.33, the accident scenario is defined up to the time of 1500 s. Here, the simulation is terminated at the time of 1160 s. The reason for this is that FEMAXI6 allows to perform the calculations up to the cladding temperature of 1500 °C and this temperature is reached at this time. When this temperature is reached, the code terminates, probably due to the temperature limits of the implemented models.

The pellet radial displacement in Figure 6.35 and fuel column (axial) elongation in Figure 6.36 are found to have very similar development. For zero burnup and lower initial temperatures, the curves are very close to each other. For higher final temperatures, the curves diverge due to the different coefficient of thermal expansion of the fuels. For intermediate burnup and lower initial temperatures, the column elongation and pellet radial displacement of UO_2+SiC fuel is larger than that of UO_2 fuel. For higher final temperature, the difference between the observed parameters decreases as the UO_2 expands more. A the highest burnup and lower initial temperatures, the difference between the curves is even more pronounced but the consequent behavior of the parameters differs. The pellet radial displacement is identical in behavior after the temperature increase after 400 s. This is the consequence of restricting influence of cladding for which only the thermal expansion model applies (the models of plasticity and creep were turned off). Due to the lack of these models, the cladding response to the accident conditions is very similar regardless the burnup - see Figure 6.37. The fuel column elongation is found to be identical but shifted along the y-axis.

The gap width development is depicted in Figure 6.38. The initial gap width in the beginning of the accident widens as the fuel power decreases. With increasing burnup, the pellet swelling causes the gap to decrease. In the case that the gap remains open in the final state, the final gap with is smaller for the UO_2 fuel instance.

A detail analysis of Figure 6.39 reveals that the plenum volume change becomes less sensitive to the temperature change as the burnup increases. At zero burnup, the plenum volume decreases with increasing temperature especially in the case of UO_2. From all the cases, the fuel column elongation and fuel gap closure are the most sensitive to the increased temperature. On the other hand, the plenum volume is insensitive to the temperature increase at the highest burnup. The fuel gap is small compared to other cases and the expanding fuel column is compensated for by the increasing cladding inner diameter. This combined effect remains the plenum volume at a constant value.

The plenum pressure (Figure 6.40) is derived from the behavior of the plenum volume and fission gas release. In the accident response simulation, the fission gas release model was not conditioned by the condition of minimum FGR of 0.5 % as in the case of the FEMAXI sensitivity study. Therefore, the FGR here is smaller and the magnitudes of plenum pressure at 0 and 30 MWd/kgU reflect only the decrease in the plenum volume. At 60 MWd/kgU, the FGR becomes substantial and, for this reason, there is a big difference between the final values.

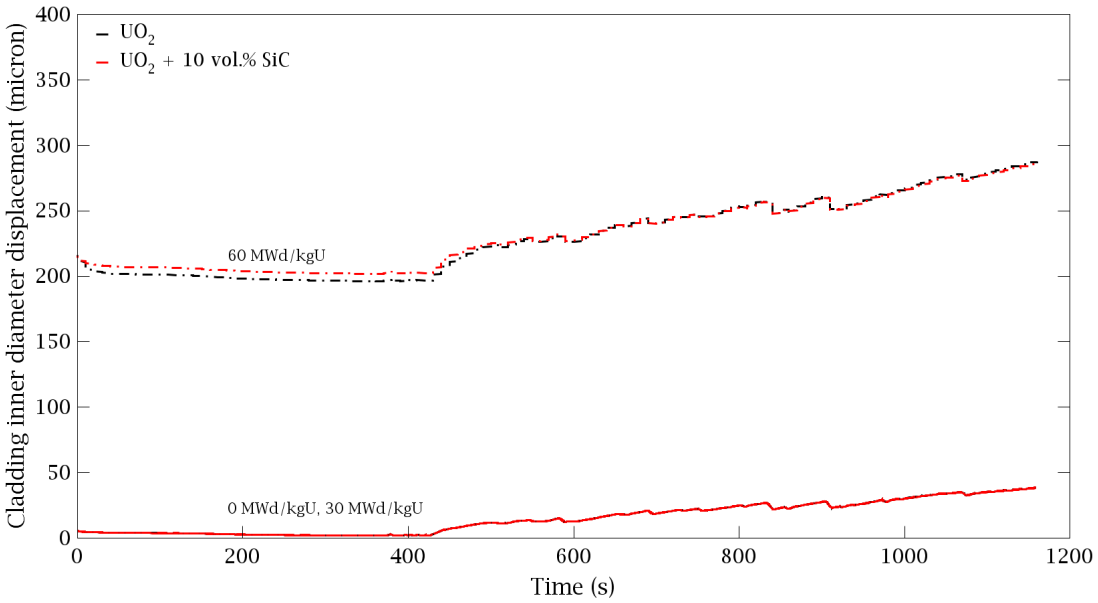

Fig. 6.37: Cladding inner diameter displacement evolution during the accident

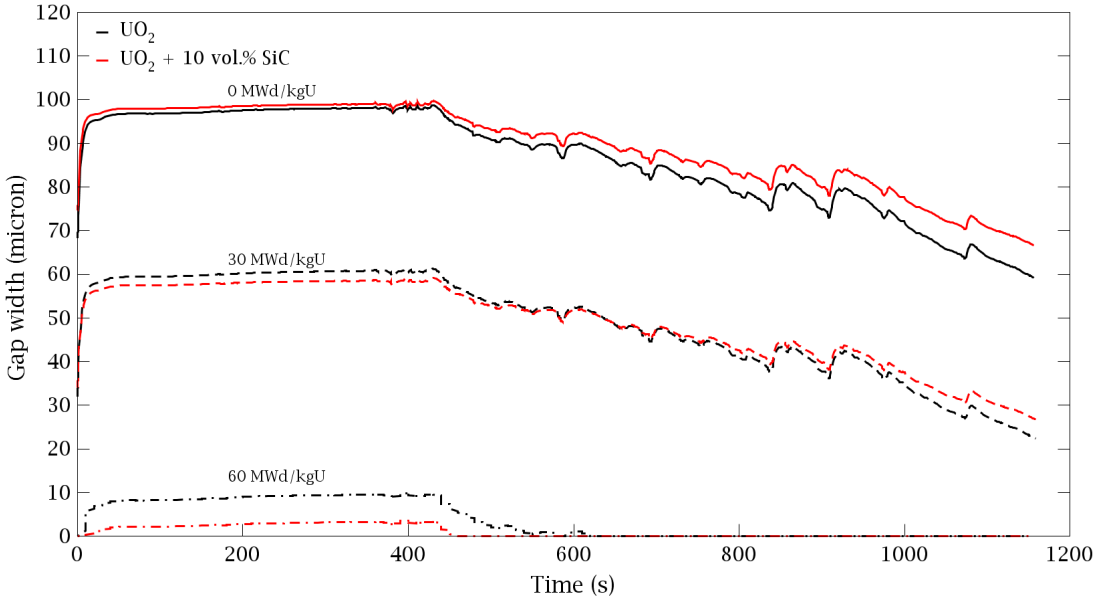

Fig. 6.38: Gap width evolution during the accident

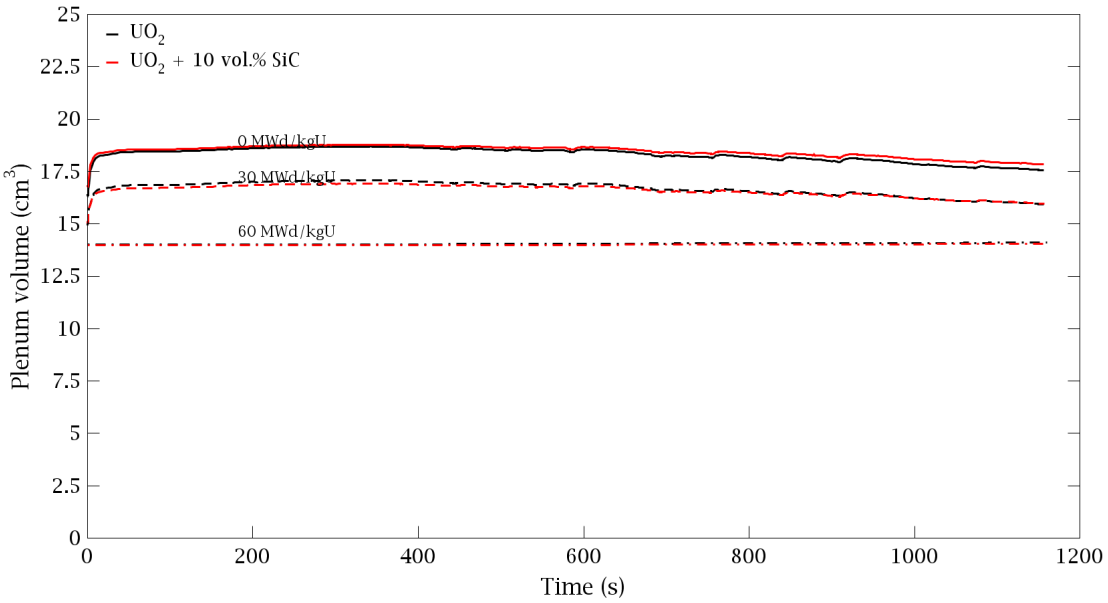

Fig. 6.39: Plenum volume evolution during the accident

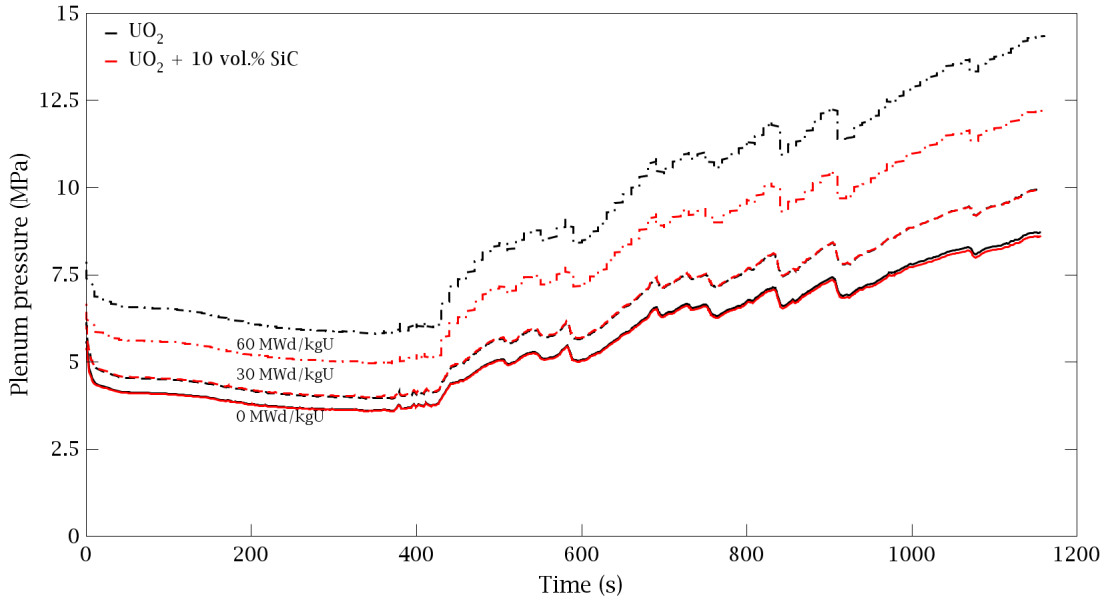

Fig. 6.40: Plenum pressure evolution during the accident

FEMAXI6 allows to calculate internal stresses within the pellet as well. Figures 6.41 - 6.43 show the axial, circumferential, and radial stresses evolution during the accident. Figure 6.44 then shows the equivalent stress which takes into account all three measures. In all cases, the UO_2 fuel is subjected to the same of higher stresses than the UO_2 + SiC fuel. However, due to the low residual power of the fuel representing the decay heat, the stresses are small compared to normal operation conditions.

In the cases of 0 and 30 MWd/kgU, there is no influence of the increasing temperature on the stresses. This is valid except for the abrupt change in temperature during the transition from cooling to heat up. It appears that the bigger preceding temperature decrease, the bigger stress peak is predicted. Moreover, this phenomenon is not observed for the transition from heat up to cooling and this effect is pronounced with higher burnup. It is a question whether this is a numerical instability or real behavior. In general, this fuel code behavior is attributed to the fact that the code is not intended for time dependent (transient) analysis. The code arrives at the solution considering the task as the series of steady states.

In the cases of 60 MWd/kgU burnup, there is a clear cladding influence on the fuel stress behavior. As the fuel expands, the cladding works in the opposite direction giving rise to negative trends in stresses. For this burnup, the stresses of the composite UO_2 + SiC fuel are lower compared to the standard UO_2 except for the case of pellet circumferential stress which is comparable.

Nevertheless the Figure 6.44 shows, that the fuels behave in very similar way and the SiC influence is low.

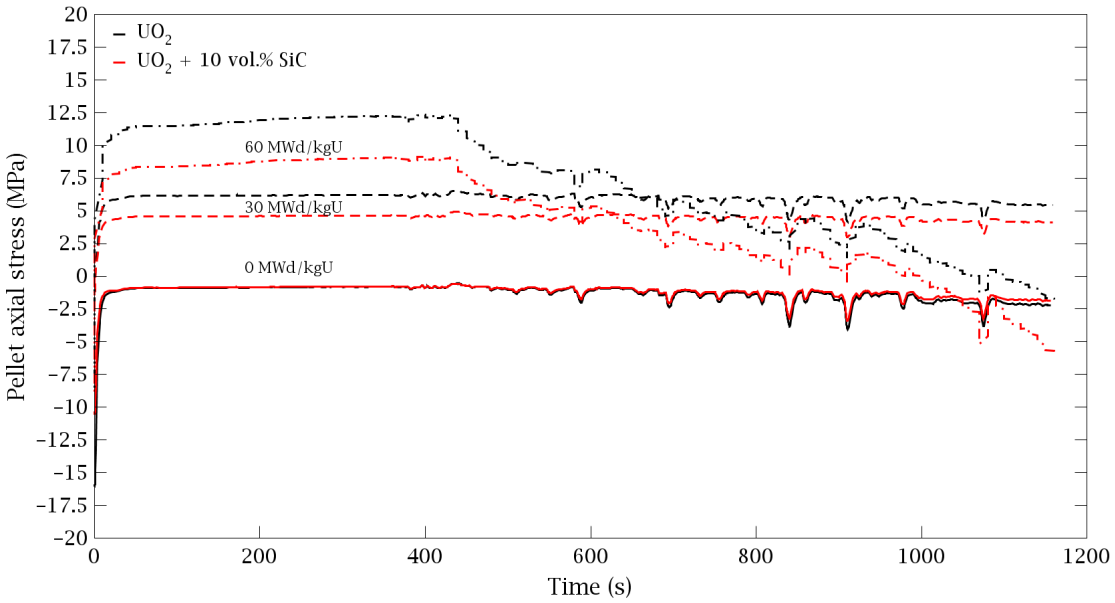

Fig. 6.41: Pellet axial stress

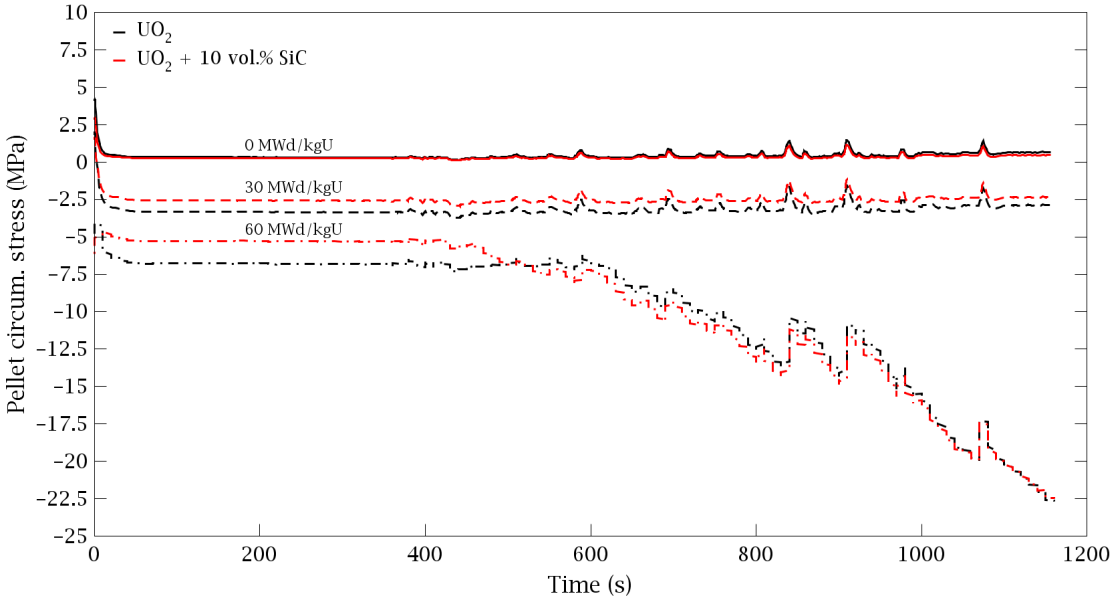

Fig. 6.42: Pellet circumferential stress

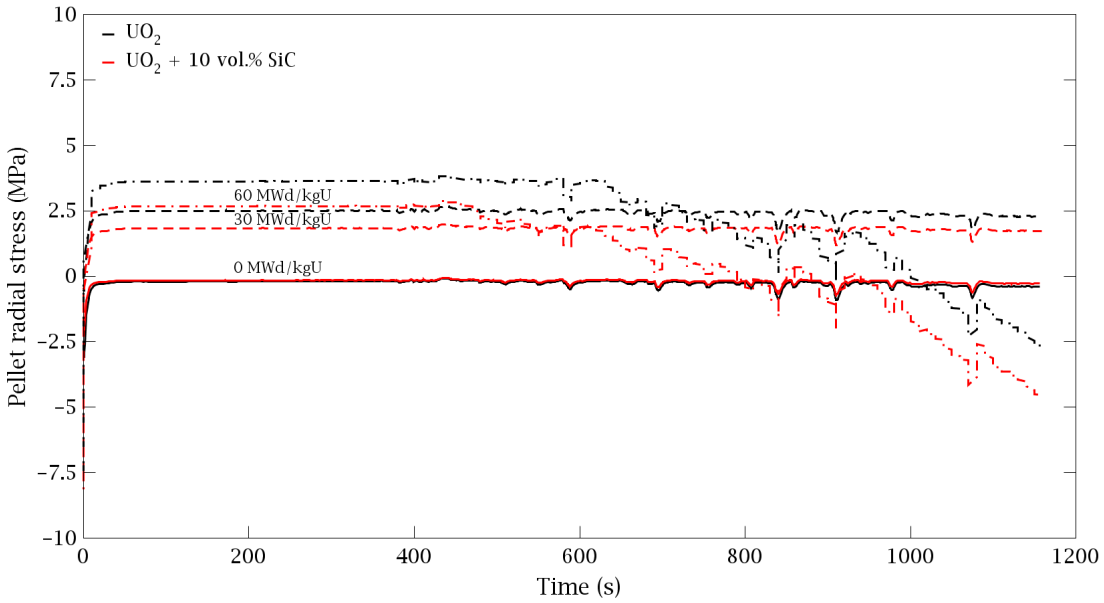

Fig. 6.43: Pellet radial stress

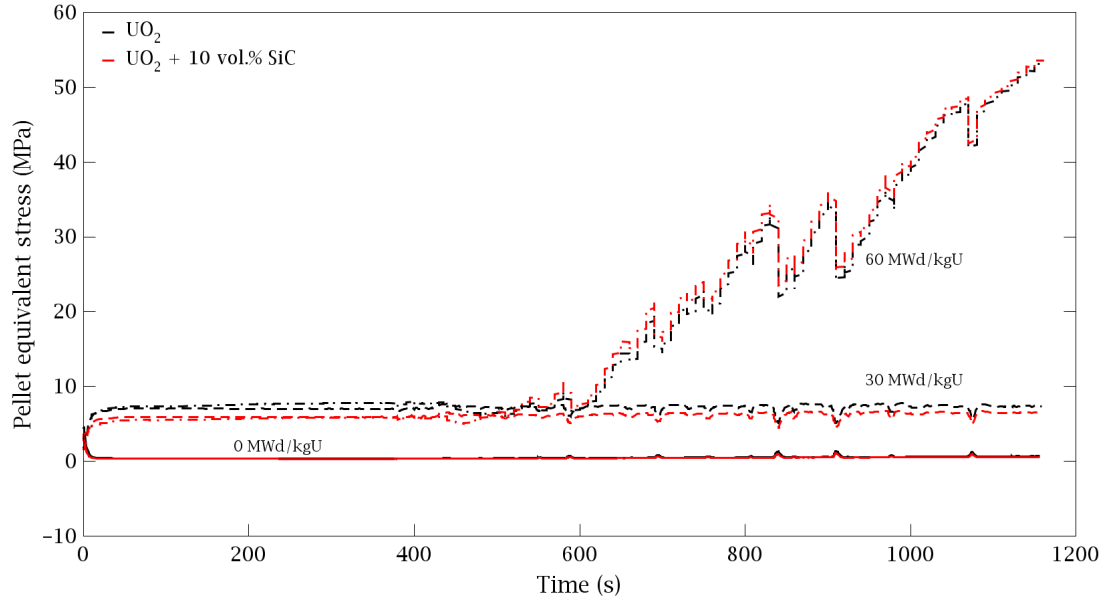

Fig. 6.44: Pellet equivalent stress

7 RIA analysis of the composite nuclear fuel

7.1 Performance of the fuel during RIA

A Reactivity Initiated/Inserted Accident of PWR is a kind of accident that involves fast ejection of the control rod from the core by mechanical failure of the control rod mechanism. As a result, a fast pulse in fission rate is generated. Since there is a direct relation between the neutron flux and heat generation, the sudden increase in neutron multiplication results in higher heat generation rate. The RIA accident may result in failure of fuel pins and the pin content may be released within the primary circuit [153].

The fuel pellet response to the RIA conditions is explained using the analysis of FK-10 and FK-12 experiments presented in [154]. These experiments were performed in the Nuclear research safety reactor located in Japan and their analysis results are illustrated in Figures 7.1 and 7.2. In these experiments, fuel rods were subjected to RIA conditions in cold phase of the startup of the reactor.

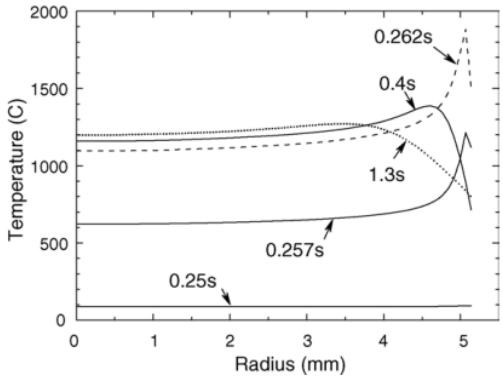

Fig. 7.1: *Calculated temperature profile in the radial direction of pellet at five instants in the FK-10 experiment* [154].

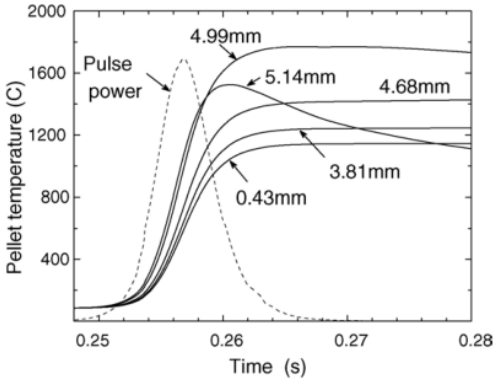

Fig. 7.2: *Pulse power (relative) and calculated pellet temperature change in five radial locations (ring elements) in the FK-10 experiment* [154].

Within the initial stage of RIA accident, there is a dominant impact on the fuel temperature profile. The initial parabolic temperature profile takes the shape depicted in Figure 7.1 where heat generation dominates on the fuel pellet periphery. The temperature profile basically corresponds to the heat generation profile during normal steady state where the fission density is the highest on the fuel pellet periphery as well due to the close neighborhood of the moderator (the self-shielding effect).

From the point of view of temperature time dependence, one can see from Figure 7.2 that the fuel pellet periphery heats up instantaneously and the heat up process of the fuel center is slightly slower. The time relation with heat up pulse is shown in this figure as well and one can also see from this figure that the power pulse is very short and sharp. With increasing time, the heat is very quickly exported from the fuel pellet. This is very illustratively depicted by the 5.14 mm line which represents the most outer radial location of the fuel pellet.

As a result of the heat pulse, the fuel pellet expands, gets in contact with cladding and thus is loaded by mechanical stresses resulting from PCMI and by cooling of the pellet surface. From the point of UO_2 solely, there is a risk of pellet fragmentation. The limit imposed on fragmentation varies between 200-280 cal/g (837-1172 J/g) in the case of VVER technology. However, this limit is very high and is not expected to occur. In some countries, another limit is imposed on the fuel failure which also considers the cladding failure. This value is typically much smaller compared to first limit. For example, in the Czech Republic, the allowable enthalpy rise is 140 cal/g (586 J/g) [155, 156].

In both cases, the fuel enthalpy is the main parameter. It can be expressed in the form of radially averaged fuel enthalpy increase for the first limit mainly or in the form of enthalpy rise or increase in the second limit.

7.2 Influence of selected parameters on RIA management and fuel behavior

Impact of selected parameters on the RIA accident consequences is considered mainly from the point of view of fuel temperature. Reference [153] provides a large discussion of the parameters having influence on the RIA management but only some of them will be discussed here. This reference is used as the main source of information in this subchapter. The thermal fuel behavior during RIA accident is complicated phenomenon difficult to predict since there are many parameters competing against each other. This subchapter tries to give a theoretical background for the analysis given within the next subchapter 7.3.

The influence of increased heat capacity on the fuel enthalpy or fuel temperature during RIA should be small. Calculations performed by PARCS (Purdue Advanced Reactor Core Simulator) for the EOC conditions by TMI-1 reactor show that increase in fuel heat capacity by 20% lead to increase in fuel centerline temperature by 10 °C.

The burnup effect on the temperature peak position is important. *In a fresh fuel rod, the fissile material consists predominantly of U-235, which is usually uniformly*

distributed in the fuel pellets. Hence, both power and fission products are generated with a relatively small variation along the fuel pellet radius. However, with increasing burnup, there is a non-uniform build-up of fissile plutonium isotopes through neutron capture by U-238 and formation of Pu-239 and heavier fissile isotopes of plutonium. Since the neutron capture takes place mainly at the pellet surface, the distributions of fissile material, fission rate and fission products will develop marked peaks at the pellet surface as fuel burnup increases. The highest temperatures are occurring at the fuel pellet periphery [157].

The thermal conductivity plays an important role in the RIA accident management. First of all, the influence of the fuel thermal conductivity degradation due to the burnup on fuel behavior needs further research. It can be expected, that burnup will have negative effect on the RIA management. As the fuel is operated in the core and the burnup increases, the thermal conductivity decreases and so prevents the accumulated heat from RIA accident to be transferred from the fuel pellet to the coolant. But most importantly, during RIA accident, there is a significant risk of boiling crisis occurrence and the thermal conductivity may have influence on this phenomenon. The boiling crisis prevents the heat from escaping the fuel pin to the coolant and *It has been found that boiling crisis are suppressed or delayed, when radial heat transfer is hindered by, e.g. a large pellet-clad gap or a thick layer of oxide at the cladding surface* [153]. Thus, one can expect that by increasing the thermal conductivity, the boiling crisis is promoted.

The pellet-clad contact and bonding are of big importance as well. During burnup, the fuel swells and thus gets in contact with cladding as discussed in the chapter dedicated to FEMAXI calculations. For high burnups, the fuel and cladding bond (weld together). The formation of bonding promotes further heat transfer from fuel pellet to cladding and coolant.

As a side note, the influence of FGR is mentioned here from the point of view of cladding behavior. The increased fuel thermal conductivity decreases the FGR and the plenum pressure. A lot of experimental work has been done to investigate the ballooning and cladding failure during RIA. Since balooning is in direct relation with plenum pressure, it is mentioned here as well. But as mentioned previously, further research is needed in FGR behavior of the composite UO_2+SiC fuel.

The risk of fuel melting is identified for the RIA accident as well. The solidus of UO_2 is 3120 K but the presence of fission fragments decreases this value. The magnitude of depression is still under research. In this work, the reference temperature of 1700 °C is taken (as mentioned in section 2.2.2, the onset on chemical reaction between UO_2 and SiC is at 1370 °C and the system is completely molten above 1700 °C). Furthermore, one may expect that fission products will have similar influence on the melting temperature too.

7.3 RIA analysis of the composite nuclear fuel

The RIA analysis has been performed using the TRANSURANUS code which is well established for this type of analysis. The analysis was performed in cooperation with the NRC Rez. Special thanks go to Vitezslav Matocha for his very kind help with this work. The author has provided him with input data on important fuel parameters. He implemented them into the TRANSURANUS code and performed the calculations. Some aspects of the calculations are performed using the "good practice" of the NRC Rez and thus they are not published here.

For the RIA analysis, similar conditions as in the FEMAXI analysis were set up. In order to reach the fuel properties corresponding to the desired burnup, the preconditioning phase was simulated here at first as well. The LHGR was of 20 kW/m but since the full-scale model was used, the LHGR axial distribution had to be considered. The fuel has been irradiated to the target burnup and after that RIA accident was simulated. The only exception from this was the analyzis for the zero burnup where the fuel assembly was kept in the hot zero state for 20 hours at 280 °C and 15.7 MPa. The analyzed fuel assembly was of the TVSA-T type. Selection of this type of fuel is explained in the subchapter 6.3.

In the analysis, the fuel column was divided into 24 segments along the height. A nodalization along the radii was performed as well. The fuel pellet was divided into 8 zones in the radial direction and 88 measurement points were defined within the zones in total. The cladding was divided into 4 zones in the radial direction and 17 measurement points were defined within the zones.

The power pulse resulting from withdrawal of the control rod bank is depicted in Figure 7.3. This power pulse was used in all cases as the boundary condition. The control rod withdrawal was assumed to happen within 0.1 seconds when the control rod bank is ejected from the core bottom to its uppermost position.

From the neutronic point of view, the power pulse shape of the for the composite UO_2 + SiC should be different from that of the standard UO_2 fuel. But for example, it was found in [158] that the power pulse during RIA accident of the U_3Si_2 fuel is almost the same as for the UO_2 fuel. So, the simplification may not be crucial.

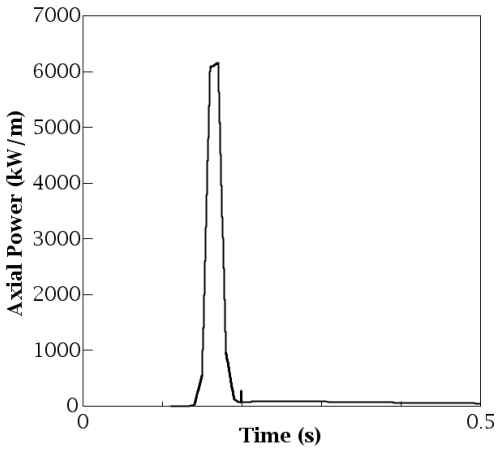

Fig. 7.3: The power pulse used in the RIA accident simulation

The rest of the work is considered as confidential. For this reason, the detail results of the work are not presented in this open version of the dissertation thesis.

8 Conclusion

This thesis deals with composite nuclear fuels, its properties, modelling of the properties with special focus on the thermal conductivity. The main findings of the work are summarized in the following points:

- Different mathematical models were developed tghrouhout the history for predicting the thermal conductivity of composite materials. The main models and accompanying theory are introduced here. It was found that the widely used Hasselman model is suitable for composite whose constituents do not have the difference in thermal conductivity higher than two orders (typically UO_2 and SiC). For composites with higher difference in thermal conductivity (UO_2 + diamonds, for example), the Geometry mean model seems to be perspective. However, due to the uncertainity in experimental data, this assumption cannot be confirmed.
- There is a need in developing thermal conductivity models for composites containing highly conductive additives in the form cylinders . The Miranda model, which seemed to be perspective in this area, fails in prediction of the thermal conductivity of the UO_2+SWCNT composite fuel. On the other hand, it must be noted that this kind of fuel poses non-standard behaviour due to the unclear physical effects. Therefore, the experimental data on thermal conductivity of this fuel should be considered with caution.
- Following additives are introduced as candidate materials for intrusion into the UO_2 matrix: BeO, SWCNT, SiC and Diamonds. From the point of view toxicity, the BeO poses high toxicity and carcinogenic risk. Other materials should be non-toxic (at least at the level of the current knowledge). For this reason, the BeO was excluded from the selection. On the other hand, the composite UO_2+BeO has been already loaded to a material test reactor so there is a (potential) chance for further research in this area. Diamonds provide the best bulk thermal conductivity, but they pose the risk of graphitization. The question of thermal conductivity of comnpoiste fuel UO_2+SWCNT remains unresolved but there is a very risk of the reaction between UO_2 and carbon forming UC. The SiC pose not so good neutronic properties compared to other materials but it is a non-toxic material which properties under neutron irradiation are well investigated. For this reason, this material was selected as additive for further detail analysis of the composite fuel behaviour. The UO_2+SiC composite fuel was subjected to computational analysis using FEMAXI-6 and RELAP5/MOD3.3 codes.

- The FEMAXI-6 code has been modified in such a way that the influence of SiC additive on the general fuel behaviour could have been taken into account. The analysis using the this code predicts improved operational characteristic, especially lower fuel centerline temperature resulting in lower fission gas release and lower plenum pressure. The mechanical loading of the fuel should be decreased by the presence of SiC as well. On the other hand, the influnce of the different structure of the composite fuel on the FGR and long term fuel matrix stability is unclear. It is not clear wheather the additional porosity will increase or decrease the FGR and wheather the contact between UO_2 matrix and SiC grains will remains good during burnup or the grains will debond from the matrix. Both the phenomena are a big issues and they are crucial for further analysis.
- For more detail analysis, the UO_2 + 10 %vol. SiC concept of accident tolerant fuel was selected. The thermo-mechanical behaviour during normal operation, LOCA-like accident and RIA accident was of the main interest. The neutronic properties of this type of fuel were out of the scope of this work but a basic analysis was performed using the UWB code tohether with other candidate materials.
- The LOCA-type analysis has been performed using the combination of the RELAP5/MOD3.3 and FEMAXI-6 code. The RELAP5 model of the PSB VVER 1000 facility was used to generate the boundary conditions of accident which is characterised by slow increase in cladding temperature above 1200 °C and minimal LHGR representing the decay heat generation within the fuel. The data was then used as input for the analysis performed by the FEMAXI-6 code. The analysis reveals that the fuel containing SiC poses lower internal stresses and slightly lower fuel centerline temperature. Thus, it was found that the SiC addition improves the behaviour of the fuel during the accident and there is a potential for mitigation of the accident consequences.
- The RIA accident analysis using the TRANSURANUS indicates that the composite UO_2 + 10 vol.% SiC fuel poses strongly negative behaviour during this type of accident. The composite fuel temperature exceeded the lowest reported temperature of the composite melting. This could lead to cladding damage and release of radioactive material into the primary circuit. Moreover, this would be supported by degraded cladding material due to the enhanced boiling crisis. The RIA analysis predicts higher cladding temperature of the composite fuel compared to the standard UO_2 fuel. This is the next negative phenomenon which needs to be investigated by all types of accident tolerant fuel with enhanced thermal conductivity and/or enhanced specific heat due to the presence of additive.

All the above mentioned findings should be considered as the first-assessment conclusion. The topic of accident tolerant fuels is very complex and addition of second phase into the standard fuel needs a large research in the material field which serves then as the basis for nuclear modelling. Moreover, the experimental database on fuel behaviour during burnup is the most significant in this field but here, the research is still in the very early phase.

List of symbols, physical constants and abbreviations

Abbreviations

CCFL	Counter current flow limitation
CVC	Chemical vapor composited
CVD	Chemical vapor deposited
ECC	Emergency core cooling
ECCS	Emergency core cooling system
EMT	Effective medium theory
LOCA	Loss of coolant accident
LANL	Los Alamos National Laboratory
LWR	Light water reactor
NRC	Nuclear regulatory commission
PWR	Pressurized water reactor
ORNL	Oak Ridge National Laboratory
REA	Rod ejection accident
RIA	Rod injection accident
SCRAM	safety control rod axe man
SWCNT	Single wall carbon nanotube
SPS	Spark plasma sintering
TCC	Thermal conductivity of composites
TRISO	Tristructural-isotropic fuel
UP	Upper plenum
WWER	Water-water energetic reactor

Symbols and physical constants

A	Phonon scattering cross section parameter
a	Radius of the second phase particle
a_k	Kapitza resistance
B	Temperature dependent term in phonon mean free path calculation
Bu	Burnup
CF	Correlation factor
CTE	Coefficient of thermal expansion
c	Specific heat

D	Fractional theoretical density
E	Young's modullus
$EFPY$	Effective full power year
F	Fluence
F	Shape factor
FGR	Fission gas release
FOM	Figure of merit
f	Volumetric share
f	Thermal utilization factor
$Gdcon$	Weight fraction of gadolinia
h_c	Interfacial thermal conductance
K_{BeO}	Technological factor
k	Thermal conductivity
k_∞	Infinite multiplication factor
L	Length
$LHGR$	Linear heat generation rate
M	Gram formula weight
MEM	Mean error magnitude
N	Avogadros's number
O	Observed point
P	Porosity
P	Predicted point
PP	Plenum pressure
p	Resonance escape probability
Q	Generated heat
q_l	Linear heat generation rate
R	Resistance
$RIHFC$	Relative Integrated Heat Flux to the Coolant
r	Pellet radius
SE	Stored energy
T	Temperature
t	Temperature
TD	Theoretical density
u	Phonon velocity
V	Volumetric share of the additive
X	Shape factor

Superscripts and subscripts

0	Initial
1	Dispersed phase
2	Continuous phase
95	At 95 theoretical density
273	At 273 K
c	Coating
c	Continuous model
cr	Chemical reaction
e	Electron
eff	Effective
irr	Irradiation
kap	Kapitza
l	Longitudal direction
m	Matrix
max	Maximal
min	Minimal
$non-irr$	Non-irradiated
p	At constant pressure
p	Parallel model
p	Particle
p	Phonon
r	Radial
rd	Radiation damage (Thermal defect)
$room$	Room
t	Transverse direction
u	Outer radius
v	Constant volume
z	Axial
θ	Tangential
$\parallel$	In axial direction
$\perp$	In radial direction
$f(\perp, \parallel)$	Fiber (in axial and parallel direction)

Greek symbols

α	Thermal expansion coefficient
α	Angle between the revolution axis of the spheroid and the non perturbed heat flux
α_1	Correction term on relative thickness of coating in axial direction
α_3	Correction term on relative thickness of coating in radial direction
β_1	Thermal conductivity ratio
β_2	Thermal conductivity ratio
δ	Thickness of coating
ϵ	Fast fission factor
ϵ^{tot}	Pellet total strain
ϵ^{therm}	Pellet thermal expansion strain
ϵ^{reloc}	Pellet relocation strain
ϵ^{crack}	Pellet crack strain
ϵ^{densf}	Pellet densification strain
ϵ^{swell}	Pellet swelling strain
$\epsilon^{hot-press}$	Pellet hot press strain
ϵ^{ps}	Pellet plasticity strain
ϵ^{creep}	Pellet creep strain
η	Reproduction factor
λ	Thermal conductivity
λ	Phonon mean free path
ν	Relative fraction of second phase to coating
ν	Phonon velocity
ν	Poisson's ratio
ρ	Density
σ	Stress
χ	Electron-phonon coupling factor

Bibliography

[1] H. Druenne and J. Zhang W.V. Hove. Safety and reliability - Fuel Rod Design. Lecture given within the BNEN course, SCK.CEN, February 2015.

[2] D.R. Olander. Fundamental aspects of nuclear reactor fuel elements. Technical report 1, California Univ., Berkeley (USA). Dept. of Nuclear Engineering, California, January 1976. URL: https://www.osti.gov/biblio/7343826-fundamental-aspects-nuclear-reactor-fuel-elements.

[3] Bedrich Hermansky. *Termomechanika jadernych reaktoru*. Academia, -, 1986.

[4] W. Wiesenak. Fuel temperature modeling and phenomena:pellet-clad gap heat transfer, fuel temperature distribution. On the WWW, April 2010. URL: http://indico.ictp.it/event/a09140/session/73/contribution/50/material/0/1.pdf.

[5] E.J. Lahoda, Lars Hallstadius, Frank Boylan, and Sumit Ray. What should be the Objective of Accident Tolerant Fuel? *TRANSACTIONS of the AMERICAN NUCLEAR SOCIETY*, 110:733–736, 2014.

[6] S.M. Bragg-Sitton, Jon Carmack, F.J. Goldner, and S.L. Hayes. Status update on U.S. DOE Accident Tolerant Fuel? *TRANSACTIONS of the AMERICAN NUCLEAR SOCIETY*, 110:727–733, 2014.

[7] Jon Carmack. Update on U.S. Accident Tolerant Fuel Program. On the WWW, February 2016. URL: https://www.nrc.gov/reading-rm/doc-collections/commission/slides/2016/20160620/carmack-20160620.pdf.

[8] Kurt A. Terrani, Dean Wang, Larry J. Ott, and Robert O. Montgomery. The effect of fuel thermal conductivity on the behavior of LWR cores during loss-of-coolant accidents. *Journal of Nuclear Materials*, 448(1):512 – 519, 2014. URL: http://www.sciencedirect.com/science/article/pii/S0022311513011288, doi:https://doi.org/10.1016/j.jnucmat.2013.09.051.

[9] H. Shimizu. The properties and irradiation behavior of U_3Si_2. Final report NAA-SR-10621, Atomics International - A division of north american aviation, inc., May 1965.

[10] Luis Ortega, Brandon J. Blamer, Jordan A. Evans, and Sean McDeavitt. Development of an accident-tolerant fuel composite from uranium mononitride

(un) and uranium sesquisilicide (u_3si_2) with increased uranium loading. *Journal of Nuclear Materials*, 471(–):116–121, January 2016.

[11] N.R. Brown, M. Todosow, L-Y Cheng, and A. Cuadra. Screening of reactor performance and safety of fuel and cladding candidates with enhanced accident tolerance. In *TopFuel 2015 - Conference Proceedings*, volume **1**, pages 10–20, Brussels, Belgium, September 2015. European Nuclear Society. ISBN 978-92-95064-23-2.

[12] Kurt A. Terrani. Accident tolerant fuel cladding development: Promise, status, and challenges. *Journal of Nuclear Materials*, 501:13 – 30, 2018. URL: http://www.sciencedirect.com/science/article/pii/S0022311517316227, doi:https://doi.org/10.1016/j.jnucmat.2017.12.043.

[13] Jeremy Bischoff, Christine Delafoy, Christine Vauglin, Pierre Barberis, Cedric Roubeyrie, Delphine Perche, Dominique Duthoo, Frederic Schuster, Jean-Christophe Brachet, Elmar W. Schweitzer, and Kiran Nimishakavi. Areva np's enhanced accident-tolerant fuel developments: Focus on cr-coated m5 cladding. *Nuclear Engineering and Technology*, 2018. URL: http://www.sciencedirect.com/science/article/pii/S1738573317307945, doi:https://doi.org/10.1016/j.net.2017.12.004.

[14] Foral. Personal communication with R. Skoda. –, October 2017.

[15] James Braun, Christine Gueneau, Thierry Alpettaz, Cedric Sauder, Emmanuelle Brackx, Renaud Domenger, Stephane Gosse, and Fanny Balbaud-Celerier. Chemical compatibility between UO_2 fuel and SiC cladding for LWRs application to ATF (Accident-Tolerant Fuels). *Journal of Nuclear Materials*, 487:380 – 395, 2017. URL: http://www.sciencedirect.com/science/article/pii/S0022311516310133, doi:https://doi.org/10.1016/j.jnucmat.2017.02.031.

[16] R. C. Progelhof, J. L. Throne, and R. R. Ruetsch. Methods for predicting the thermal conductivity of composite systems:a review. *Polymer Engineering & Science*, 16(9):615–625, 1976. URL: http://dx.doi.org/10.1002/pen.760160905, doi:10.1002/pen.760160905.

[17] Jianfeng Wang, J. K. Carson, M. F. North, and D. J. Cleland. A new approach to modelling the effective thermal conductivity of heterogeneous materials. *International Journal of Heat and Mass Transfer*, 49(17-18):3075–3083, 2006.

[18] J. K. Carson, S. J. Lovatt, D. J. Tanner, and A. C. Cleland. Thermal conductivity bounds for isotropic, porous materials. *International Journal of Heat and Mass Transfer*, 48(11):2150–158, 2005.

[19] A. E. Powers. Conductivity in Aggregates. Progress report JCAPL-2145, Knolls Atomic Power Lab, -, March 1961.

[20] J. V. Miller. Estimating thermal conductivity of cermet fuel materials for nuclear reactor application. NASA technical note NASA TND-3898, Lewis Research Center, Cleveland, Ohio, April 1967. URL: `https://ntrs.nasa.gov/archive/nasa/casi.ntrs.nasa.gov/19670013537.pdf`.

[21] F. Cernuschi, S. Ahmaniemi, P. Vuoristo, and T. Mantyla. Modelling of thermal conductivity of porous materials: application to thick thermal barrier coatings. *Journal of the European Ceramic Society*, 24(9):2657 – 2667, 2004.

[22] Jianfeng Wang, J. K. Carson, M. F. North, and D. J. Cleland. A new structural model of effective thermal conductivity for heterogeneous materials with co–continuous phases. *International Journal of Heat and Mass Transfer*, 51(9–10):2389–2397, 2008.

[23] D. P. H. Hasselman and Lloyd F. Johnson. Effective Thermal Conductivity of Composites with Interfacial Thermal Barrier Resistance. *Journal of Composite Materials*, 21:508–515, June 1987.

[24] Ce-Wen Nan. Effective-medium Theory of Piezoelectric Composites. *Journal of Applied Physics*, 76(2):1155–1163, July 1994.

[25] S. Yeo, R. Baney, G. Subhash, and J. Tulenko. The influence of SiC particle size and volume fraction on the thermal conductivity of spark plasma sintered UO_2 - SiC composites. *Journal of Nuclear Materials*, 442(1–3):245–252, November 2013.

[26] E. T. Swartz and R. O. Pohl. Thermal boundary resistance. *Reviews or Modern Physics*, 61(3):605–668, July 1989.

[27] Xuebing Liang, Chengchang Jia, Ke Chu, and Hui Chen. Predicted Interfacial Thermal Conductance and Thermal Conductivity of Diamond/Al Composites with Various Interfacial Coatings. *Rare Metals*, 30(5):544–549, October 2011.

[28] Ce-Wen Nan, G. Liu, Y. Lin, and M. Li. Interface effect on thermal conductivity of carbon nanotube composites. *Applied Physics Letters*, 85(16):–, October 2004.

[29] J. Zhao, F. Du, W. Cui, P. Zhu, X. Zhou, and X. Xie. Effect of silica coating thickness on the thermal conductivity of polyurethane/sio2 coated multiwalled carbon nanotube composites. *Composites Part A: Applied Science and Manufacturing*, 58:1 – 6, 2014. URL: http://www.sciencedirect.com/science/article/pii/S1359835X13003175, doi:http://dx.doi.org/10.1016/j.compositesa.2013.11.008.

[30] Hyungu Im and Jooheon Kim. Thermal conductivity of a graphene oxide-carbon nanotube hybrid/epoxy composite. *Carbon*, 50(15):5429 – 5440, 2012. URL: http://www.sciencedirect.com/science/article/pii/S0008622312006240, doi:http://dx.doi.org/10.1016/j.carbon.2012.07.029.

[31] J. Ordonez-Miranda, J. J. Alvarado-Gil, and R. Yang. Effective thermal conductivity of metal-dielectric composites at the non-dilute limit. *International Journal of Thermophysics*, 33(10):2118–2124, Novemeber 2012.

[32] Eric D. Felder. Heat conduction analysis of randomly dispersed single-walled carbon nanotubes. MS Thesis, Naval postgraduate school, Monterey, CA 93943, June 2007. -.

[33] Jianwei Che, Tahir Cagin, and William A. Goddard. Thermal conductivity of carbon nanotubes. *Nanotechnology*, 11(–):65–69, 2000.

[34] YAN HE and YUANZHENG TANG. Thermal conductivity of carbon nanotube/natural rubber composite from molecular dynamics simulations. *Journal of Theoretical and Computational Chemistry*, 12(3):–, April 2013.

[35] J. Ordonez-Miranda and R. Yang. Effect of a metallic coating on the thermal conductivity of carbon nanofiber-dielectric matrix composites. *Composites Science and Technology*, 109:18–4, 2015. URL: http://www.sciencedirect.com/science/article/pii/S0266353815000329, doi:http://dx.doi.org/10.1016/j.compscitech.2015.01.010.

[36] Neil E. Todreas and Mujid S. Kazimi. *Nuclear Systems I - Thermal Hydraulics Fundamentals*. Taylor & Francis, Levittown, PA, USA, 1993.

[37] Peter D. Johnson and Jack A. Rubin. UO_2–BeO fuel process. On the WWW, February 16 1975. URL: http://www.google.ch/patents/US3865746.

[38] Shinji ISHIMOTO, Mutsumi HIRAI, Kenichi ITO, and Yoshiaki KOREI. Thermal conductivity of UO_2-BeO pellet. *Journal of Nuclear Science and Technology*, 33(2):133–140, February 1996.

[39] J. Fourcade, K.H. Sarma, S.G. Lee, and A.A. Solomon. Enhanced thermal conductivity oxide or ECO fuels. *Transactions of the American Nuclear Society*, 92:179–180, 2005.

[40] A.A. Solomon, Shripad Revankar, and J.K. McCoy. Enhanced Thermal Conductivity Oxide Fuels. Final Report 02-180, Purdue University, W. Lafayette, IN, September 14 2005. -.

[41] S.M. McDeavitt, J.C. Ragusa, J. Smith, C. Garcia, and J. Malone. Behavior assessments for UO_2-BeO enhanced conductivity fuels. https://ucarecdn.com/8993f12a-33a8-4cf2-9f58-db75ddfd1cbc/-/inline/yes/, December 2015.

[42] S.K. Kim, W.I. Ko, H.D. Kim, Shripad T. Revankar, W. Zhou, and Daeseong Jo. Cost - benefit analysis of BeO - UO_2 nuclear fuel. *Progress in NuclearEnergy*, 52(8):813–821, November 2010.

[43] Deepthi Chandramouli and Shripad T. Revankar. Development of thermal models and analysis of UO_2-BeO fuel during a loss of coolant accident. *International Journal of Nuclear Energy*, 2014(Article ID 751070):9, 2014.

[44] M.A. McGrath, B.Yu. Volkov, and Y. Russin. In-reactor investigation of the composite UO_2-BeO fuel: background, results and perspectives. A poster presented at The Nuclear Materials Conference, Montpellier (France), November 2016.

[45] R. W. Powell, C. Y. Ho, and P. E. Liley. Thermal conductivity of selected materials. Final report nsrds-nbs8, National Bureau of Standards (Purdue University), Yeager Road, IN, November 1966. See also URL `https://archive.org/details/thermalconductiv08powe`.

[46] S. Yeo, E. Mckenna, R. Baney, G. Subhash, and J. Tulenko. Enhanced thermal conductivity of uranium dioxide – silicon carbide composite fuel pellets prepared by spark plasma sintering (SPS). *Journal of Nuclear Materials*, 433(1–3):66–73, April 2013.

[47] Zhichao Chen, Ghatu Subhash, and James S. Tulenko. Master sintering curves for UO_2 and UO_2-SiC composite processed by spark plasma sintering. *Journal of Nuclear Materials*, 454(1-3):427–433, November 2014.

[48] J. S. Tulenko and R. H. Baney. An Innovative High Thermal Conductivity Fuel Design. Final report DE-FG07-04ID14598, The University of Florida,

Gainesville, FL, October 2007. URL: https://www.osti.gov/scitech/servlets/purl/917989.

[49] Chinthaka M. Silva, Yutai Katoh, Stewart L. Voit, and Lance L. Snead. Chemical reactivity of CVC and CVD SiC with UO_2 at high temperatures. *Journal of Nuclear Materials*, 460:52 – 59, 2015. URL: http://www.sciencedirect.com/science/article/pii/S0022311515000872, doi:https://doi.org/10.1016/j.jnucmat.2015.02.002.

[50] Rohm and Haas. CVD silicon carbide. On the WWW, September 2000. PDF file. URL: http://www.dow.com/assets/attachments/business/gt/advanced_ceramics/cvd_silicon_carbide/tds/cvd_silicon_carbide.pdf.

[51] Lance L. Snead, Takashi Nozawa, Yutai Katoh, Thak-Sang Byun, Sosuke Kondo, and David A. Petti. Handbook of SiC properties for fuel performance modeling. *Journal of Nuclear Materials*, 371(1–3):329–377, September 2007.

[52] Andrew Cartas, Haitang Wang, Ghatu Subhash, Ronald Baney, and James Tulenko. Influence of carbon nanotube dispersion in UO_2–carbon nanotube ceramic matrix composites utilizing spark plasma sintering. *Nuclear Technology*, 189(3):258–267, 2015. URL: http://dx.doi.org/10.13182/NT14-7, arXiv:http://dx.doi.org/10.13182/NT14-7, doi:10.13182/NT14-7.

[53] Eric Pop, David Mann, Qian Wang, and Kenneth Goodson andHongjie Dai. Thermal conductance of an individual single-wall carbon nanotube above room temperature. *Nano Letters*, 6(1):96–100, December 22 2005.

[54] Y. W. Kwon. Heat conduction analysis of randomly dispersed single walled carbon nanotubes. MS Thesis, Naval Postgraduate School, Monterey, California, June 2007. URL: https://calhoun.nps.edu/bitstream/handle/10945/3367/07Jun_Felder.pdf?sequence=1&isAllowed=y.

[55] Jianwei Che, Tahir, Cagin, and William A. Goddard. Thermal conductivity of carbon nanotubes. *Nanotechnology*, 11(–):65–69, March 2000.

[56] YAN He and YUANZHENG TANG. Thermal conductivity of carbon nanotube/natural rubber composite from molecular dynamics simulations. *Journal of Theoretical and Computational Chemistry*, 12(03):1350011, 2013.

[57] D. F. Hollenbach, L. J. Ott, T. M. Besmann, B. L. Armstrong, A. A. Wereszczak, H. T. Lin, R. J. Ellis, P. F. Becher, R. T. Jubin, and S. L.

Voit. Technical project plan for the enhanced thermal conductivity of oxide fuels through the addition of high thermal conductivity fibers and microstructural engineering. Technical Project Plan ORNL/TM-2010/233, Oak Ridge National Laboratory, Oak Ridge, TN, September 2010. See also URL http://info.ornl.gov/sites/publications/files/Pub26612.pdf.

[58] G. E. Youngblood, D. J. Senor, J. W. Kowbel, J. Webb, and Akira Kohyama. Thermal conductivity of SiC and C fibers. Fusion Materials Semiannual Progress Report (FMSPR) for period ending December 31 DOE/ER-031327, Pacific Northwest National Laboratory, Richland, WA, December 1999.

[59] L.L. Snead, M. Balden, R.A. Causey, and H. Atsumi. High thermal conductivity of graphite fiber silicon carbide composites for fusion reactor application. *Journal of Nuclear Materials*, 307-311, Part 2:1200–1204, 2002. URL: http://www.sciencedirect.com/science/article/pii/S0022311502011157, doi:http://dx.doi.org/10.1016/S0022-3115(02)01115-7.

[60] L.L. Snead, M. Balden, Rion Causey, and H. Atsumi. SiC/graphite System for High-Heat-Flux Applications. On the WWW, - -. URL slideplayer.com/slide/6052915/.

[61] Chunghao Shih, Yutai Katoh, Lance L. Snead, and John Steinbeck. The effect of neutron irradiation on the mechanical properties of C/SiC composites. *Journal of Nuclear Materials*, 439(1):192 – 201, 2013. URL: http://www.sciencedirect.com/science/article/pii/S0022311513005928, doi:https://doi.org/10.1016/j.jnucmat.2013.03.089.

[62] Zhichao Chen, Ghatu Subhash, and James S. Tulenko. Spark plasma sintering of diamond-reinforced uranium dioxide composite fuel pellets. *Nuclear Engineering and Design*, 294(Supplement C):52 – 59, 2015. URL: http://www.sciencedirect.com/science/article/pii/S0029549315003957, doi:https://doi.org/10.1016/j.nucengdes.2015.08.021.

[63] James Tulenko and Ghatu Subhash. Development of Innovative Accident Tolerant High Thermal Conductivity UO_2-Diamond Composite Fuel Pellets. Final report Project No. 12-4037, University of Florida, Gainesville, FL, January 2016. See also URL https://www.osti.gov/scitech/servlets/purl/1239275.

[64] Zhichao Chen, Ghatu Subhash, and James S. Tulenko. Raman spectroscopic investigation of graphitization of diamond during spark plasma

sintering of UO_2 diamond composite nuclear fuel. *Journal of Nuclear Materials*, 475(Supplement C):1 – 5, 2016. URL: http://www.sciencedirect.com/science/article/pii/S0022311516300897, doi:https://doi.org/10.1016/j.jnucmat.2016.03.015.

[65] R.A. Khmelnitsky and A.A. Gippius. Transformation of diamond to graphite under heat treatment at low pressure. *Phase Transitions*, 87(2):175–192, 2014. URL: http://dx.doi.org/10.1080/01411594.2013.807429, arXiv:http://dx.doi.org/10.1080/01411594.2013.807429.

[66] Diamond materials. The CVD diamond booklet. On the WWW, at http://www.diamond-materials.com/downloads/cvd_diamond_booklet.pdf, - c2008. PDF file.

[67] J.R. Olson, R.O. Pohl, J.W. Vandersande, A. Zoltan, T.R. Anthony, and W.F. Banholzer. Thermal conductivity of diamond between 170 and 1200 k and the isotope effect. *Phys. Rev. B*, 47:14850–14856, Jun 1993. URL: https://link.aps.org/doi/10.1103/PhysRevB.47.14850, doi:10.1103/PhysRevB.47.14850.

[68] Magnus Willander, Milan Friesel, Qamar-ul Wahab, and Boris Straumal. Silicon carbide and diamond for high temperature device applications. *Journal of Materials Science: Materials in Electronics*, 17(1):1, Jan 2006. URL: https://doi.org/10.1007/s10854-005-5137-4, doi:10.1007/s10854-005-5137-4.

[69] DaDong Shao, JiaXing Li, XiangKe Wang, JiaXing Li, and XiangKe Wang. Poly(amidoxime)-reduced graphene oxide composites as adsorbents for the enrichment of uranium from seawater. *Science China Chemistry*, 57(11):1449–1458, Nov 2014. URL: https://doi.org/10.1007/s11426-014-5195-7, doi:10.1007/s11426-014-5195-7.

[70] S. W. Lee, H. T. Kim, and I. C. Bang. Performance evaluation of UO_2/graphene composite fuel and SiC cladding during LBLOCA using MARS-KS. *Nuclear Engineering and Design*, 257:139–145, April 2013.

[71] Y. Katoh, L.L. Snead, and C.H. Henager. Overview of US SiC/SiC RD activity for fusion applications. On the WWW, – 2006. URL: ftp://ftp.nrg.eu/pub/www/nrg/2006_csicc/pres/1A_US_SiC_overview-Katoh.pdf.

[72] L.L. Snead, S.J. Zinkle, and D.P. White. Thermal conductivity degradation of ceramic materials due to low temperature, low dose neutron irradiation. *Journal of Nuclear Materials*, 340(2-3):187–202, April 2005.

[73] Ctirad Uher and Donald T. Morelli. Influence of neutron irradiation on the thermal conductivity of vapor-deposited diamond. *Journal of Applied Physics*, 76(3):1515–1517, 1994. doi:10.1063/1.357727.

[74] D. T. Morelli and T. A. Perry. *Phonon Scattering in Lightly-Neutron-Irradiated Diamond*, pages 37–38. Springer Berlin Heidelberg, Berlin, Heidelberg, 1993. URL: https://doi.org/10.1007/978-3-642-84888-9_13, doi:10.1007/978-3-642-84888-9_13.

[75] L.L. Snead and T.D. Burchell. Thermal conductivity degradation of graphites due to nuetron irradiation at low temperature. *Journal of Nuclear Materials*, 224(3):222 – 229, 1995. URL: http://www.sciencedirect.com/science/article/pii/0022311595000712, doi:https://doi.org/10.1016/0022-3115(95)00071-2.

[76] L.L. Snead. Accumulation of thermal resistance in neutron irradiated graphite materials. *Journal of Nuclear Materials*, 381(1):76 – 82, 2008. Proceedings of the Seventh and Eighth International Graphite Specialists Meetings (INGSM). URL: http://www.sciencedirect.com/science/article/pii/S0022311508004030, doi:https://doi.org/10.1016/j.jnucmat.2008.07.017.

[77] L.L. Snead and T.D. Burchell. Reduction in thermal conductivity due to neutron irradiation. On the WWW, July 1995. URL http://www.acs.omnibooksonline.com/data/papers/1995_774.pdf.

[78] B.T. Pham and J.J. Einerson G.L. Hawkes. Uncertainty Quantification of Calculated Temperatures for the U.S. Capsules in the AGR-2 Experiment. Final report INL/EXT-15-34587, Idaho National Laboratory, Idaho Falls, ID, March 2015. URL: http://https://www.osti.gov/scitech/servlets/purl/1184085+.

[79] Yutai Katoh, Takashi Nozawa, Lance L. Snead, Kazumi Ozawa, and Hiroyasu Tanigawa. Stability of SiC and its composites at high neutron fluence. *Journal of Nuclear Materials*, 417(1–3):400–405, October 2011.

[80] M. Rohde. Reduction of the thermal conductivity of SiC by radiation damage. *Journal of Nuclear Materials*, 182:87–92, May-June 1991.

[81] J.B.J. Hegeman, J.G. van der Laan, M. van Kranenburg, M. Jong, D. d'Hulst, and P. ten Pierick. Mechanical and thermal properties of SiC_f/SiC composites irradiated with neutrons at high temperatures. *Fusion Engineering and Design*, 75–79:789–793, November 2005.

[82] G.E. Youngblood, D.J. Senor, and R.H. Jones. Thermal diffusivity/conductivity of irradiated monolithic CVD-SiC. *Fusionl Materials: Semi-Annual Progress Report Ending December 31*, 33:27–33, 2002.

[83] D.J. Senor, G.E. Youngblood, L.R. Greenwood, D.V. Archer, D.L. Alexander, M.C. Chen, and G.A. Newsomeb. Defect structure and evolution in silicon carbide irradiated to 1 dpa-SiC at 1100 °C. *Journal of Nuclear Materials*, 317(2-3):145–159, May 2003.

[84] D.J. Senor, G.E. Youngblood, C.E. Moore, D.J. Trimble, G.A. Newsome, and J.J. Woods. Effects of neutron irradiation on thermal conductivity of SiC-based composites and monolithic ceramics. *Fusion Technology*, 30(3):943–955, 1996.

[85] L.L. Snead. Limits on irradiation-induced thermal conductivity and electrical resistivity in silicon carbide materials. *Journal of Nuclear Materials*, -329–333, Part A(1):524–529, August 2004.

[86] R.J. Price. Thermal conductivity of neutron-irradiated pyrolytic $\beta-$silicon carbide. *Journal of Nuclear Materials*, 46(3):268–272, April 1973.

[87] R.J. Price. Effects of fast-neutron irradiation on pyrolytic silicon carbide. *Journal of Nuclear Materials*, 33(1):17 – 22, 1969. URL: `http://www.sciencedirect.com/science/article/pii/0022311569900038`, `doi:https://doi.org/10.1016/0022-3115(69)90003-8`.

[88] H.L. Heinisch, L.R. Greenwood, W.J. Weber, and R.E. Williford. Displacement damage in silicon carbide irradiated in fission reactors. *Journal of Nuclear Materials*, 327(2-3):175–181, 2004. URL: `http://www.sciencedirect.com/science/article/pii/S0022311504000820`, `doi:http://dx.doi.org/10.1016/j.jnucmat.2004.02.012`.

[89] OECD/NEA Data Bank. *Janis 4.0 User's guide*. OECD/NEA Data Bank, Le Seine Saint-Germain, France, 1 edition, 2013. URL: `https://www.oecd-nea.org/janis/janis-4.0/documentation/janis-4.0_manual_rev1.pdf`.

[90] S.G. Popov, J.J. Carbajo, V.K. Ivanov, and G.L. Yoder. Thermophysical properties of MOX and UO_2 Fuels Including the Effects of Irradiation. Scientific report ORNL/TM-2000/351, Oak Ridge National Laboratory, Oak Ridge, TN, November 2000. See also URL `http://web.ornl.gov/~webworks/cpr/v823/rpt/109264.pdf`.

[91] IAEA. Thermophysical properties of materials for nuclear engineering: a tutorial and collection of data. On the WWW, at www-pub.iaea.org/MTCD/publications/PDF/IAEA-THPH_web.pdf, November 2008. PDF file, ISBN 9789201065087.

[92] A. Taylor and R. M. Jones. *Silicon Carbide — A High Temperature Semiconductor*. Pergamon Press, xford, London, New York, Paris, 1960.

[93] web1. SiC - Silicon Carbide. On the WWW, January 2018. URL http://www.ioffe.ru/SVA/NSM/Semicond/SiC/basic.html.

[94] Garry L.Harris. *Properties of Silicon Carbide*. INSPEC, London, UK, 1995.

[95] Libo Deng, Robert J. Young, Ian A. Kinloch, Rong Sun, Guoping Zhang, Laure Noe, and Marc Monthioux. Coefficient of thermal expansion of carbon nanotubes measured by raman spectroscopy. *Applied Physics Letters*, 104(5):051907, 2014. URL: https://doi.org/10.1063/1.4864056, doi:10.1063/1.4864056.

[96] Ch. Laurent, E. Flahaut, and A. Peigney. The weight and density of carbon nanotubes versus the number of walls and diameter. *Carbon*, 48(10):2994 – 2996, 2010. URL: http://www.sciencedirect.com/science/article/pii/S0008622310002617, doi:https://doi.org/10.1016/j.carbon.2010.04.010.

[97] Robert R. Reeber and Kai Wang. Thermal expansion, molar volume and specific heat of diamond from 0 to 3000k. *Journal of Electronic Materials*, 25(1):63–67, Jan 1996. URL: https://doi.org/10.1007/BF02666175, doi:10.1007/BF02666175.

[98] National Institute of Standard and Technology. Sintered Silicon Carbide (SiC). On the WWW, February 2001. URL https://srdata.nist.gov/CeramicDataPortal/Pds/Scdscs.

[99] Xu Guo, Jingbo Liao, and Xiangyang Wang. Investigation of the thermo-mechanical properties of single-walled carbon nanotubes based on the temperature-related higher order cauchy–born rule. *Computational Materials Science*, 51(1):445 – 454, 2012. URL: http://www.sciencedirect.com/science/article/pii/S0927025611004502, doi:https://doi.org/10.1016/j.commatsci.2011.07.058.

[100] Howard W. Day. A revised diamond-graphite transition curve. *American Mineralogist*, 97:52–62, 2012.

[101] L. J. Siefken, E. W. Coryell, E. A. Harvego, and J. K. Hohorst. *SCDAP/RELAP53/MOD3.3D Code Manual-NUREG/CR-6150*. IdahoNnationalEngineering and Enviromental Laboratory, Idaho Falls, Idaho 83415, vol.4,rev.2 edition, 2001. See also URL pbadupws.nrc.gov/docs/ML0103/ML010330363.pdf.

[102] Rong Liu, Wenzhong Zhou, Andrew Prudil, and Paul K. Chan. Multiphysics modeling of UO_2-SiC composite fuel performance with enhanced thermal and mechanical properties. *Applied Thermal Engineering*, 107(Supplement C):86 – 100, 2016. URL: http://www.sciencedirect.com/science/article/pii/S1359431116310870, doi:https://doi.org/10.1016/j.applthermaleng.2016.06.173.

[103] J. D. Hales, S. R. Novascone, G. Pastore, D. M. Perez, B. W. Spencer, and R. L. Williamson. *BISON Theory Manual*. Fuels Modeling and Simulation Department, Idaho National Laboratory, Idaho Falls, ID, - edition, 2013. See also URL neup.inl.gov/SiteAssets/FY2014Documents/BISON_theory_manual.pdf.

[104] D.G Martin. The thermal expansion of solid UO_2 and (U, Pu) mixed oxides — a review and recommendations. *Journal of Nuclear Materials*, 152(2):94 – 101, 1988. URL: http://www.sciencedirect.com/science/article/pii/0022311588903157, doi:https://doi.org/10.1016/0022-3115(88)90315-7.

[105] U.S. Department of Energy. DOE fundamentals handbook -Nuclear physics and reactor theory - vol. 2. On the WWW, January 1993. URL: http://large.stanford.edu/courses/2014/ph241/alnoaimi2/docs/Nuclear-Volume2.pdf.

[106] J. R. Smith. Enhanced thermal conductivity UO_2–BeO nuclear fuel: neutronic performance studies and economic analyses. MS Thesis, Texas A&M University, College Station, Texas, December 2012.

[107] Jiwei Wang. *Developing a high thermal conductivity nuclear fuel with silicon carbide additives*. PhD Thesis, University of Florida, Gainesville, FL, August 2008.

[108] INEEL. *SCDAP/RELAP5-3D CODE MANUAL: volume 4: MATPRO - a library of materials properties for light-water-reactor accident analysis*. IdahoNnationalEngineering and Enviromental Laboratory, Idaho Falls, Idaho 83415, 2003. See also URL www4vip.inl.gov/relap5/scdap/vol4.pdf.

[109] F. Pazdera and J. Belac. Safety Criteria and Their Comparison between WWER and PWR. Report INIS-BG–0858, Nuclear Research Institute Rez plc, Rez, Czech Republic, September 2003. URL: http://www.iaea.org/inis/collection/NCLCollectionStore/_Public/36/040/36040516.pdf.

[110] Hector Hernandez-Lopez and Marco A. Lucatero. Linear heat generation rate for breaking plastic strain limit of cladding in a bwr fuel rod type. *Annals of Nuclear Energy*, 90(Supplement C):234 – 239, 2016. URL: http://www.sciencedirect.com/science/article/pii/S0306454915300062, doi:https://doi.org/10.1016/j.anucene.2015.12.005.

[111] Motoe SUZUKI and Hiroaki SAITOU. *Light Water Reactor Fuel Analysis Code FEMAXI-6 (Ver.1)*. Japan Atomic Energy Agency, Tokai-mura, Japan, jaea-data/code 2005-003 edition, 2005. -.

[112] Information Systems Laboratories. *RELAP5/MOD3.3 code manual volume I: code structure, system models, and solution methods*. Information Systems Laboratories, Idaho Falls, Idaho, latest edition, 2010.

[113] M. Lovecky, L. Piterka, J. Prehradny, and R. Skoda. UWB1 – fast nuclear fuel depletion code. *Annals of Nuclear Energy*, 71:333–339, May 2014.

[114] M. Lovecky and J. Jirickova andR. Skoda. Monte carlo solver for UWB1 nuclear fuel depletion code. *Annals of Nuclear Energy*, 85:778–787, July 2015.

[115] P. Van Uffelen, C. Gyori, A. Schubert, J. van de Laar, Z. Hozer, and G. Spykman. Extending the application range of a fuel performance code from normal operating to design basis accident conditions. *Journal of Nuclear Materials*, 383:137–143, 2008.

[116] Foral. Personal communication with Gerold Spykman. –, January 2012.

[117] G. Passage, I. Mandev, M. Georgieva, S. Stefanova, K. Kamenov, and A. Ivanova. Computational analysis of the WWER-1000 fuel rod thermomechanical behaviour under loca conditions. 9 International conference on WWER fuel performance, modelling and experimental support, 17-24 Sep 2011. URL: www.iaea.org/inis/collection/NCLCollectionStore/_Public/43/056/43056323.pdf.

[118] P. Van Uffelen et al. Verification of the transuranus fuel performance code - an overview. In *7 International conference on WWER fuel performance, modelling and experimental support*, volume **1**, 2008.

[119] SUJB. Vyber a hodnoceni projektovych a nadprojektovych udalosti pro JE - bezpecenostni navod JB-1.7. On the WWW, December 2003. URL: https://www.sujb.cz/fileadmin/sujb/docs/dokumenty/publikace/G2-EF-final_udalosti_a_rizika_PUBLIKACE.pdf.

[120] IAEA. Deterministic Safety Analysis for Nuclear Power Plants (SSG). On the WWW, December 2003. URL: https://www-pub.iaea.org/MTCD/publications/PDF/Pub1428_web.pdf.

[121] M. Suzuki, K. Kusagaya, H. Saitou, and T. Fuketa. Analysis on lift-off experiment in halden reactor by femaxi-6 code. *Journal of Nuclear Materials*, 335(3):417 – 424, 2004. URL: http://www.sciencedirect.com/science/article/pii/S0022311504006610, doi:https://doi.org/10.1016/j.jnucmat.2004.07.049.

[122] Suzuki Motoe. Analysis of high burnup fuel behavior in halden reactor by femaxi–v code. *Nuclear Engineering and Design*, 201(1):99–106, 2000. URL: http://www.sciencedirect.com/science/article/pii/S0029549300002478, doi:https://doi.org/10.1016/S0029-5493(00)00247-8.

[123] Jaemin Sohn, Dongsoo Lee, Sungjae Park, Yoontaeg Shin, Keenam Choo, Mansoon Cho, Myounghwan Choi, Bonggoo Kim, and Harkrho Kim. Analysis of the internal pressure of the nuclear fuel rod irradiated by an instrumented fuel capsule at HANARO. On the WWW, November 2006. URL www.kns.org/kns_files/kns/file/157%BC%D5%C0%E7%B9%CE.pdf.

[124] Jaemin Sohn, Sungjae Park, Yoontaeg Shin, Keenam Choo, Mansoon Cho, Bonggoo Kim, and Harkrho Kim. Analysis of the elongation of nuclear fuels irradiated by an instrumented fuel capsule at at HANARO. On the WWW, May 2007. URL: https://www.kns.org/kns_files/kns/file/157%BC%D5%C0%E7%B9%CE.pdf.

[125] Akifumi Yamaji, Motoe Suzuki, and Tsutomu Okubo. FEMAXI-6 code verification with MOX fuels irradiated in Halden reactor. *Journal of Nuclear Science and Technology*, 46(12):1152–1161, 12 2009. doi:10.3327/jnst.46.1152.

[126] S.N. Pelykh, M.V. Maksimov, and G.T. Parks. A method for vver-1000 fuel rearrangement optimization taking into account both fuel cladding durability and burnup. *Nuclear Engineering and Design*, 257(Supplement C):53 – 60, 2013. URL: http://www.sciencedirect.com/science/article/pii/

S0029549313000368, doi:https://doi.org/10.1016/j.nucengdes.2012.12.022.

[127] M. V. Maksimov, S. N. Pelykh, and R. L. Gontar. Principles of controlling fuel-element cladding lifetime in variable vver-1000 loading regimes. *Atomic Energy*, 112(4):241–249, Aug 2012. URL: https://doi.org/10.1007/s10512-012-9552-3, doi:10.1007/s10512-012-9552-3.

[128] M. V. Maksimov, S. N. Pelykh, O. V. Maslov, and V. E. Baskakov. Method for evaluating the service life of vver-1000 fuel-element cladding in different loading regimes. *Atomic Energy*, 108(5):357–363, Sep 2010. URL: https://doi.org/10.1007/s10512-010-9301-4, doi:10.1007/s10512-010-9301-4.

[129] A. Yamaji, Y. Oka, Y. Ishiwatari, J. Liu, and M. Suzuki. Principle of rationalizing the criteria for abnormal transients of the super lwr with fuel rod analyses. *Annals of Nuclear Energy*, 33(11):984 – 993, 2006. URL: http://www.sciencedirect.com/science/article/pii/S0306454906001034, doi:https://doi.org/10.1016/j.anucene.2006.05.010.

[130] US NRC. Technical Report on Densification of Light Water Reactor Fuels,. AEC Regulatory Staff Report WASH-1236, -, -, November 14 1972. See also [111].

[131] Jason Hales Xu Wu, Piyush Sabharwall. *Neutronics and Fuel Performance Evaluation of Accident Tolerant Fuel under Normal Operation Conditions*. The INL is a U.S. Department of Energy National Laboratory, July 2014. URL: http://www.osti.gov/scitech/servlets/purl/1166052, doi:10.2172/1166052.

[132] SUNGHWAN YEO. *UO_2–SiC composite reactor fuels with enhanced thermal and mechanical properties prepared by spark plasma sintering*. PhD Thesis, University of Florida, Gainesville, Florida, August 2013. -.

[133] A. R. Massih. Effect of additives on uranium dioxide fuel behavior. - 2014:21, Stralsakerhetsmyndigheten, Stockholm, Sweden, January 2014. URL: http://www.stralsakerhetsmyndigheten.se.

[134] C. Gyori, Z. Hozer, E. Perez-Fero, P. van Uffelen, A. Schubert, and J. van de Laar. Applying the TRANSURANUS code to VVER fuel under accident conditions. 18th International Conference on Structural Mechanics in Reactor Technology (SMiRT 18), August 7-12 2005. SMiRT18-C04-3.

[135] P.D. Bayless. RELAP/MOD3.2 Assessment Using an 11% Upper Plenum Break Experiment in the PSB Facility. IReport INEEL/EXT-03-00058, Idaho National Engineering and Environmental Laboratory, Bechtel BWXT Idaho, Idaho, January 2003. URL: hwww.osti.gov/scitech/servlets/purl/808522.

[136] TVEL JSC. Nuclear fuel for VVER reactors. On the WWW, - 2011. PDF file. URL: http://www.iaea.org/inis/collection/NCLCollectionStore/_Public/37/098/37098302.pdf.

[137] Nikolaus Mullner. *Simulation of Beyond Design Basis Accidents - a Contribution to Risk Analysis of Nuclear Power Plants*. PhD Thesis, Universitat Wien, Vienna, Austria, November 2010. -.

[138] Jonas Frantz. g3data. On the WWW, May 2011. URL: http://github.com/pn2200/g3data/.

[139] Ankit Rohatgi. WebPlotDigitizer (Version 3.12). On the WWW, June 2017. URL: https://automeris.io/WebPlotDigitizer/.

[140] P. S. Damerell and J. W. Simons. 2D/3D Program Work Summary Report. International Agreement Report 1, Office of Nuclear Regulatory Research, US NRC, Washington, CD 20555, june 1993. NUREG/IA-0126.

[141] R. F. Kunz, G. F. Kasmala, J. H. Mahaffy, and C. J. Murray. An automated code assessment program for determining systems code accuracy. OECD/CSNI Workshop on Advanced Thermal-Hydraulic and Neutronic Codes: Current and Future Applications, Barcelona, Spain, 10-13 April 2000.

[142] Robert F Kunz, Gerald F Kasmala, John H Mahaffy, and Christopher J Murray. On the automated assessment of nuclear reactor systems code accuracy. *Nuclear Engineering and Design*, 211(2):245 – 272, 2002. URL: http://www.sciencedirect.com/science/article/pii/S002954930100440X, doi:https://doi.org/10.1016/S0029-5493(01)00440-X.

[143] P. Kral. *Thesis to Dissertation thesis Influence of presence of non-condensable gases on the behaviour of VVER primary circuit*. PhD Thesis, Czech technical university, Prague, MA, - 2014. In czech.

[144] M.D. Lazor. Evaluation of assessment techniques for verification and validation of the trace nuclear systems code. MS Thesis, The Pennsylvania State University, State College, PA, December 2004.

[145] D. Pack and E. May. *RELAP5/MOD3.3 CODE MANUAL VOLUME V: User Guideline*. Information Systems Laboratories, Inc.,Rockville, Maryland, Idaho Falls, Idaho, latest edition, 2010. NUREG/CR-5535/Rev P4-Vol. V .

[146] D. Krylov. New types of nuclear fuel. On the WWW, June 2011. URL: http://2011.atomexpo.ru/mediafiles/u/files/Present2011/Krylov_D.V._eng.pdf.

[147] Ondrej Novak. Study of VVER - 1000 Fuel Cycle Using NESTLE and ORIGEN Codes. MS Thesis, Czech Technical University in Prague, Prague, Czech Republic, May 2016. URL: https://www.academia.edu/32855663/Study_of_VVER_-1000_Fuel_Cycle_Using_NESTLE_and_ORIGEN_Codes.

[148] V. Molchanov. Nuclear fuel for VVER reactors - actual state and trends. On the WWW, September 2009. URL: http://www.iaea.org/inis/collection/NCLCollectionStore/_Public/43/056/43056258.pdf.

[149] M.C. Billone, H.M. Chung, and Y. Yan. Steam Oxidation Kinetics of Zirconium Alloys,. Report 1, Argonne National Laboratory, Argonne, Illinois, June 4 2002. See also URL http://https://www.nrc.gov/docs/ML0216/ML021680052.pdf.

[150] E. Elias, D. Hasan, and Y. Nekhamkin. Zirconium ignition in exposed fuel channel. *Nuclear Engineering and Design*, 286:205 – 210, 2015. URL: http://www.sciencedirect.com/science/article/pii/S0029549315001041, doi:https://doi.org/10.1016/j.nucengdes.2015.03.002.

[151] V.I. Almjashev et al. Ternary eutectics in the systems FeO–UO_2–ZrO2 and Fe2O3–U3O8–ZrO2. *Radiochemistry*, 53(1):13–18, February 2011.

[152] W.B.Wilson et al. *American National Standard for Decay Heat Power in Light Water Reactors*. American Nuclear Society, La Grange Park, Illinois 60525 USA, ANSI/ANS-5.1-1994 edition, 1994. -.

[153] NEA/OECD. Nuclear Fuel Behaviour under Reactivity-initiated Accident (RIA) Conditions. State of the art report 1, Nuclear Energy Agency, Paris, France, 2010.

[154] Motoe Suzuki, Hiroaki Saitou, and Toyosi Fuketa. Analysis on split failure of cladding of high burnup BWR rods in reactivity-initiated accident conditions by RANNS code. *Nuclear Engineering and Design*, 263:128–139, July 2005.

[155] Zoltan Hozer. Review of RIA and LOCA criteria for VVER fuel. In *6th International conference on WWER fuel performance, modelling and experimental support*, Publisher address, September 2006. URL: http://www.iaea.org/inis/collection/NCLCollectionStore/_Public/37/098/37098346.pdf?r=1.

[156] NEA/OECD. Fuel safety criteria in NEA member countries. Compilation of responses received from member countries 1, Nuclear Energy Agency, Paris, France, March 2003.

[157] K. L. Murty. *Materials Ageing and Degradation in Light Water Reactors: Mechanisms and Management*. Woodhead Publishing, Philadelphia, USA, 2013.

[158] Lap Y. Cheng, A. Cuadra, M. Todosow, K. A. Gamble, and P. G. Medvedev. Performance of U3Si2 fuel in a reactivity insertion accident (preprint). On the WWW, April 2016. URL: https://www.osti.gov/servlets/purl/1367835.